

DYNAMICS AND RHEOLOGY OF A DILUTE SUSPENSION OF ELASTIC CAPSULES

BY

RAM CHANDRA MURTHY KALLURI

A thesis submitted to the

Graduate School—New Brunswick

Rutgers, The State University of New Jersey

in partial fulfillment of the requirements

for the degree of

Master of Science

Graduate Program in Mechanical and Aerospace Engineering

Written under the direction of

Prof. Prosenjit Bagchi

and approved by

New Brunswick, New Jersey

OCTOBER, 2010

ABSTRACT OF THE THESIS

Dynamics and Rheology of a Dilute Suspension of Elastic Capsules

by

Ram Chandra Murthy Kalluri

Thesis Director: Prof. Prosenjit Bagchi

Three-dimensional numerical simulations using front-tracking method are considered to study the dynamics and rheology of a suspension of elastic capsules in linear shear flow over a broad range of viscosity contrast (ratio of internal-to-external fluid viscosity), shear rate (or, capillary number), and aspect ratio. First, we focus on the coupling between the shape deformation and orientation dynamics of capsules, and show how this coupling influences the transition from the tank-treading to tumbling motion. At low capillary numbers, three distinct modes of motion are identified: a swinging or oscillatory (OS) mode at a low viscosity contrast in which the inclination angle $\theta(t)$ oscillates but always remains

positive; a vacillating-breathing (VB) mode at a moderate viscosity contrast in which $\theta(t)$ periodically becomes positive and negative, but a full tumbling does not occur; and a pure tumbling mode (TU) at a higher viscosity contrast. At higher capillary numbers, three types of transient motions occur, in addition to the OS and TU modes, during which the capsule switches from one mode to the other as (i) VB to OS, (ii) TU to VB to OS, and (iii) TU to VB. It is shown that the coupling between the shape deformation and orientation is the strongest in the VB mode. The numerical results are compared with the theories of Keller and Skalak, and Skotheim and Secomb. Significant departures from the two theories are discussed and related to the strong coupling between the shape deformation, inclination, and transition dynamics.

We then address the rheology of a dilute suspension of liquid-filled elastic capsules. We consider capsules of spherical resting shape for which only a steady tank-treading motion is observed. It is shown that the suspension exhibits a shear viscosity minimum at moderate values of the viscosity ratio, and high capillary numbers. The normal stress differences are shown to decrease with increasing capillary number at high viscosity ratios. Such non-trivial results can neither be predicted by the small-deformation theory, nor can be explained by the capsule geometry alone. Physical mechanisms underlying these novel results are studied by decomposing the particle stress tensor into a contribution due to the elastic stresses in the capsule membrane, and a contribution due to the viscosity differences between the internal and suspending fluids. It is shown that the elastic

contribution is shear-thinning, but the viscous contribution is shear-thickening. The coupling between the capsule geometry, and the elastic and viscous contributions is analysed to explain the observed trends in the bulk rheology.

Acknowledgements

Firstly, I would like to thank my advisor Prof. Prosenjit Bagchi for his invaluable guidance and support throughout my period of study here. His unique way of working with the students has greatly helped me in overcoming my research obstacles. His methodical and scientific way of analyzing problems to extract the underlying physics has always been a strong source of inspiration for me. In addition to this, the courses that I took under him gave me strong grip on the fundamentals of fluid mechanics which I found useful even in my research.

Secondly, I would like to give my sincere appreciation to all of my family who have always been there for me with encouragement and without their support, none of this would have been possible.

I would like to thank my friends and co-workers Sai, Vijay, Kirit and Alireza for valuable discussions regarding various topics of interest related to and outside my field of research. I would like to take this opportunity to acknowledge the support of my friend and former classmate Phani Kumar whose encouragement lies behind my significant accomplishments. I will also remember all my labmates for maintaining a good work atmosphere with pleasant as well as useful discussions. I would like to give a special mention to Prof. Doyle Dana Knight for bringing a very friendly and cheerful attitude at the workplace. I will never forget the good

times with all the pleasant anecdotes he shared with us.

I thank my roommates Pavan, Naga, Vijay, Navi, Daman, Deep, Srinivas, Sandeep, Hasan, Siddhant and Sankha for sharing their day to day experiences and making my stay at home memorable. They have also been supportive to me to get past my states of melancholy.

I extend my thanks to my friends Dhaval, Hadi, Kelly, Tushar, John, Aditya, Pallab, Venkat, Iyer, Sohrob and Elan for sharing the good times during the department BBQs and other events. I have also greatly enjoyed short lunch and coffee breaks with Marco, Ramon, Sankha, Alireza and my special friend Giorgiana and thank them for making my stay at Rutgers cherishable.

Last but not the least, I would like to thank many others whom I have not mentioned here for making my stay at Rutgers mutually productive and enjoyable both professionally and personally.

This research is funded by NSF grant No. BES-0603035 and No. CTS-0625936. Computational supports from the NSF-funded Teragrid resources at SDSC, TACC, NCSA and NERSC resources at DOE LBNL are acknowledged.

Dedication

To my family

Table of Contents

Abstract	ii
Acknowledgements	v
Dedication	vii
List of Tables	xi
List of Figures	xii
1. Introduction	1
1.1. Blood	1
1.2. Dynamics of Erythrocytes in Shear flow	3
1.3. Mathematical models for tank-treading and tumbling	4
1.3.1. Keller and Skalak model [11]	4
1.3.2. Limitations of Keller and Skalak model	8
1.3.3. Skotheim and Secomb's model [12]	10
1.3.4. Limitations of Skotheim and Secomb model	11
1.4. Scope of the thesis	13
2. Numerical Methodology	15
2.1. Flow Configuration and Simulation Technique	15

2.1.1.	Problem setup	15
2.1.2.	Fluid-structure interaction	16
2.1.3.	Numerical treatment of membrane deformation	19
2.1.4.	Flow solver	20
2.1.5.	Interface tracking	21
3.	Effect of Deformation on Capsule Dynamics	23
3.1.	Introduction	23
3.1.1.	Dimensionless parameters	24
3.2.	Capsule Dynamics at Low Shear	25
3.3.	Capsule Dynamics at High Shear	48
4.	Rheology of a Dilute Suspension of Liquid-filled Elastic Capsules	53
4.1.	Introduction	53
4.2.	Methodology	55
4.3.	Results	58
4.3.1.	Capsule shape and orientation	58
4.3.2.	Shear stress	61
4.3.3.	Effect of area dilatation	70
4.3.4.	Normal stress differences	75
5.	Conclusion	87
5.1.	Dynamics of Ellipsoidal Capsules	87
5.2.	Rheology of Dilute suspension of Capsules	91

References	94
----------------------	----

List of Tables

1.1. Summary of the membrane properties.	3
--	---

List of Figures

1.1. (a) Image showing red blood cells. (b) Schematic of the cross-section of an RBC showing its dimensions and the typical values of hemoglobin and plasma viscosities. The image to its right is the zoomed view of a slice of the RBC membrane. Source: http://www.wellcome.ac.uk	2
1.2. Schematic showing the a) tank-treading motion and b) tumbling motion of a capsule in shear flow.	4
1.3. Experimental observations of tank-treading and tumbling motions in red blood cells. Shear flow is in the x-direction in both cases. A) Observations of tank-treading motion with a time interval of 40 ms by Fischer <i>et al.</i> [4] B) Observations of tumbling motion with a time sequence of 1 s by Abkarian <i>et al.</i> [5].	5
1.4. Schematic showing a capsule in shear flow. Here θ is the inclination angle of the major axis with the flow direction (x), and ϕ is the phase angle of a surface Lagrangian point. $0 < \theta < \pi/2$ is the extensional quadrant, and $-\pi/2 < \theta < 0$ is the compressional quadrant of the shear flow $\mathbf{u} = \{\dot{\gamma}y, 0, 0\}$	6

1.5. Steady state inclination angle θ^* w.r.t. the viscosity ratio λ as predicted by KS theory for four cases. The solid line, dashed line, dash dot line and dotted lines represent $\alpha = 0.6, 0.7, 0.8$ and 0.9 respectively.	8
1.6. Critical viscosity ratio w.r.t. the aspect ratio α of the particle.	9
1.7. Experimental observations by Abkarian <i>et al.</i> [5]. (A) RBC swinging ($\dot{\gamma} = 1.33 \text{ s}^{-1}$ and time sequence of 2 s). (B) Rotation of a bead stuck on the membrane of a RBC ($\dot{\gamma} = 6 \text{ s}^{-1}$ and time sequence of 1 s). (C) Transition from swinging to tumbling induced by decreasing shear rate is associated with a transient localized deformation ($\dot{\gamma} = 2.66 \text{ s}^{-1}$ and time sequence of 1 s).	10
1.8. Snapshots of a vacillating vesicle by Deschamps <i>et al.</i> [10].	12
2.1. Three-dimensional flow domain for simulating capsule deformation.	16
2.2. The Eulerian and Lagrangian grids and region of the distribution of nodal forces.	17

- 3.1. (Color online). Capsule dynamics at ‘low shear’ ($\text{Ca} = 0.05$) showing oscillatory (OS), vacillating-breathing (VB) and tumbling (TU) motions. Left panel shows the inclination angle $\theta(t)$ (solid black line) and the deformation parameter D (dash red line). The black dotted line is $D_o = D(t = 0)$. Right panel shows the semi-major (L , red solid line) and minor (B , green solid line) axes, and the half axis length in the vorticity direction (Z , dash blue line). All lengths are scaled by a , and time by $1/\dot{\gamma}$. Note that $(L - B)_{\min}$ and D_{\min} are nearly zero for the VB case shown in (b). 26
- 3.2. (Color online). Phase angle $\phi(t)$ for the three cases shown in Fig. 3.2. $\lambda = 3$, solid line; $\lambda = 7$, dash line; $\lambda = 10$, dotted line. 27
- 3.3. Instantaneous shapes for the oscillatory (OS), vacillating-breathing (VB) and tumbling (TU) motion at $\text{Ca} = 0.05$. For all cases, $\alpha = 0.7$. From top to bottom, λ varies as 3, 7, and 10 (compare with Fig. 3.1). 29
- 3.4. (Color online). Principal tension (in arbitrary unit) T_2^P for the (a) oscillatory (OS), (b) vacillating-breathing (VB), and (c) tumbling (TU) motion at $\text{Ca} = 0.05$. For all cases, $\alpha = 0.7$. From top to bottom, λ varies as 3, 7, and 10 (compare with Fig. 3.1). 32

3.5.	(Color online). (a) Inclination angle $\theta(t)$ at which D is maximum, and (b) $\theta(t)$ at which D is minimum, as a function of the viscosity contrast λ for different values of α and Ca. Here $\alpha = 0.6$ (green), 0.7 (red), and 0.9 (black). Symbols represent Ca = 0.05 (squares), 0.1 (delta), and 0.2 (circles).	34
3.6.	(Color online). Amplitude of shape deformation ΔD (top), and minimum of $(L-B)$ (bottom) as a function of the viscosity contrast λ for different values of α and Ca.	36
3.7.	(Color online). Average inclination angle θ_o as a function of λ for (a) $\alpha = 0.6$, and (b) $\alpha = 0.9$. Symbols and/or solid lines are the numerical results. Dash line is the KS theory (KS).	38
3.8.	(Color online). Variation of θ_o with respect to Ca. Symbols and solid lines are the numerical results. Dash lines are based on the SS theory.	39
3.9.	(Color online). Asymmetry in $\theta(t)$ shown by τ_2/τ_1 as a function of the viscosity contrast λ for different capillary numbers and aspect ratio. Various runs are as follows: $\text{---}\square\text{---}$ $\alpha = 0.6$, Ca = 0.05; $\text{---}\Delta\text{---}$ $\alpha = 0.6$, Ca = 0.1; $\text{---}\circ\text{---}$ $\alpha = 0.6$, Ca = 0.2; $\text{---}\Delta\text{---}$ $\alpha = 0.7$, Ca = 0.1; $\text{---}\square\text{---}$ $\alpha = 0.9$, Ca = 0.05. Inset shows how τ_1 and τ_2 are obtained from $\theta(t)$ for the OS and TU cases. KS: the Keller-Skalak theory.	40

- 3.10. (Color online). Amplitude of oscillation of the inclination angle w.r.t. (a) λ , and (b) Ca. In (a), numerical results are shown by symbols and solid lines (green circle Ca = 0.05, red square Ca = 0.1, blue delta Ca = 0.2). The dash-dot line is the result of the SS model for $1/U_e = 5$. All results are for $\alpha = 0.7$. In (b) the numerical results are for $\lambda = 4$ (circle) and $\lambda = 2$ (X). The dash line is the result for the SS model at $\lambda = 4$. All results are for $\alpha = 0.6$ 42
- 3.11. (Color online). (a) Variation of the semi-major (L , filled symbols) and minor (B , open symbols) axes w.r.t the inclination angle θ . Symbols are as follows. OS case: red circles ($\alpha = 0.7$, Ca = 0.05, $\lambda = 4$). VB case: green squares ($\alpha = 0.7$, Ca = 0.05, $\lambda = 7$). TU cases: blue diamond ($\alpha = 0.7$, Ca = 0.05, $\lambda = 10$), and black delta ($\alpha = 0.6$, Ca = 0.05, $\lambda = 7$). (b) dL/dt (filled symbols) and dB/dt (open symbols) for the similar cases as in (a). 44

- 3.12. (Color online). Angular velocity $\dot{\theta}$. Results for OS cases: right and left arrows imply θ going from θ_{\min} to θ_{\max} , and θ_{\max} to θ_{\min} , for which $\dot{\theta}$ is positive and negative, respectively. Symbols are numerical results for $\alpha = 0.7$ for $\text{Ca} = 0.05$, $\lambda = 3$ (red X), $\text{Ca} = 0.05$, $\lambda = 5$ (blue \diamond), $\text{Ca} = 0.2$, $\lambda = 3$ (black +). Lines are the SS theory for $1/U_e = 2$, $\lambda = 3$ (solid red line), $1/U_e = 2$, $\lambda = 5$ (dash red line), $1/U_e = 8$, $\lambda = 3$ (solid black line). First two SS cases (solid red line and dash red line) nearly overlap in the figure. 46
- 3.13. (Color online). Angular velocity $\dot{\theta}$. Results for TU cases: Symbols are numerical results for $\alpha = 0.7$ for $\text{Ca} = 0.05$, $\lambda = 10$ (green squares), and $\text{Ca} = 0.02$, $\lambda = 5$ (blue squares). Solid black line is the KS theory for $\alpha = 0.7$, $\lambda = 10$. Dash and dash-dot black lines are the SS theory for $\alpha = 0.7$ for $1/U_e = 1$, $\lambda = 10$, and $1/U_e = 1.43$, $\lambda = 5$, respectively. 47
- 3.14. (Color online). Capsule dynamics at ‘high shear’ for $\alpha = 0.7$. (a) $\text{Ca} = 0.2$, $\lambda = 13$; (b) $\text{Ca} = 0.4$, $\lambda = 9$; (c) $\text{Ca} = 0.4$, $\lambda = 13$. Left panel shows the inclination angle $\theta(t)$ (black line), and deformation parameter D (green line). Right panel shows semi-major and minor axes lengths, L (red line) and B (green line). 49
- 3.15. (Color online). Phase diagrams showing different regimes of capsule dynamics for (a) $\alpha = 0.7$, and (b) 0.9 51

4.1.	(Color online) Sample results for spherical capsules with SK model ($C = 1$). (a) and (b) show the final shapes for $\text{Ca} = 0.6$, $\lambda = 1$ and $\text{Ca}=0.6$, $\lambda = 13$, respectively. (c) Time-dependent Taylor deformation parameter D (left axis, and continuous lines) and inclination angle θ (right axis, and dash lines) for two cases: $\text{Ca} = 0.6$, $\lambda = 1$ (thin lines), and $\text{Ca}=0.6$, $\lambda = 13$ (thick lines). (d) Time-dependent particle stress components Σ_{xy} (black lines, left axis), N_1 (red lines, left axis), and N_2 (blue lines, right axis) for two cases: $\text{Ca} = 0.6$, $\lambda = 1$ (continuous lines), and $\text{Ca}=0.6$, $\lambda = 13$ (dotted lines). . . .	59
4.2.	Steady-state values of the Taylor deformation parameter D (left axis, and lines with symbols) and the inclination angle θ (right axis, and lines without symbols) for capsules with SK model ($C = 1$). $\lambda = 1$ (continuous lines), 5 (dash lines), and 10 (dotted lines). . .	60
4.3.	Particle shear stress Σ_{xy} for capsules with SK model ($C = 1$). (a) Effect of Ca at constant λ , and (b) effect of λ at constant Ca . . .	62
4.4.	Particle shear stress Σ_{xy} for capsules with NH model. (a) Effect of Ca at constant λ , and (b) effect of λ at Ca	64
4.5.	(Color online) Elastic (Σ_{xy}^{el}) and viscous (Σ_{xy}^{vis}) components with varying Ca for different values of λ for SK model with $C = 1$. Symbols have same meanings in (a) and (b).	65

4.6.	Elastic (Σ_{xy}^{el}) and viscous (Σ_{xy}^{vis}) components with varying λ for different Ca for SK model with $C = 1$. Symbols have same meanings in (a) and (b).	66
4.7.	(Color online) Variation of $\Sigma_{xy}^{\text{el,iso}}$ (solid, black lines), and $\Sigma_{xy}^{\text{vis,geom}}$ (dash red lines) as functions of inclination angle θ for shape-preserving oblate spheroids for aspect ratios 1 (no symbol), 1.25 (triangles), and 1.67 (circles).	68
4.8.	Effect of area dilatation on (a) capsule deformation and (b) inclination angle. Symbols represent NH model (Δ), and SK models with $C = 0.1$ (\diamond), 1 (\square), 50 (\circ), and 100 (\triangleright).	70
4.9.	Effect of area dilatation on Σ_{xy} . (a) variation with respect to Ca at $\lambda = 1$; and (b) variation with respect to λ at Ca = 0.4. Symbols represent NH model (Δ), and SK models with $C = 0.1$ (\diamond), 1 (\square), and 50 (\circ).	72
4.10.	(Color online) Effect of area dilatation on Σ_{xy}^{el} and Σ_{xy}^{vis} . Symbols represent NH model (Δ), and SK models with $C = 0.1$ (\diamond), 1 (\square), and 50 (\circ). (a) Variation of Σ_{xy}^{el} (continuous lines) and Σ_{xy}^{vis} (dash lines) with λ at Ca = 0.4. (b) Variation of Σ_{xy}^{sh} (long dash lines) and Σ_{xy}^{di} (dash-dot lines) with λ at Ca = 0.4. (c) Variation of Σ_{xy}^{sh} (long dash lines) and Σ_{xy}^{di} (dash-dot lines) with Ca at $\lambda = 1$	74

4.11. (Color online) N_1 and N_2 for capsules with SK model ($C = 1$). $\lambda = 1$ (thick red lines), 3 (thin red lines), 5 (dash red lines), 7 (black dash-dot lines), 10 (blue dotted lines), and 13 (black dash- dot-dot lines).	76
4.12. (Color online) Effect of Ca on the elastic contributions (a) N_1^{el} , and (b) N_2^{el} for SK model with $C = 1$. Line patterns represent different values of λ as in Fig. 4.11. $\lambda = 1$ (thick red lines), 3 (thin red lines), 5 (dash red lines), 7 (black dash-dot lines), 10 (blue dotted lines), and 13 (black dash-dot-dot lines).	77
4.13. (Color online) Effect of λ on the elastic contributions (a) N_1^{el} , and (b) N_2^{el} for SK model with $C = 1$. Line patterns represent different values of Ca as indicated.	79
4.14. Variation of $N_1^{\text{el,iso}}$ (red dash lines) and $N_2^{\text{el,iso}}$ (blue dash-dot lines) as functions of inclination angle θ for shape-preserving oblate spheroids for aspect ratios 1 (no symbol), 1.25 (triangles), and 1.67 (circles).	80
4.15. (Color online) Distribution of the principal membrane tensions τ_1 and τ_2 for $\lambda = 1$ for two capillary numbers 0.05 (a,b) and 0.4 (c,d). The color changes from red to blue as the values change from positive to negative, respectively. The contour ranges are indicated for each case.	82
4.16. (Color online) Same as in Fig. 4.15 but for $\lambda = 7$, and Ca = 0.05 (a,b) and 0.4 (c,d).	83

4.17. (Color online) Effect of Ca on the viscous contributions (a) N_1^{vis} , and (b) N_2^{vis} for SK model with $C = 1$. Line patterns represent different values of λ as in Fig. 4.11. $\lambda = 1$ (thick red lines), 3 (thin red lines), 5 (dash red lines), 7 (black dash-dot lines), 10 (blue dotted lines), and 13 (black dash-dot-dot lines).	84
4.18. Effect of area dilatation on N_1 (continuous line, left axis) and N_2 (dash lines, right axis). Variation with respect to Ca is shown at $\lambda = 1$. Symbols represent NH model (Δ), and SK models with $C = 0.1$ (\diamond), and 50 (\circ).	85

Chapter 1

Introduction

1.1 Blood

Human blood is a multiphase fluid comprising of red blood cells, white blood cells, and platelets suspended in a Newtonian liquid called plasma. Erythrocytes or red blood cells (shown in Fig. 1.1a) constitute the major particulate component of blood which is 40 – 45% by volume. Red blood cells are filled with a Newtonian liquid called hemoglobin, an iron-containing protein, which facilitates the transportation of oxygen to the tissues. The resting shape of an erythrocyte is a biconcave disk of diameter 8 microns, flattened and depressed in the center, with a dumbbell-shaped cross section as depicted in Fig. 1.1b. Their outer structure is made of a lipid bilayer and a two-dimensional network of spectrin filaments [1,2]. It shows resistance to any change in surface area and has bending stiffness. This structure gives the cell an extreme flexibility, a unique characteristic which, in a major way, determines the dynamics and rheology of blood. Understanding the dynamics of erythrocytes in flow is fundamental to understanding the complex motion of blood in vivo and in vitro.

Modeling of the whole cell on the molecular level is however prohibitive if

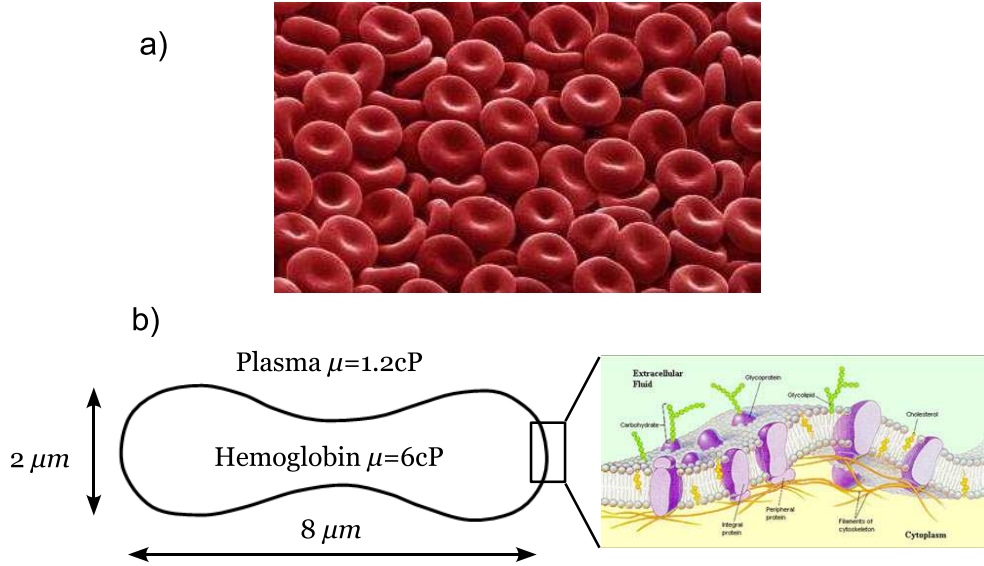


Figure 1.1: (a) Image showing red blood cells. (b) Schematic of the cross-section of an RBC showing its dimensions and the typical values of hemoglobin and plasma viscosities. The image to its right is the zoomed view of a slice of the RBC membrane. Source: <http://www.wellcome.ac.uk>

interaction among multiple cells are considered, or the long-time dynamics of individual cell is of interest. At typical length scales of the cells, the bilayer-cytoskeleton complex can be modeled as a zero-thickness elastic membrane. Continuum approaches then become useful by modeling the cells as either capsules or vesicles. A capsule is a viscous drop enclosed by thin elastic membrane. A vesicle is a liquid viscous droplet enclosed by a phospholipid bilayer membrane. Unlike a capsule, a vesicle does not have the shear resistance; rather it has a bending resistance, and its surface area and volume are conserved. Typically four quantities determine the mechanical behavior of such deformable particles - the viscosity contrast, the shear and extensional moduli of the membrane, and the bending

	Capsules	Vesicles	RBCs
Shear Resistance	✓		✓
Bending Resistance		✓	✓
Constant Surface Area		✓	✓
Constant Volume	✓	✓	✓
Viscosity Contrast	✓	✓	✓

Table 1.1: Summary of the membrane properties.

resistance. Accurate description of the dynamics of these capsules or vesicles based on theoretical models might also provide a sensitive way of measuring their mechanical properties.

1.2 Dynamics of Erythrocytes in Shear flow

Erythrocytes, or their simplified models, capsules and vesicles, exhibit complex dynamics when subject to a shear flow. Early [3,4] and recent [5–10] experiments show primarily two types of motion of the particle - tank-treading and tumbling.

Tank-treading is the motion of the particle in which it inclines at a steady angle with the flow direction while the interior liquid and the membrane make a continuous rotation. This is illustrated in Fig. 1.2a using a lagrangian point on surface of an ellipsoidal particle. With the passage of time, this point moves on the surface of the particle while the particle maintains its shape and orientation with the horizontal. In tumbling motion, the cell flips like a rigid body and the membrane tank-treading ceases. Therefore any point on the membrane stays at the same location relative to the particle irrespective of the particle's orientation. Experimental observations of both these kinds of motion are shown in Fig. 1.3.

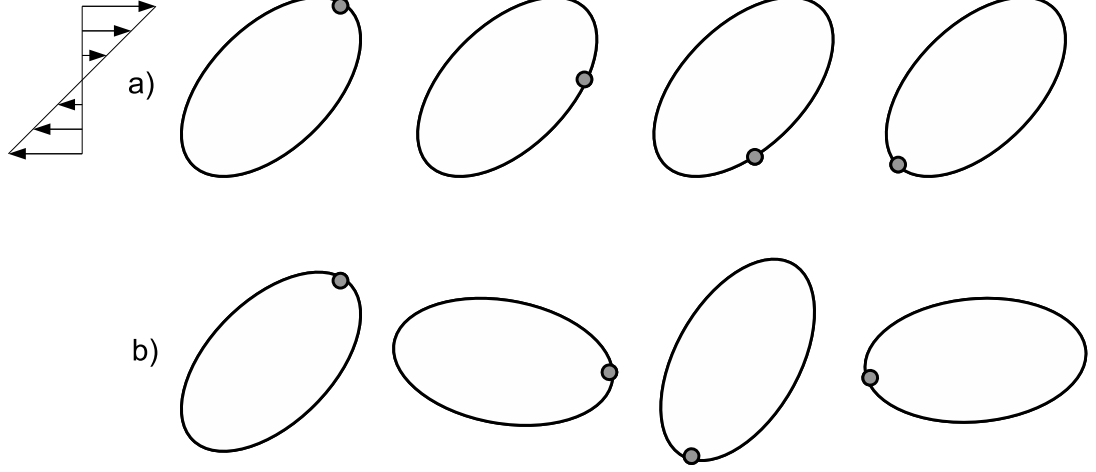


Figure 1.2: Schematic showing the a) tank-treading motion and b) tumbling motion of a capsule in shear flow.

1.3 Mathematical models for tank-treading and tumbling

1.3.1 Keller and Skalak model [11]

The tank-treading and tumbling motion of a particle in a shear flow $\mathbf{u} = \{\dot{\gamma}y, 0, 0\}$ can be predicted analytically by the Keller-Skalak (KS) theory [11]. In the KS model, the particle is assumed to be a shape-preserving ellipsoid of semi-major and minor axes lengths L and B enclosed by an inextensible membrane. The viscosity of the internal fluid is $\lambda\mu_o$, and the particle is immersed in a fluid of viscosity μ_o (Fig. 1.4). Both fluids are assumed to be incompressible Newtonian liquids. The membrane is assumed to have zero shear viscosity. The motion of the particle is determined by equilibrium and energy conditions.

From the equilibrium considerations KS model predicts that the only non-zero

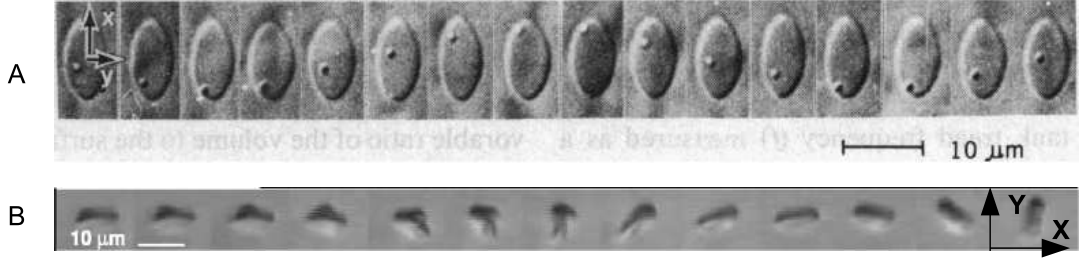


Figure 1.3: Experimental observations of tank-treading and tumbling motions in red blood cells. Shear flow is in the x -direction in both cases. A) Observations of tank-treading motion with a time interval of 40 ms by Fischer *et al.* [4] B) Observations of tumbling motion with a time sequence of 1 s by Abkarian *et al.* [5].

moment on the particle, M_3 is given by,

$$M_3 = M_3^S + M_3^F + M_3^T \quad (1.1)$$

where, M_3^S is the moment due to shear flow acting on a stationary rigid ellipsoid inclined at an angle θ , M_3^F is the moment acting on a rigid ellipsoid flipping about the x_3 axis with angular speed $\dot{\theta}$ in a fluid at rest at infinity and M_3^T is the moment acting on a stationary ellipsoid undergoing the tank-treading motion in an otherwise quiescent liquid.

Assuming that there are no external forces or moments, and that inertial effects are negligible, equilibrium requires $M_3 = 0$. This gives the following

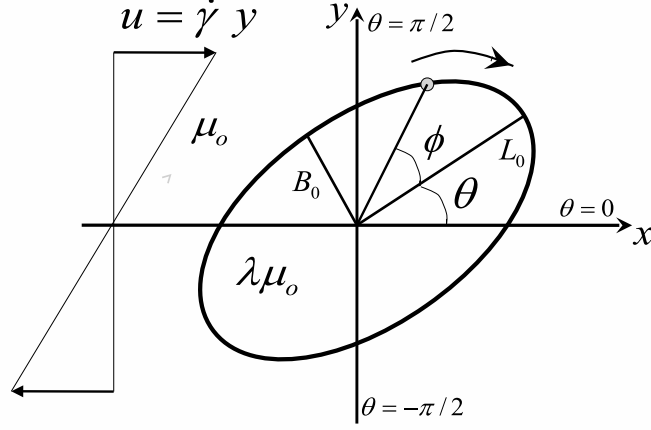


Figure 1.4: Schematic showing a capsule in shear flow. Here θ is the inclination angle of the major axis with the flow direction (x), and ϕ is the phase angle of a surface Lagrangian point. $0 < \theta < \pi/2$ is the extensional quadrant, and $-\pi/2 < \theta < 0$ is the compressional quadrant of the shear flow $\mathbf{u} = \{\dot{\gamma}y, 0, 0\}$.

equations of motion.

$$\dot{\theta} = \tilde{A} + \tilde{B} \cos 2\theta, \quad (1.2)$$

where,

$$\tilde{A} = - \left(\frac{1}{2} \dot{\gamma} + \frac{2LB}{L^2 + B^2} \dot{\phi} \right) \quad (1.3)$$

$$\tilde{B} = \frac{1}{2} \dot{\gamma} \frac{L^2 - B^2}{L^2 + B^2}. \quad (1.4)$$

It is to be noted that these equations do not depend on a_3 and the viscosity

of the outer liquid μ . In addition to these equilibrium equations, energy considerations impose further constraints on the motion of the particle. Conservation of energy requires that the total work done by the external fluid on the particle is equal to the energy dissipation in the membrane and the internal fluid combined. However, KS model neglects the dissipation in the membrane for the sake of simplicity.

Thus using the energy conditions, we arrive at the following final set of equations describing capsule dynamics.

$$\dot{\theta} = -\frac{\dot{\gamma}}{2} - \frac{2LB}{L^2 + B^2}\dot{\phi} + \frac{\dot{\gamma}}{2} \frac{L^2 - B^2}{L^2 + B^2} \cos 2\theta, \quad (1.5)$$

$$\dot{\phi} = -\frac{\dot{\gamma}f_3}{f_2 - \lambda f_1} \cos 2\theta \quad (1.6)$$

where f_1, f_2 and f_3 are dimensionless, and they depend on the axes ratios [11,12]. The steady state inclination angle θ^* of the major axis of the capsule in tank-treading mode can be found by equating the Eq. 1.2 to zero.

$$\theta^* = \frac{1}{2} \arccos \left(-\frac{A}{B} \right) \quad (1.7)$$

Fig. 1.5 shows the steady state inclination angle of the major axis with respect to viscosity contrast of the particle for four aspect ratios i.e. $\alpha = 0.6, 0.7, 0.8$ and 0.9 . The viscosity ratio where the inclination angle becomes zero is called

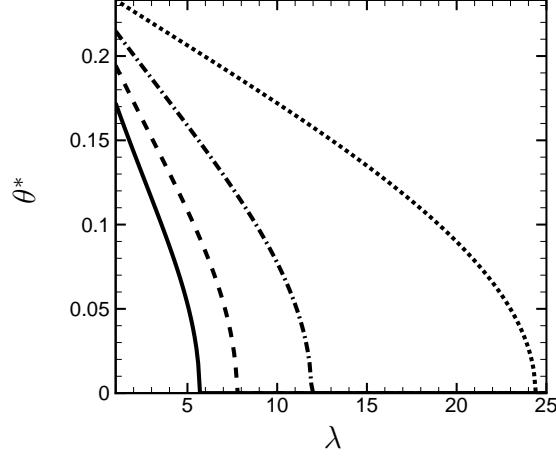


Figure 1.5: Steady state inclination angle θ^* w.r.t. the viscosity ratio λ as predicted by KS theory for four cases. The solid line, dashed line, dash dot line and dotted lines represent $\alpha = 0.6, 0.7, 0.8$ and 0.9 respectively.

critical viscosity ratio λ_c . It corresponds to the transition between tank-treading and tumbling modes. For a given geometry, the tank-treading motion is predicted when the viscosity contrast λ is less than a critical value λ_c , and the tumbling motion is predicted when $\lambda > \lambda_c$. λ_c depends on the aspect ratio of the particle. At $\lambda = \lambda_c$, $\theta^* = 0$. From this we get the following expression for λ_c .

$$\lambda_c = \frac{1}{f_1} \left[f_2 - \frac{2f_3}{\frac{1}{2} \left(r_2 + \frac{1}{r_2} \right) - z_1} \right] \quad (1.8)$$

Fig. 1.6 shows the variation of critical viscosity ratio with aspect ratio.

1.3.2 Limitations of Keller and Skalak model

The major limitations of the KS theory, among others, are that it assumes a shape-preserving particle, and that the results are independent of the shear rate.

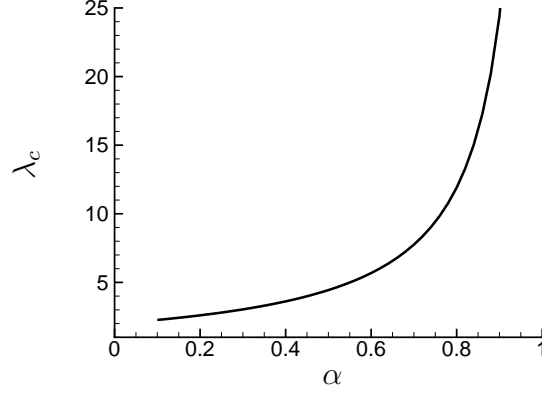


Figure 1.6: Critical viscosity ratio w.r.t. the aspect ratio α of the particle.

Erythrocytes, capsules and vesicles can undergo a large amplitude shape deformation in shear flow [3–10]. Analytical theories exist for capsules and vesicles in the limit of small deformation [13–15]. Numerical simulations are required when large deformation is considered which have successfully predicted the tank-treading and tumbling motions of capsules [16–19] and vesicles [20–25].

Recent experiments have suggested the existence of a swinging or oscillatory motion of red blood cells [5], nonspherical capsules [6], and vesicles [7, 8], in addition to the tank-treading and tumbling modes. Numerical simulations have also predicted swinging of capsules [18, 19] and vesicles [25]. Experiments by Abkarian *et al.* carried out on a red blood cell illustrate the swinging behavior. RBC's were suspended in a liquid of viscosity $\eta_0 = 47$ mPa.s and the shear rate was varied. For high shear values, RBC's exhibited a quasisteady tank-treading motion (shown in Fig. 1.7A) as previously reported [4]. When the shear rate was decreased, the RBC's inclination oscillated about a mean angle as shown in Fig.

1.7B. In addition, an intermediate regime was also observed where the particle alternatively oscillates and tumbles. However, it was not established conclusively due to experimental constraints.

Experiments [5] and simulations [18] have shown that the transition from tank-treading to tumbling of erythrocytes and capsules as seen from Fig. 1.7C can be triggered by decreasing the shear rate while the viscosity contrast remains a constant, thus departing from the KS theory. The oscillatory dynamics and the shear-dependent transition are recently addressed theoretically by Skotheim and Secomb (SS) [12] within the framework of the KS theory.

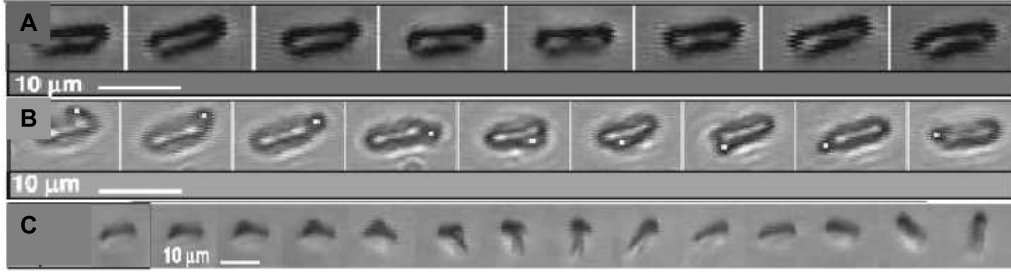


Figure 1.7: Experimental observations by Abkarian *et al.* [5]. (A) RBC swinging ($\dot{\gamma} = 1.33 \text{ s}^{-1}$ and time sequence of 2 s). (B) Rotation of a bead stuck on the membrane of a RBC ($\dot{\gamma} = 6 \text{ s}^{-1}$ and time sequence of 1 s). (C) Transition from swinging to tumbling induced by decreasing shear rate is associated with a transient localized deformation ($\dot{\gamma} = 2.66 \text{ s}^{-1}$ and time sequence of 1 s).

1.3.3 Skotheim and Secomb's model [12]

Skotheim and Secomb's [12] model considers the same problem of capsule deformation as described in the section 1.3.1. Further, it takes into account the

deformation of the capsules by introducing an additional elastic energy term of the form $E = E_o \sin^2 \phi$ into the equations 1.5 and 1.6. From the conservation of energy, work done by the external liquid on the capsule is equal to the dissipation inside the capsule plus change in its membrane elastic energy. This gives the following conservation equation -

$$V\mu_0 (f_2 \partial_t \phi^2 + f_3 \dot{\gamma} \partial_t \phi \cos 2\theta) = V\mu f_1 \partial_t \phi^2 + E_o \sin(2\phi) \partial_t \phi \quad (1.9)$$

Solving for $\dot{\phi}$ from this gives the following modified form of equation 1.6

$$\dot{\phi} = \frac{f_3 \dot{\gamma}}{(f_2 - \lambda f_1)} (U_e \sin 2\phi - \cos 2\theta) \quad (1.10)$$

where, $U_e = E_o/V\mu_o\dot{\gamma}f_3$, and V is the volume of the particle. U_e is the ratio of the change in the elastic energy to the work done by the external fluid during the rotation. It signifies the stiffness of the capsule relative to the external shear flow. By incorporating the elastic energy term into the KS model, SS model can successfully predict the shear-dependent dynamics and the intermittent behavior of the particle between tank-treading and tumbling modes observed by Abkarian *et al.* [5].

1.3.4 Limitations of Skotheim and Secomb model

Though the SS model can predict the shear-rate dependent transition from tank-treading to tumbling, it neglects large deformation in shape. Experiments on

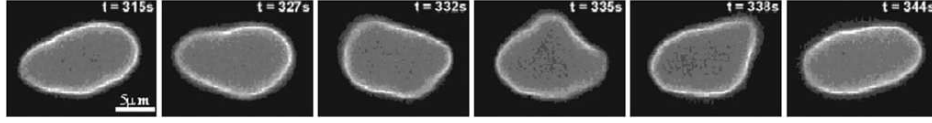


Figure 1.8: Snapshots of a vacillating vesicle by Deschamps *et al.* [10].

viscous vesicles have shown that the shape deformation plays a very significant role in the inclination and transition dynamics [9, 10]. A vacillating-breathing mode of vesicles has been observed experimentally [8–10], and predicted analytically [14, 15, 26, 27] and numerically [24, 25].

Vacillating-breathing mode appears in the vicinity of $\lambda = \lambda_c$, and is characterized by the vesicle swinging about its mean inclination angle $\theta_0 \approx 0$ accompanied by a large amplitude shape deformation. Fig. 1.8 shows snapshots of a vacillating vesicle by Deschamps *et al.* [10]. Initially it is in the elongated ellipsoidal shape. Slowly it undergoes strong shape deformation to almost a sphere and then regains back its original shape.

It appears, therefore, that the shape deformation plays a major role in inclination and transition dynamics of vesicles and capsules, and most likely for erythrocytes, despite the differences in their mechanical characteristics [28]. Both the KS and SS theories neglect the influence of deformability. Experiments have shown that even in the pure tumbling mode, the shape deformation makes $\theta(t)$ deviate from that predicted by the KS theory [9]. Understanding the influence of shape deformation on the transition dynamics of capsules and vesicles

is receiving a growing interest in recent years using state-of-the-art experimental [7–10] and computational [18–25, 29], approaches, and higher-order analytical theories [14, 15, 26, 27, 30].

1.4 Scope of the thesis

The thesis is divided into two parts as follows:

Role of deformation on the capsule dynamics

In the first part (chapter 3), we focus on the dynamics of capsules with initially oblate shapes. Using three-dimensional numerical simulations of capsules in large deformation, we present results over a broad range of the parameters, namely, viscosity contrast, shear rate, and aspect ratio. Our main objective is

(i) to further improve our understanding of the coupling between the shape deformation and orientation dynamics, and,

(ii) to show how this coupling influences the transition from tank-treading to tumbling motion, and leads to significant departures from the KS and SS theories. The emphasis is on how the dynamics changes, with increasing viscosity contrast, from the oscillating to vacillating-breathing to tumbling motions when large shape deformation is considered.

Rheology of dilute suspensions of capsules

In the second part (chapter 4), we extend our understanding of capsule dynamics to the study of rheology of suspension of spherical capsules. We consider capsules of spherical resting shape for which only a steady tank-treading motion

is observed. A comprehensive analysis of the suspension rheology is presented over a broad range of viscosity ratio (ratio of internal-to-external fluid viscosity), shear rate (or, capillary number), and capsule surface area dilatation. It is shown that the suspension exhibits a shear viscosity minimum at moderate values of the viscosity ratio, and high capillary numbers. The normal stress differences are shown to decrease with increasing capillary number at high viscosity ratios. Such non-trivial results neither can be predicted by the small-deformation theory, nor can be explained by the capsule geometry alone. Physical mechanisms underlying these novel results are studied by decomposing the particle stress tensor into a contribution due to the elastic stresses in the capsule membrane, and a contribution due to the viscosity differences between the internal and suspending fluids. It is shown that the elastic contribution is shear-thinning, but the viscous contribution is shear-thickening. The coupling between the capsule geometry, and the elastic and viscous contributions is analysed to explain the observed trends in the bulk rheology.

Chapter 2

Numerical Methodology

2.1 Flow Configuration and Simulation Technique

2.1.1 Problem setup

We consider a three-dimensional computational domain shown in Fig. 2.1 for studying the dynamics of single capsule deformation. The domain is bounded by two infinite flat plates placed parallel to the X -axis in the XYZ coordinate system as shown. The height of the channel is H . In absence of a capsule, we have linear shear flow at zero pressure-gradient driven by the two walls of the channel as

$$\mathbf{u}_0 = [\dot{\gamma}Y, 0, 0], \quad (2.1)$$

where $\dot{\gamma}$ is the shear rate. Here Z is the direction of vorticity of the undisturbed flow. The channel is assumed to be infinitely long in the X and Z directions. We use periodic boundary conditions in these directions to reduce the size of the computational domain. This also allows us to use Fourier transforms for accelerating the computation.

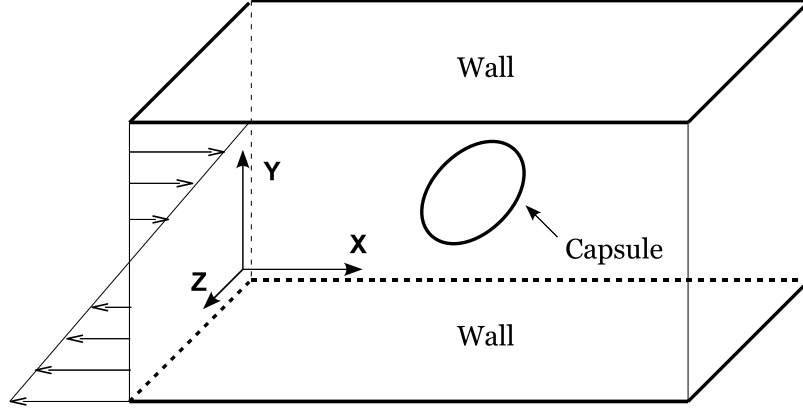


Figure 2.1: Three-dimensional flow domain for simulating capsule deformation.

The initial undeformed shape of the capsule can be spherical, ellipsoidal or biconcave. However, in the present work, we consider only spherical or ellipsoidal shapes. The particle is placed at the center of the cubical domain. The resting shape of the capsule can be specified using a dimensionless parameter called aspect ratio, α which is defined as the ratio of the minor axis to the major axis. Aspect ratio can theoretically vary from 0 to 1 depending on whether the particle is a thin rod or a sphere.

2.1.2 Fluid-structure interaction

We model capsules as liquid drops surrounded by infinitesimally thin elastic membranes. The simulation technique considered here is the front-tracking/immersed boundary method (Peskin *et al.* [31]; Unverdi & Tryggvason [32]; Tryggvason *et al.* [33]) for multiple fluids with different properties. The main idea of the front-tracking method is to use a single set of equations for both the fluids, inside and

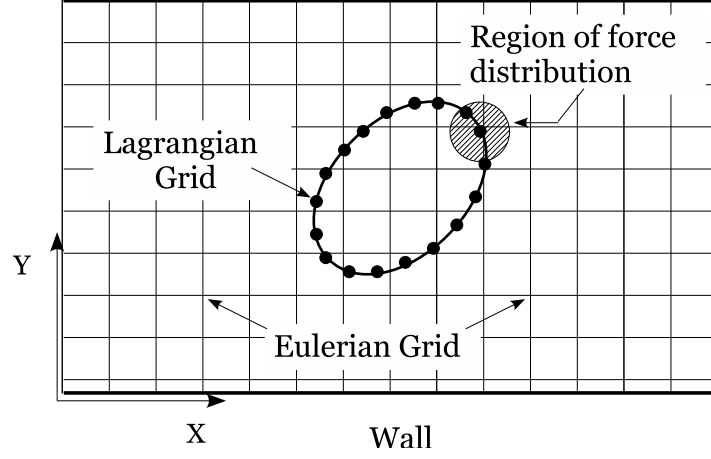


Figure 2.2: The Eulerian and Lagrangian grids and region of the distribution of nodal forces.

outside of the capsule. The fluid equations are solved on a fixed Eulerian grid, and the interface is tracked in a Lagrangian manner by a set of marker points as seen from Fig. 2.2. All the fluids inside and outside the capsule are considered to be incompressible. Therefore, the fluid motion is governed by the continuity and Navier-Stokes equations as:

$$\nabla \cdot \mathbf{u} = 0, \quad (2.2)$$

$$\rho \left[\frac{\partial \mathbf{u}}{\partial t} + \mathbf{u} \cdot \nabla \mathbf{u} \right] = -\nabla p + \nabla \cdot \mu (\nabla \mathbf{u} + (\nabla \mathbf{u})^T) \quad (2.3)$$

where $\mathbf{u}(\mathbf{x}, t)$ is the fluid velocity, ρ is density, p is pressure, and μ is the viscosity. Here $\mu(\mathbf{x}, t)$ is a single variable used to denote the viscosity of the entire fluid. Therefore, $\mu = \mu_c$ inside the capsule and $\mu = \mu_0$ outside. It is mathematically defined using an indicator function $I(x)$ which is unity inside the capsule and zero

outside. Thus, μ is given by a single expression for every point in the fluid as

$$\mu(x) = \mu_0 + (\mu_c - \mu_0)I(\mathbf{x}). \quad (2.4)$$

The capsule surface is then recognized by adding a source-like term \mathbf{F} to the right hand side of the equation 2.3. The force on the capsule surface is \mathbf{f} the elastic force which arises due to its deformation. The source term \mathbf{F} is related to \mathbf{f} as

$$\mathbf{F}(\mathbf{x}, t) = \int_{\partial S} \mathbf{f}(\mathbf{x}', t) \delta(\mathbf{x} - \mathbf{x}') d\mathbf{x}'. \quad (2.5)$$

Here \mathbf{x} is a point in the flow domain, \mathbf{x}' is a point on the capsule-fluid interface ∂S , and δ is the Delta function which vanishes everywhere except on the membrane.

The δ function used in equation 2.5 is constructed by multiplying three 1D δ functions as

$$\delta(\mathbf{x} - \mathbf{x}') = \delta(x - x')\delta(y - y')\delta(z - z'). \quad (2.6)$$

For numerical implementation, a smooth representation of the δ -function is used as

$$\begin{aligned} D(\mathbf{x} - \mathbf{x}') &= \frac{1}{64\Delta^3} \prod_{i=1}^3 \left(1 + \cos \frac{\pi}{2\Delta}(x_i - x'_i) \right) \quad \text{for } |x_i - x'_i| \leq 2\Delta, \quad i = 1, 2, 3, \\ D(\mathbf{x} - \mathbf{x}') &= 0 \quad \text{otherwise,} \end{aligned} \quad (2.7)$$

where Δ is the Eulerian grid size (Unverdi & Tryggvason [32]). As a result, the membrane force varies smoothly over four Eulerian grid points surrounding the

interface. In discrete form, the integral in equation 2.5 can be written as

$$\mathbf{F}(\mathbf{x}_j) = \sum_i D(\mathbf{x}_j - \mathbf{x}'_i) \mathbf{f}(\mathbf{x}'_i) \quad (2.8)$$

where i and j represent Lagrangian and Eulerian points, respectively.

2.1.3 Numerical treatment of membrane deformation

The constitutive law governing the capsule membrane is described by a strain energy function W due to Skalak *et al.* [34] as

$$W = \frac{E_s}{12} [I_1^2 + 2(I_1 - I_2)] + \frac{E_a}{12} I_2^2 \quad (2.9)$$

where $I_1 = \epsilon_1^2 + \epsilon_2^2 - 2$ and $I_2 = \epsilon_1^2 \epsilon_2^2 - 1$ are the surface strain invariants. ϵ_1 and ϵ_2 are the principal stretch ratios and E_s and E_a are the shear elasticity and area dilatation moduli, respectively. The first term in the right hand side of Eq. 2.9 represents the shear resistance of the membrane, while the second term represents the resistance against area dilatation. The membrane is nearly incompressible when $E_a \gg E_s$. In our simulations, the ratio $C = E_a/E_s$ is fixed at unity. Thus the area incompressibility condition of the membrane is not satisfied. We assume that the bending resistance of the membrane is negligible. The elastic forces acting on the three vertices of a triangular element are obtained from the strain energy function W using the principal of virtual work as $\mathbf{f}(\mathbf{x}', t) = -\partial W / \partial \mathbf{x}'$.

The deformation of the membrane is treated using a finite element model

developed by Charrier *et al.* [35]; Shrivastava & Tang [36]), and later implemented by Eggleton & Popel [37] within the framework of immersed boundary method to consider large deformation of capsules. First, the membrane is discretized using flat triangular elements. The triangulated surface mesh needed for the simulations is obtained from the GNU Triangulated Surface (GTS) Library. GTS is an Open Source Free Software Library intended to provide a set of useful functions for scientists dealing with 3D computational surface meshes. The main idea is that a general 3D deformation of the membrane can be reduced to a 2D problem by assuming that individual triangular element on the membrane remains flat even after deformation. The forces acting on the three vertices of a triangular element are obtained by computing the displacements of the vertices of the deformed element with respect to the undeformed element. The details of the method can be found in Doddi [38], Doddi & Bagchi [39] and Doddi & Bagchi [40].

2.1.4 Flow solver

The Navier-Stokes equations are discretized spatially using a second-order finite difference scheme, and temporally using a two-step time-split scheme. In this method the momentum equation is split into an advection–diffusion equation and a Poisson equation for the pressure. The body-force term is retained in the advection–diffusion equation. The nonlinear terms are treated explicitly using a second-order Adams–Bashforth scheme, and the viscous terms are treated semi-implicitly using the second-order Crank–Nicholson scheme. The resulting linear

equations are inverted using an ADI (alternating direction implicit) scheme to yield a predicted velocity field. The Poisson equation is then solved to obtain pressure at the next time level. Using the new pressure, the velocity field is corrected so that it satisfies the divergence-free condition. Details of the time-step scheme can be found in Doddi [38], Doddi & Bagchi [39] and Doddi & Bagchi [40].

2.1.5 Interface tracking

The capsule membrane is tracked in a Lagrangian manner. After solving the Navier-Stokes equations for pressure and velocity fields, no-slip condition on the capsule surface is imposed by extracting the surface velocity from the surrounding fluid at each time step as

$$\mathbf{u}_S(\mathbf{x}', t) = \int_S \mathbf{u}(\mathbf{x}, t) \delta(\mathbf{x} - \mathbf{x}') d\mathbf{x}, \quad (2.10)$$

where S indicates the entire flow domain. Though the summation is over all Eulerian nodes, only the ‘local’ nodes contribute to the membrane velocity. The discrete form of the delta function used here is the same given by equation 2.6. In this way, a weighted interpolation of the Eulerian fluid velocity is performed which ensures that the continuity of velocity across the membrane is satisfied. The Lagrangian points on the membrane are then advected as

$$\frac{d\mathbf{x}'}{dt} = \mathbf{u}_S(\mathbf{x}', t). \quad (2.11)$$

Numerically, the above equation is treated explicitly using the second-order Adams-Bashforth scheme as

$$\mathbf{x}'_{n+1} = \mathbf{x}'_n + \Delta t \left[\frac{3}{2} \mathbf{u}_S(\mathbf{x}'_n) - \frac{1}{2} \mathbf{u}_S(\mathbf{x}'_{n-1}) \right], \quad (2.12)$$

where n , $n + 1$, etc. are the time instances.

As the capsule moves and deforms, μ needs to be updated. This is done by solving a Poisson equation for the indicator function $I(x, t)$ as

$$\nabla^2 I = \nabla \cdot \mathbf{G}, \quad (2.13)$$

where, $\mathbf{G} = \int_S \delta(\mathbf{x} - \mathbf{x}') \mathbf{n} d\mathbf{x}$, and \mathbf{n} is the unit vector normal to the capsule surface.

The inertia effect is considered small as the Reynolds number defined as $Re = \rho \dot{\gamma} a^2 / \mu \approx O(10^{-2})$. Typical Eulerian resolution used in this study is $80 \times 80 \times 80$, and Lagrangian resolution used is 5120 triangular elements. Dimensionless timestep used in the simulation is $O(10^{-4})$.

A detailed validation of the immersed boundary method, in the context of capsule deformation, is provided in Doddi [38], Doddi & Bagchi [39] and Doddi & Bagchi [40].

The results presented in the following chapters are from the publications [41] and [42].

Chapter 3

Effect of Deformation on Capsule Dynamics

3.1 Introduction

In this Chapter, three-dimensional numerical simulations using front-tracking method are presented on the dynamics of oblate shape capsules in linear shear flow by considering a broad range of viscosity contrast (ratio of internal-to-external fluid viscosity), shear rate (or, capillary number), and aspect ratio. We focus specifically on the coupling between the shape deformation and orientation dynamics of capsules, and show how this coupling influences the transition from the tank-treading to tumbling motion. At low capillary numbers, three distinct modes of motion are identified: a swinging or oscillatory (OS) mode at a low viscosity contrast in which the inclination angle $\theta(t)$ oscillates but always remains positive; a vacillating-breathing (VB) mode at a moderate viscosity contrast in which $\theta(t)$ periodically becomes positive and negative, but a full tumbling does not occur; and a pure tumbling mode (TU) at a higher viscosity contrast. At higher capillary numbers, three types of transient motions occur, in addition to the OS and TU modes, during which the capsule switches from one mode to the other as (i) VB to OS, (ii) TU to VB to OS, and (iii) TU to VB. Phase diagrams

showing various regimes of capsule dynamics are presented. For all modes of motion (OS, VB, TU), a large amplitude oscillation in capsule shape, and a strong coupling between the shape deformation and orientation dynamics are observed. It is shown that the coupling between the shape deformation and orientation is the strongest in the VB mode, and hence at a moderate viscosity contrast, for which the amplitude of shape deformation reaches its maximum. The numerical results are compared with the theories of Keller and Skalak, and Skotheim and Secomb. Significant departures from the two theories are discussed and related to the strong coupling between the shape deformation, inclination, and transition dynamics.

3.1.1 Dimensionless parameters

The shear rate of the undisturbed flow is given by $\dot{\gamma}$. The length scale is chosen to be the radius a of a sphere of equal volume as that of the oblate capsule. The governing equations are made dimensionless using a as the characteristic length scale, $1/\dot{\gamma}$ as the time scale, and $\dot{\gamma}a$ as the velocity scale. The dimensionless time is denoted by $t^* = \dot{\gamma}t$. Since deformation of the capsule occurs, the semi-major and minor axes lengths vary with time, and are denoted by $L(t)$ and $B(t)$. The half axis length in the vorticity direction is $Z(t)$. The Taylor deformation parameter D , is a dimensionless measure of capsule deformation. Major dimensionless parameters defined are:

$$\alpha = B_0/L_0, \tag{3.1}$$

$$\lambda = \mu/\mu_0, \quad (3.2)$$

$$Ca = \mu_0 \dot{\gamma} a / E_s, \quad (3.3)$$

$$D = (L - B)/(L + B). \quad (3.4)$$

where, α is the aspect ratio of the particle, λ is the viscosity ratio and Ca is capillary number. Here L_0, B_0 are semi-major and semi-minor axes of the undeformed capsule and μ, μ_0 are the inner and outer viscosities of the capsule. We vary Ca from 0.02 to 0.4, λ from unity to 25, and α between 0.6 and 0.9.

3.2 Capsule Dynamics at Low Shear

We begin with a detailed description of the capsule dynamics at ‘low shear’ at $Ca = 0.05$. Fig. 3.1 shows the time-dependent inclination angle $\theta(t)$, deformation parameter D , and semi-major (L) and semi-minor (B) axes. Here we describe the transition in the capsule dynamics that is observed in the simulations as the viscosity contrast λ is increased. We show the results for three viscosity contrasts, $\lambda = 3, 7$ and 10, all for aspect ratio $\alpha = 0.7$.

For $\lambda = 3$ case in Fig. 3.1(a), the numerical results show that the inclination angle $\theta(t)$ does not remain a constant, rather it oscillates with time. Here $\theta(t)$ is always positive ($0 < \theta(t) < \pi/2$) and it varies periodically between θ_{\max} and θ_{\min} . The capsule shape is also not stationary, and the angular oscillation is accompanied by a periodic shape deformation as evident from D , L , and B plots in Fig. 3.1(a). The lengths of the major and minor axes oscillate with a large

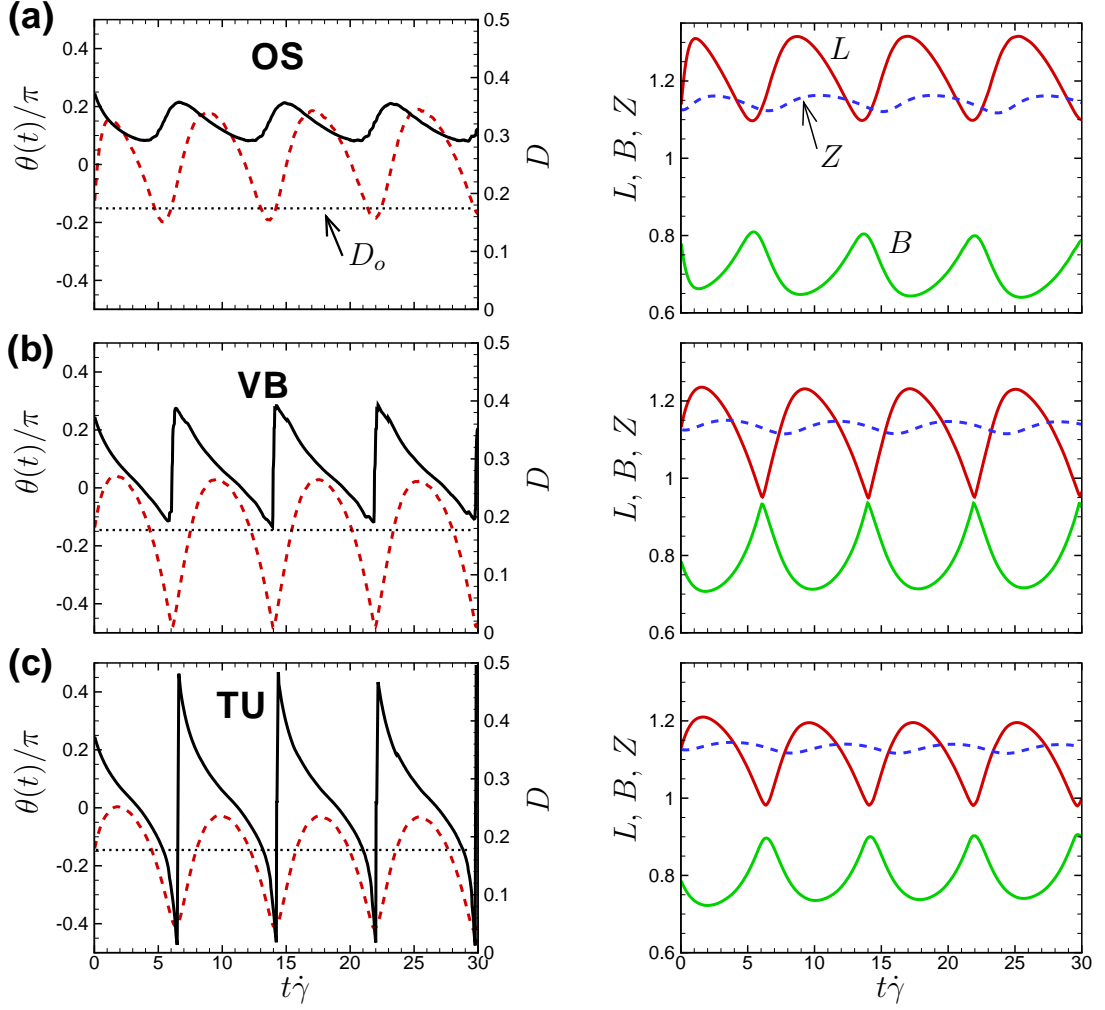


Figure 3.1: (Color online). Capsule dynamics at ‘low shear’ ($Ca = 0.05$) showing oscillatory (OS), vacillating-breathing (VB) and tumbling (TU) motions. Left panel shows the inclination angle $\theta(t)$ (solid black line) and the deformation parameter D (dash red line). The black dotted line is $D_o = D(t = 0)$. Right panel shows the semi-major (L , red solid line) and minor (B , green solid line) axes, and the half axis length in the vorticity direction (Z , dash blue line). All lengths are scaled by a , and time by $1/\dot{\gamma}$. Note that $(L - B)_{\min}$ and D_{\min} are nearly zero for the VB case shown in (b).

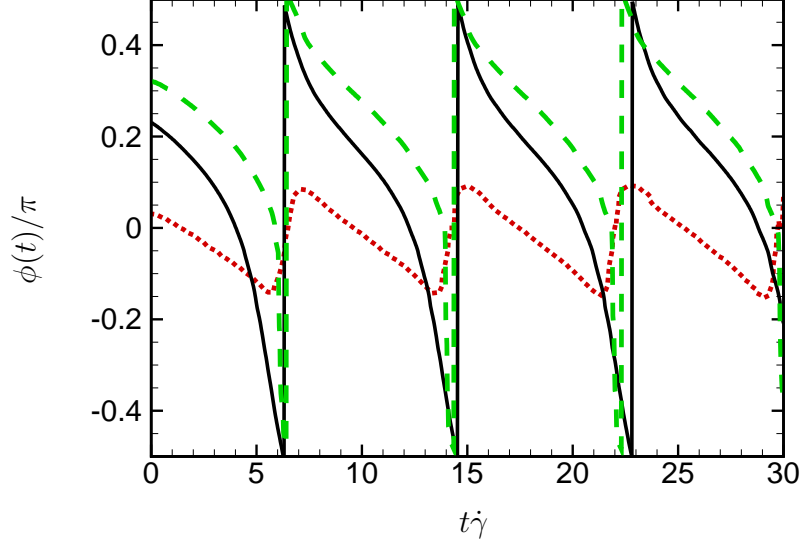


Figure 3.2: (Color online). Phase angle $\phi(t)$ for the three cases shown in Fig. 3.2. $\lambda = 3$, solid line; $\lambda = 7$, dash line; $\lambda = 10$, dotted line.

amplitude. The oscillatory (or, swinging) motion of the capsule is superimposed with a tank-treading motion of the membrane. The tank-treading motion is described in Fig. 3.2 where the of the undeformed capsule phase angle $\phi(t)$ of a surface Lagrangian point is shown. For $\lambda = 3$ case, $\phi(t)$ decreases smoothly from $\pi/2$ to $-\pi/2$ (and, $\dot{\phi} < 0$ in accordance with the direction of vorticity of the flow) implying the tank-treading motion of the capsule membrane.

Consider now $\lambda = 10$ case as shown in Fig. 3.1(c). A tumbling motion is observed here which is indicated by the inclination angle $\theta(t)$ going from $+\pi/2$ to $-\pi/2$. Even for this tumbling case, a significant shape deformation is evident as D , L and B oscillate with a large amplitude. The phase angle $\phi(t)$ oscillates between its maximum and minimum (Fig. 3.2) whose magnitude remains less

than $\pi/2$, and $\dot{\phi}$ is both positive and negative, implying that a Lagrangian point oscillates back and forth along the capsule surface, and that the tank-treading motion is inhibited.

Consider now an intermediate viscosity contrast at $\lambda = 7$ in Fig. 3.1(b). Here $\theta(t)$ periodically becomes positive and negative, but does not reach $\pm\pi/2$. Hence the capsule does not make a full tumbling. Instead, it makes large amplitude swinging motion about a mean inclination which is close to zero. A sharp increase in $\theta(t)$ occurs while going from θ_{\min} to θ_{\max} which is associated with a large amplitude shape oscillation as evident from D , L , and B plots in Fig. 3.1(b). From Fig. 3.2 we see that for this case the phase angle ϕ ranges in $\pm\pi/2$, and $\dot{\phi}$ is always negative, implying that the tank-treading motion still exists.

The numerical results presented above suggest that the capsule dynamics at the intermediate viscosity contrast ($\lambda = 7$ here) is distinct from the oscillatory motion at a lower λ and the tumbling motion at a higher λ . This can be further understood by comparing the amplitude of shape deformation for the three cases. The amplitudes of $D(t)$, $L(t)$, and $B(t)$ are higher at $\lambda = 7$ than those at $\lambda = 3$ and 10. Most interestingly, the minimums of $L - B$ and D , that is, $(L - B)_{\min}$ and D_{\min} , first decrease as λ is increased from 3 to 7, but then increase as λ is increased further to 10. At $\lambda = 7$, both $(L - B)_{\min}$ and D_{\min} are nearly zero meaning that the capsule momentarily attains a near-circular shape in the plane of shear. This happens when $\theta(t)$ becomes negative.

It is interesting to note that for $\lambda = 7$ the inclination angle $\theta(t)$ and the major

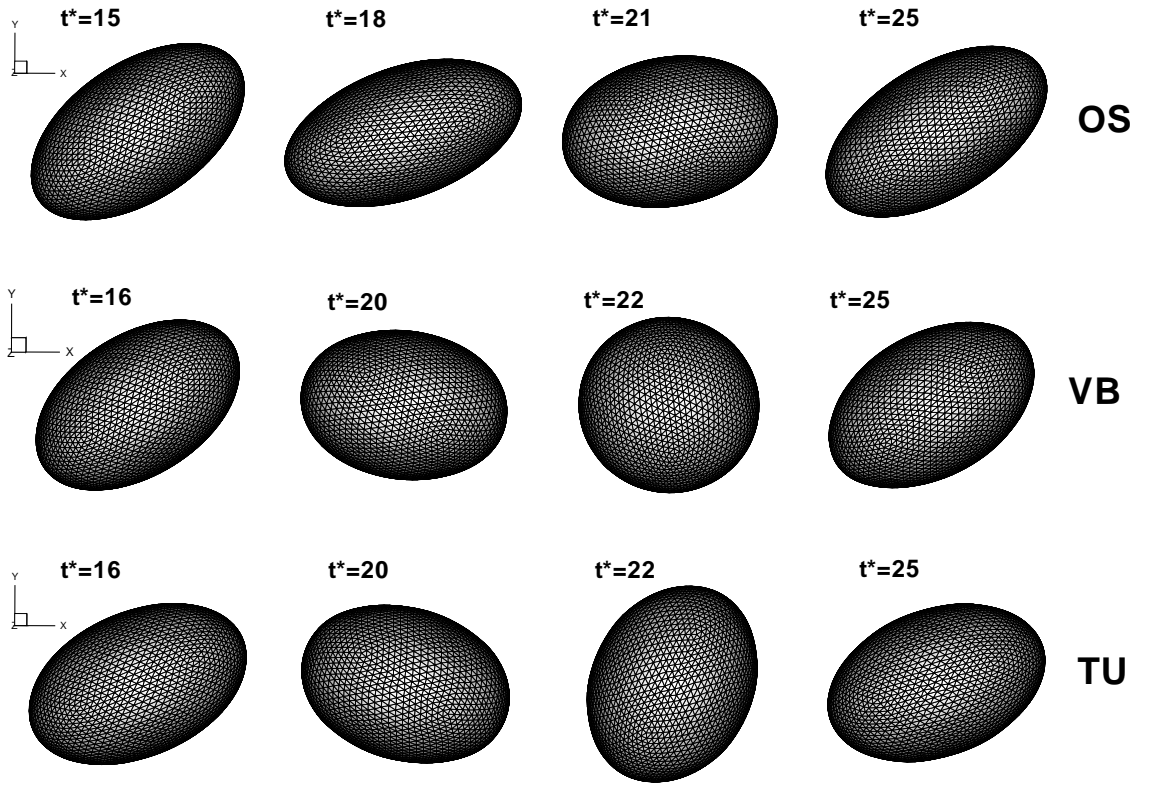


Figure 3.3: Instantaneous shapes for the oscillatory (OS), vacillating-breathing (VB) and tumbling (TU) motion at $Ca = 0.05$. For all cases, $\alpha = 0.7$. From top to bottom, λ varies as 3, 7, and 10 (compare with Fig. 3.1).

and minor axes presented here look qualitatively similar to those of a vacillating-breathing vesicle as predicted theoretically in [26] (see Figs. 3.2 and 3.3 therein) and observed experimentally in [10].

Fig. 3.3 shows the capsule shapes at different times for the three viscosity contrasts ($\lambda = 3, 7, 10$). Swinging or oscillatory motion for $\lambda = 3$, and tumbling motion for $\lambda = 10$ are evident here. For $\lambda = 7$ case, the shape becomes nearly circular in the shear plane during $\theta(t) < 0$, while it is elongated during $\theta(t) > 0$. This clearly shows that for the intermediate viscosity contrast, the capsule undergoes a significant elongation and compression. The shape at $\theta(t) < 0$ is not a mirror image of the shape at $\theta(t) > 0$. Further, a full tumbling motion does not occur though $\theta(t)$ becomes negative. A qualitative explanation of this dynamics was given in [14], and is applicable here as well. When $\theta(t) > 0$, the capsule is in its elongational state for which the hydrodynamic torque is maximum, and it tends to tumble. As $\theta(t)$ becomes negative, compression starts, and the hydrodynamic torque is reduced preventing the capsule from making a full tumbling motion. At even higher viscosity contrast (e.g., $\lambda = 10$ here), the compression is not significant, and a full tumbling is possible.

The numerical results presented in Figs. 3.1–3.3 describe the transition in the capsule dynamics at a low Ca as λ is increased. Three types of motion are evident here that can be characterized using $\theta(t)$ and $(L - B)_{\min}$. (i) At a low λ , a swinging or oscillatory (OS) motion occurs in which the major axis always lies in the extensional quadrant of the shear flow, with $0 < \theta(t) \leq \pi/4$, and

$(L - B)_{\min} > 0$. (ii) At higher λ , a pure tumbling motion (TU) occurs that is characterized by $\theta(t)$ varying between $\pm\pi/2$, and $(L - B)_{\min} > 0$. (iii) At the intermediate viscosity contrast, a vacillating-breathing (VB) type motion occurs which is characterized by an increased shape deformation, $(L - B)_{\min} \approx 0$, and $\theta(t)$ being periodically positive and negative without a full tumbling motion.

The above results on the capsule dynamics show two significant departures from the KS theory. First, the KS theory predicts either a steady inclination angle (at a low viscosity contrast), or a tumbling motion (at a higher viscosity contrast), unlike the OS and VB modes seen here. Second, and more interestingly, at the intermediate viscosity contrast, the inclination angle $\theta(t)$ periodically becomes positive and negative without a full tumbling, while in the KS theory the tumbling motion starts as soon as $\theta(t) < 0$.

The half axis length $Z(t)$ along the vorticity direction is also shown in Fig. 3.1. For all modes (OS, VB, TU), $Z(t)$ shows a small amplitude oscillation. For the OS case Z is mostly less than L . For the VB and TU modes, $Z(t)$ can be greater than $L(t)$, and the capsule momentarily attains a prolate shape whose major axis lies along the vorticity direction.

The deformation parameter D at $t = 0$, D_o is marked in Fig. 3.1. By comparing D_o with $D(t)$, we can infer if the capsule is in an elongational or compressional state. For the OS case at $\lambda = 3$ (Fig. 3.1(a)), $D(t)$ is mostly greater than D_o , implying that the capsule spends more time in an extensional state. For the VB

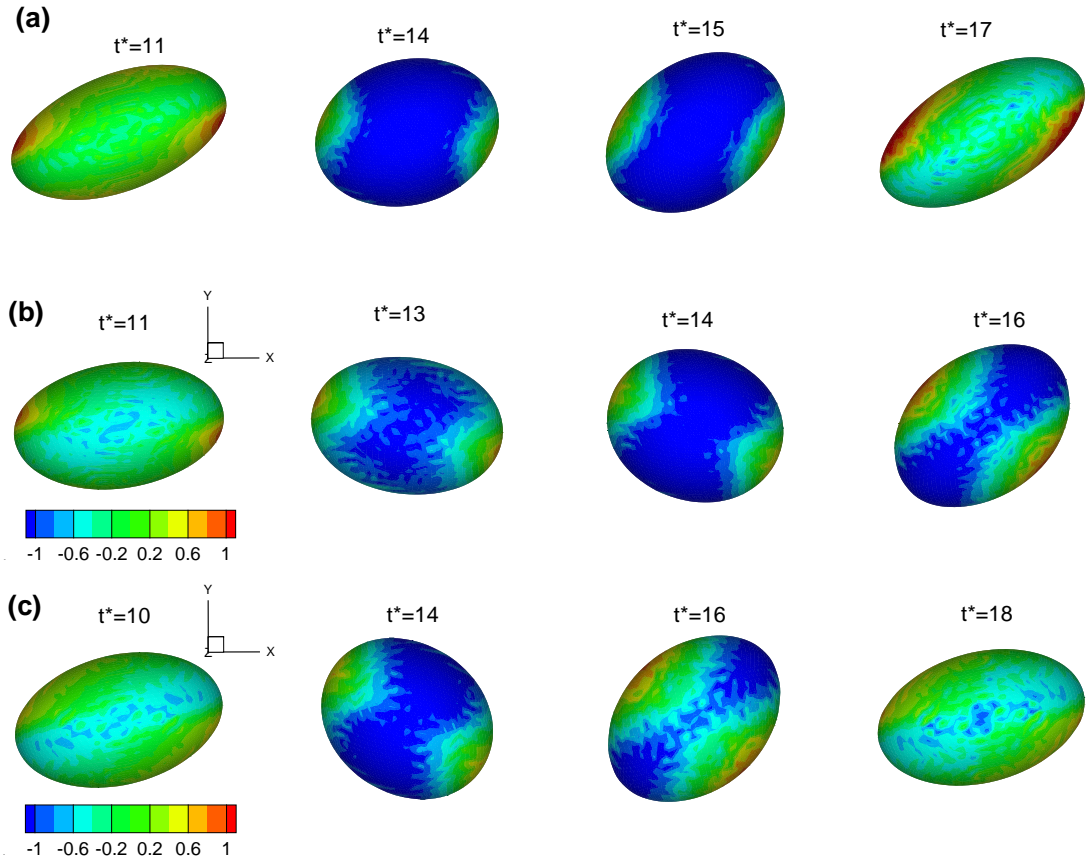


Figure 3.4: (Color online). Principal tension (in arbitrary unit) T_2^P for the (a) oscillatory (OS), (b) vacillating-breathing (VB), and (c) tumbling (TU) motion at $Ca = 0.05$. For all cases, $\alpha = 0.7$. From top to bottom, λ varies as 3, 7, and 10 (compare with Fig. 3.1).

($\lambda = 7$) and TU ($\lambda = 10$) modes, $D(t)$ is mostly less than D_o , and hence the capsule spends a significant time in the compressional state. To elucidate this point further, we plot in Fig. 3.4 the contours of a principal tension on the capsule membrane defined as $T_2^P = (\partial W / \partial \epsilon_2) / \epsilon_1$.

Since the area is not conserved, the membrane can be locally under elongation or compression, and accordingly, T_2^P is either positive or negative. Fig. 3.4 shows that T_2^P varies over the capsule surface and becomes periodically positive/negative as the capsule oscillates. When $D(t)$ is maximum, $T_2^P > 0$ over the most of the surface. When $D(t) < D_o$, a compressional stress develops over a large area around the equatorial region of the capsule. Surprisingly, the compressional stress exists even when the inclination angle $\theta(t)$ is positive. Thus the part of the capsule may be under compression even when its major axis is oriented along the extensional direction of the flow. For all modes (OS, VB, TU) the maximum magnitude of the compressive stress exceeds that of the extensional stress. We also see (not shown in the figure) that stress magnitude decreases with increasing λ . Further, for low Ca, the compressive stress leads to onset of buckling in which the capsule membrane folds. Since T_2^P goes periodically positive and negative, we observe that the capsule goes through repeated membrane folding and recovery stages when $D(t) < D_o$ and $D(t) > D_o$, respectively.

The angular orientation and shape deformation are strongly coupled to each other. This coupling has a major influence on the capsule dynamics during the transition from swinging to tumbling mode. We now explore the coupling between

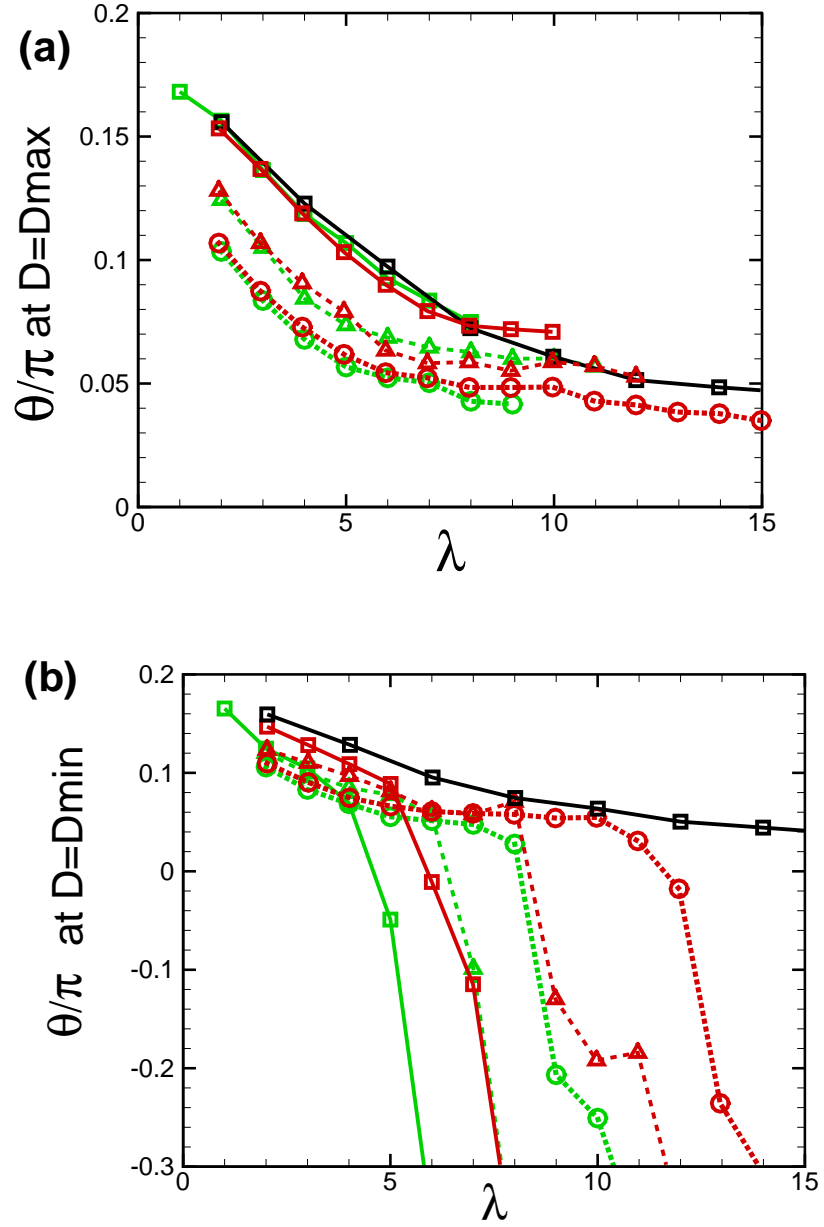


Figure 3.5: (Color online). (a) Inclination angle $\theta(t)$ at which D is maximum, and (b) $\theta(t)$ at which D is minimum, as a function of the viscosity contrast λ for different values of α and Ca . Here $\alpha = 0.6$ (green), 0.7 (red), and 0.9 (black). Symbols represent $Ca = 0.05$ (squares), 0.1 (delta), and 0.2 (circles).

the orientation dynamics and the shape deformation in more detail. Fig. 3.5(a) shows the inclination angle at which the maximum elongation occurs. We see that the angle at which the capsule elongation reaches its maximum is less than the extensional direction of the flow ($\pi/4$). This angle decreases with increasing Ca (and hence increasing shear). With respect to λ , the angle first decreases rapidly during the OS and VB modes, but becomes nearly independent of λ in the TU mode. Further, this angle is independent of α . At low Ca and low λ , the shape relaxation is fast compared to the flow time, and the elongation is in phase with the shear flow. At high Ca and high λ , the relaxation is slow, and the elongation continues for $\theta(t) < \pi/4$. Fig. 3.5(b) shows the inclination angle at which $D(t)$ reaches its minimum. In the OS mode, this angle is positive. With increasing λ the angle decreases rapidly as the transition to VB and TU modes occur. In the VB mode, minimum D occurs for $-\pi/4 < \theta < 0$. In the TU mode, the compression continues beyond $-\pi/4$ due to slower relaxation, and the minimum D occurs near $\theta = -\pi/2$.

We now show that the shape deformation is maximum for the intermediate λ values when the VB modes occur. For this, we consider the amplitude ΔD of the deformation parameter in Fig. 3.6(a). We also show the value of $(L-B)_{\min}$ in Fig. 3.6(b). Several interesting results are noted here which further elucidate the role of shape deformation on the emergence of the VB modes: (i) For a given Ca and α , the amplitude ΔD first increases but then decreases, and $(L-B)_{\min}$ first decreases to nearly zero but then slightly increases, with increasing λ . The maximum of

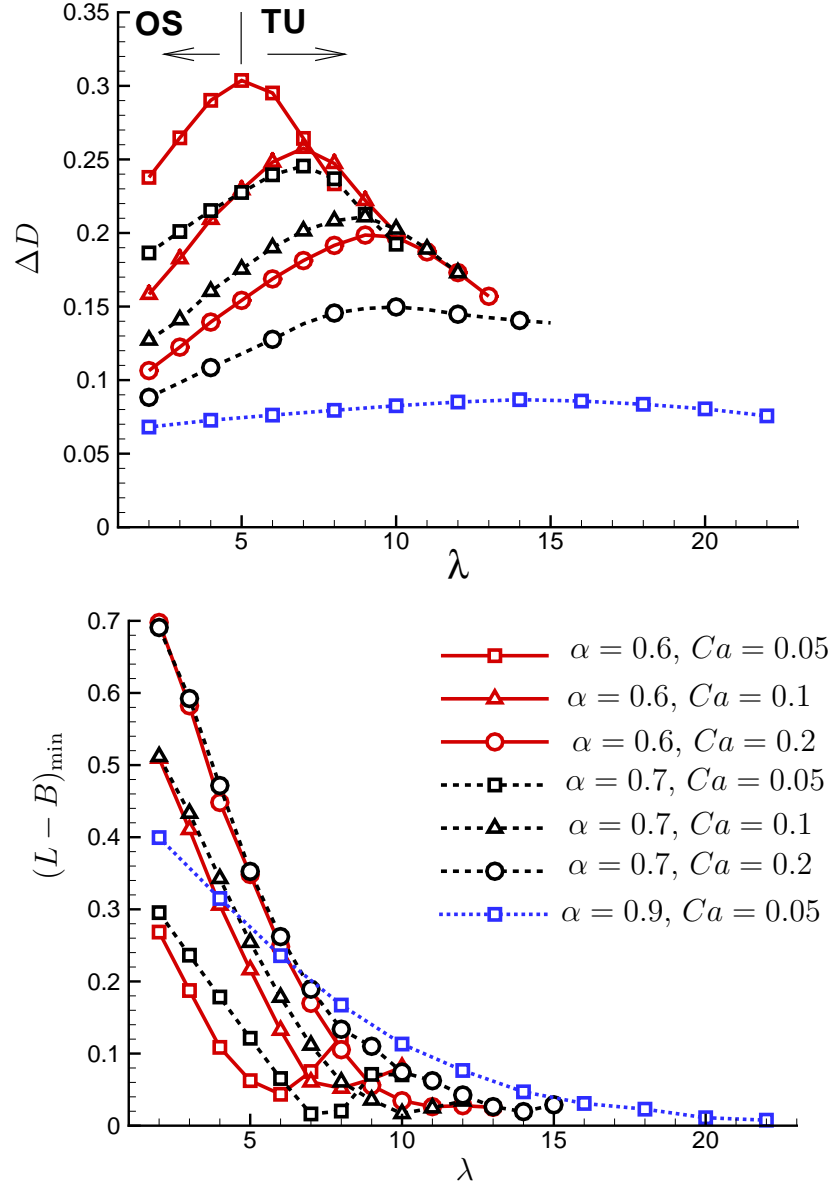


Figure 3.6: (Color online). Amplitude of shape deformation ΔD (top), and minimum of $(L - B)$ (bottom) as a function of the viscosity contrast λ for different values of α and Ca .

ΔD occurs at an intermediate λ for which the VB-type motion occurs so that the capsule momentarily attains a circular shape in the shear plane leading to $(L - B)_{\min} \approx 0$. (ii) ΔD and hence, shape oscillation, increases with decreasing Ca and α . (iii) The viscosity ratio at which ΔD reaches its maximum increases with increasing Ca and α , implying that the VB-type mode onsets at a lower λ for lower shear rates and α .

Now we present results showing the role of shape deformation in causing departures from the KS and SS models. The time average inclination angle θ_o is shown in Fig. 3.7(a)–(b), and compared with the KS theory. Both the numerical results and the KS theory show a decrease in θ_o with increasing λ . The agreement between the theory and the numerical results is better for weakly deformable capsules (low Ca), but poor for more deformable capsules (higher Ca). A significant difference between the theoretical and the numerical results occurs in the VB and TU modes, and hence, at higher λ . In the KS theory, the transition from the tank-treading to tumbling occurs when $\theta_o = 0$ via a saddle-node bifurcation; θ_o decreases faster as λ approaches λ_c . In contrast, the numerical results show a very slow decrease of θ_o near the transition. In the simulations, tumbling occurs even for $\theta_o > 0$. Such a slow decrease in θ_o has been reported earlier for vesicles with viscous membranes in [24] using stochastic simulations. Our results show that a qualitatively similar trend occurs for capsules as well, and can be predicted by deterministic simulations. This slow decrease in θ_o is due to a nonharmonic variation of θ w.r.t time arising from the large amplitude shape deformation, and

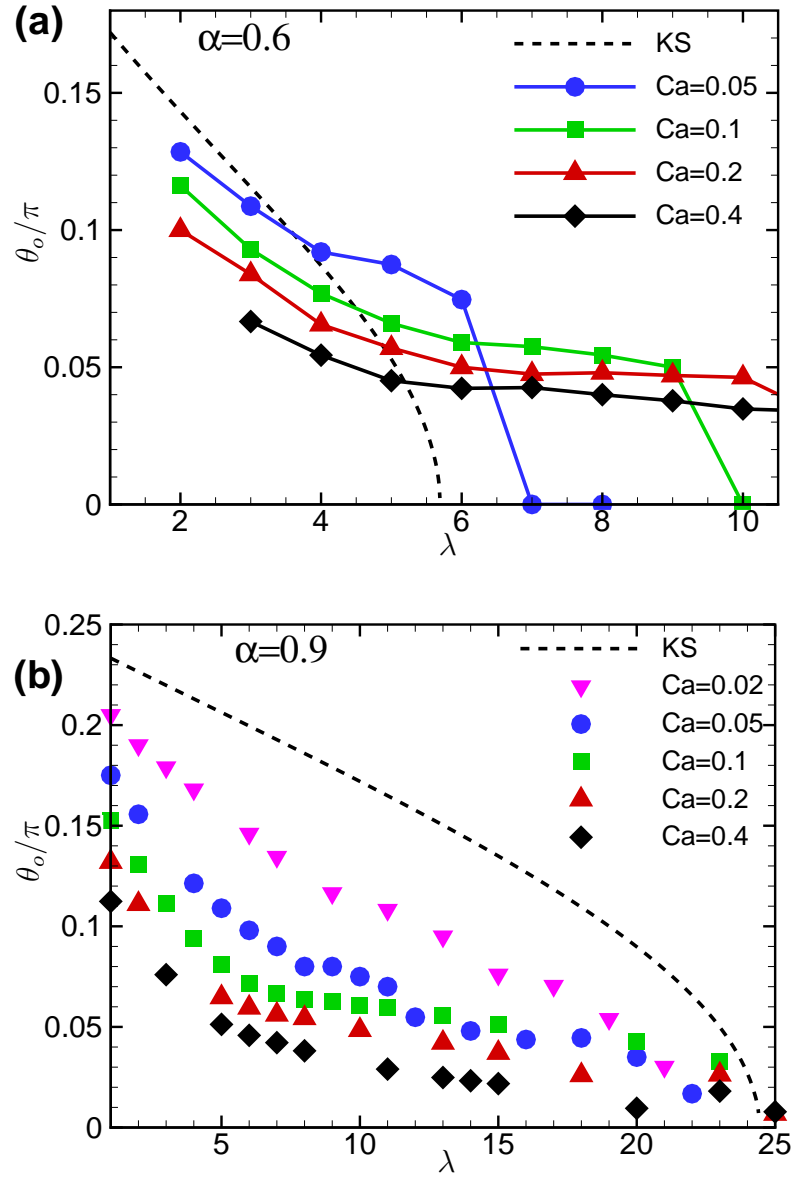


Figure 3.7: (Color online). Average inclination angle θ_o as a function of λ for (a) $\alpha = 0.6$, and (b) $\alpha = 0.9$. Symbols and/or solid lines are the numerical results. Dash line is the KS theory (KS).

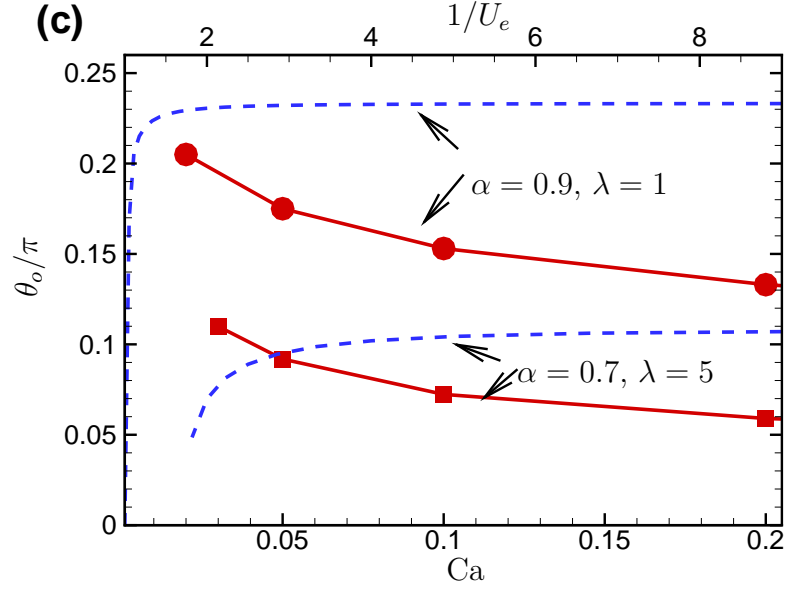


Figure 3.8: (Color online). Variation of θ_o with respect to Ca . Symbols and solid lines are the numerical results. Dash lines are based on the SS theory.

is discussed later.

Figure 3.8 shows the variation of θ_o with Ca , and compares the results with the SS theory in the OS regime. Note that in the SS theory, the effect of shear rate is considered via $1/U_e$ which is proportional to but not equal to Ca . Thus a qualitative comparison can be obtained between the theory and the numerical results by choosing a range of values of $1/U_e$. The numerical results show that in the OS regime, θ_o decreases with increasing Ca (or, $\dot{\gamma}$). In contrast, the SS theory predicts that θ_o is nearly insensitive to $\dot{\gamma}$ in the OS regime. This discrepancy is because the SS theory neglects the large deformation of capsules which is important at high $\dot{\gamma}$. More elongated shapes that occur at an increasing $\dot{\gamma}$ lead to a reduced θ_o . The decrease in θ_o with increasing Ca has been observed earlier in experiments [6] and numerical simulations [16,17] for spherical capsules, and is

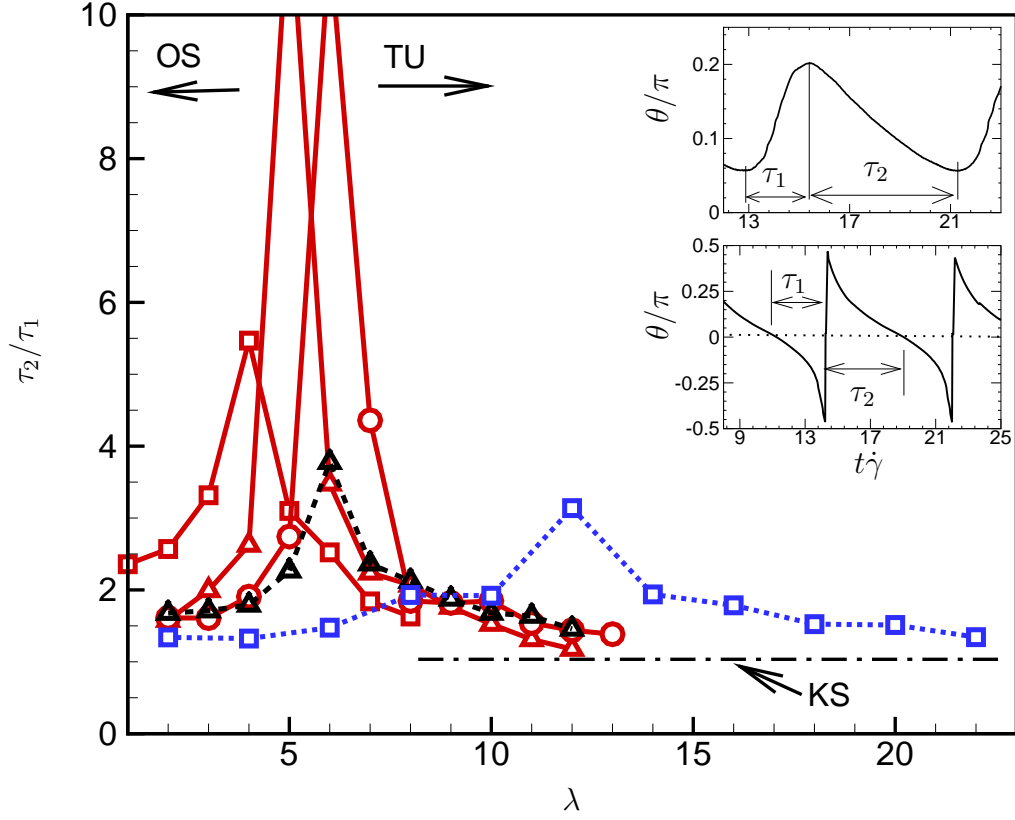


Figure 3.9: (Color online). Asymmetry in $\theta(t)$ shown by τ_2/τ_1 as a function of the viscosity contrast λ for different capillary numbers and aspect ratio. Various runs are as follows: $\text{---}\square\text{---}$ $\alpha = 0.6$, $Ca = 0.05$; $\text{---}\triangle\text{---}$ $\alpha = 0.6$, $Ca = 0.1$; $\text{---}\circ\text{---}$ $\alpha = 0.6$, $Ca = 0.2$; $\text{---}\triangle\text{---}$ $\alpha = 0.7$, $Ca = 0.1$; $\text{---}\square\text{---}$ $\alpha = 0.9$, $Ca = 0.05$. Inset shows how τ_1 and τ_2 are obtained from $\theta(t)$ for the OS and TU cases. KS: the Keller-Skalak theory.

in qualitative agreement with the present results for non-spherical capsules.

One important effect of the shape deformation on the orientation dynamics is a nonharmonic variation of the inclination angle $\theta(t)$ with time which results in an ‘asymmetry’ about its time-average value θ_o . The ‘asymmetry’ in $\theta(t)$, in turn, leads to non-zero values of θ_o , even in the TU regime (Figs. 3.7(a)–(b)), thus departing from the KS theory. We now quantify the ‘asymmetry’ in $\theta(t)$ as

follows. For an OS mode, $\theta(t)$ is always positive, and the ‘asymmetry’ in $\theta(t)$ can be defined by the ratio τ_2/τ_1 where τ_1 is the time taken by the capsule to go from θ_{\min} to θ_{\max} , and τ_2 is the time to go from θ_{\max} to θ_{\min} . In absence of an asymmetry, the ratio τ_2/τ_1 would be unity. The numerical results for τ_2/τ_1 is shown in Fig. 3.9 as a function of the viscosity contrast λ . In the OS regime, the numerical results show that $\tau_2/\tau_1 > 1$. This apparently implies that the capsule swings faster in direction opposite to the rotational motion of the flow. This is because the compression occurs over a longer time, while the elongation occurs much rapidly (Fig. 3.1). As λ increases, the ratio τ_2/τ_1 increases. It then approaches to ∞ as the VB-mode onsets at higher λ . In the VB and TU regimes, $\theta(t)$ becomes negative. Then τ_1 and τ_2 are computed as the times for which $\theta(t)$ is negative and positive, respectively (see inset of Fig. 3.9). The numerical results show that as the capsule transits from VB to TU-type motion with increasing λ , the ratio τ_2/τ_1 decreases from large values and approaches unity at higher λ . The KS theory predicts τ_2/τ_1 is always unity for a tumbling capsule. The numerical results show that τ_2/τ_1 can be greater than unity in the TU regime. This implies that the capsule spends more time in the extensional quadrant of the shear flow (though the capsule actually may be under compression even in this orientation, Fig. 3.4).

Another example of the coupling between the shape deformation and orientation dynamics is shown by the amplitude $\Delta\theta$ of the inclination angle as in Fig. 3.10. The numerical results are compared with the SS theory. Fig. 3.10(a) shows

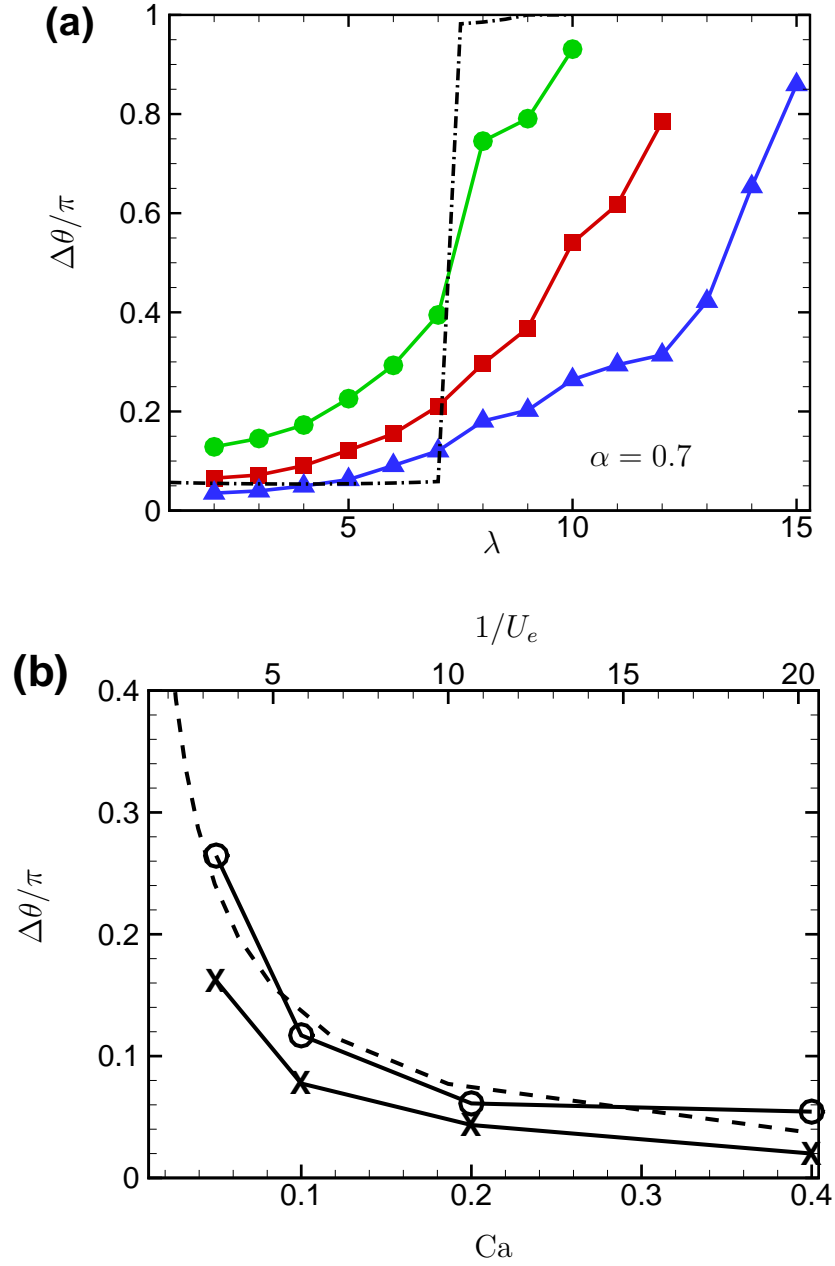


Figure 3.10: (Color online). Amplitude of oscillation of the inclination angle w.r.t. (a) λ , and (b) Ca . In (a), numerical results are shown by symbols and solid lines (green circle $Ca = 0.05$, red square $Ca = 0.1$, blue triangle $Ca = 0.2$). The dash-dot line is the result of the SS model for $1/U_e = 5$. All results are for $\alpha = 0.7$. In (b) the numerical results are for $\lambda = 4$ (circle) and $\lambda = 2$ (X). The dash line is the result for the SS model at $\lambda = 4$. All results are for $\alpha = 0.6$.

the variation of $\Delta\theta$ with respect to the viscosity contrast λ for a given Ca . As λ increases, $\Delta\theta/\pi$ increases from small values in the OS regime and approaches unity in the TU regime. In this respect, a qualitative agreement between the numerical results and the SS theory is observed. However, the SS theory predicts a sharp jump in $\Delta\theta$ near $\lambda = \lambda_c$, while the numerical results show a much slower increase. The slower increase of $\Delta\theta$ is due to the emergence the VB modes for which large-amplitude shape deformation occurs which is not considered in the SS model.

Figure 3.10(b) shows the variation of $\Delta\theta$ with respect to Ca for a given λ . Here we have chosen the data in the OS regime for clarity. The prediction based on the SS theory is also shown by choosing a range of $1/U_e$ for which the numerical data closely follows the theoretical prediction. Similar to the SS theory, the numerical $\Delta\theta$ decreases with increasing Ca (and so $\dot{\gamma}$). So the SS theory can capture the qualitative trend of $\Delta\theta$ with respect to $\dot{\gamma}$, but not with λ .

Figure 3.11(a) shows the variation of the lengths of the semi-major and minor axes w.r.t the inclination angle θ for OS, VB and TU cases. A large variation in the axis lengths is evident here. For all cases, the major axis shows a greater change in its length than the minor axis, that is, $|L_{\max} - L_{\min}| > |B_{\max} - B_{\min}|$. For the OS case, we see that there is a small asymmetry in L and B about the mean inclination angle θ_o . Elongation of the major axis (i.e. when L is increasing) occurs over a smaller variation of θ than its contraction. Similarly, the contraction of the minor axis occurs over a smaller variation of θ than its

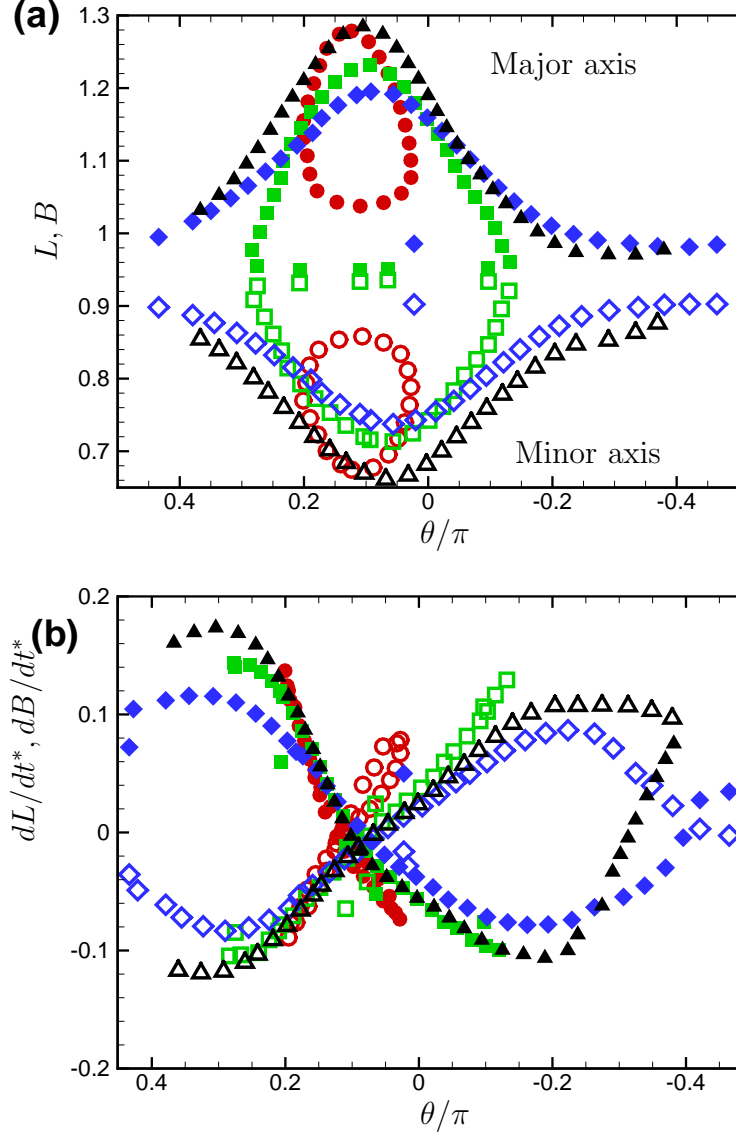


Figure 3.11: (Color online). (a) Variation of the semi-major (L , filled symbols) and minor (B , open symbols) axes w.r.t the inclination angle θ . Symbols are as follows. OS case: red circles ($\alpha = 0.7$, $\text{Ca} = 0.05$, $\lambda = 4$). VB case: green squares ($\alpha = 0.7$, $\text{Ca} = 0.05$, $\lambda = 7$). TU cases: blue diamond ($\alpha = 0.7$, $\text{Ca} = 0.05$, $\lambda = 10$), and black delta ($\alpha = 0.6$, $\text{Ca} = 0.05$, $\lambda = 7$). (b) dL/dt^* (filled symbols) and dB/dt^* (open symbols) for the similar cases as in (a).

elongation. This asymmetry implies that the capsule shape at $\theta(t) > \theta_o$ is not a mirror image of that at $\theta(t) < \theta_o$. The asymmetry increases further in the VB mode. When the TU mode is considered for which $\theta_o \approx 0$, we see that L and B are still asymmetric about $\theta_o = 0$. The major axis starts to grow, and the minor axis starts to contract, when $\theta = \theta_{\max}$ (OS and VB modes), or $\pi/2$ (TU modes). Elongation of the capsule continues for $\theta < \pi/4$. Contraction of the major axis, and elongation of the minor axis, start even for $\theta > 0$, when the capsule is oriented in the extensional quadrant of the flow.

Figure 3.11(b) shows the rates of elongation and contraction, dL/dt and dB/dt , over θ . For all modes (OS, VB, TU), the elongation and contraction rates show asymmetry, that is, they are higher when θ is positive than that when it is negative. Note that the overall deformation is described by the Taylor parameter D . The results imply that dD/dt is higher when the capsule is aligned with the compressional direction of the shear flow. Thus the elongation of the capsule from a compressional state occurs faster than the other way.

Figure 3.12 shows the variation of the angular velocity $\dot{\theta}$ with respect to θ . Results for the OS and TU regimes are shown in Fig. 3.12 and Fig. 3.13, respectively. In Fig. 3.12 we compare the numerical results ($\dot{\theta}_{\text{num}}$) with the SS theory ($\dot{\theta}_{\text{ss}}$) by choosing a value of $1/U_e$ (but for same λ and α) for which the best agreement is found.

The horizontal axis in the plot is $(\theta(t) - \theta_{\min})/(\theta_{\max} - \theta_{\min})$. In this regime, $\dot{\theta}$ becomes positive and negative due to capsule oscillation. However, $|\dot{\theta}_{\text{num}}|$ is

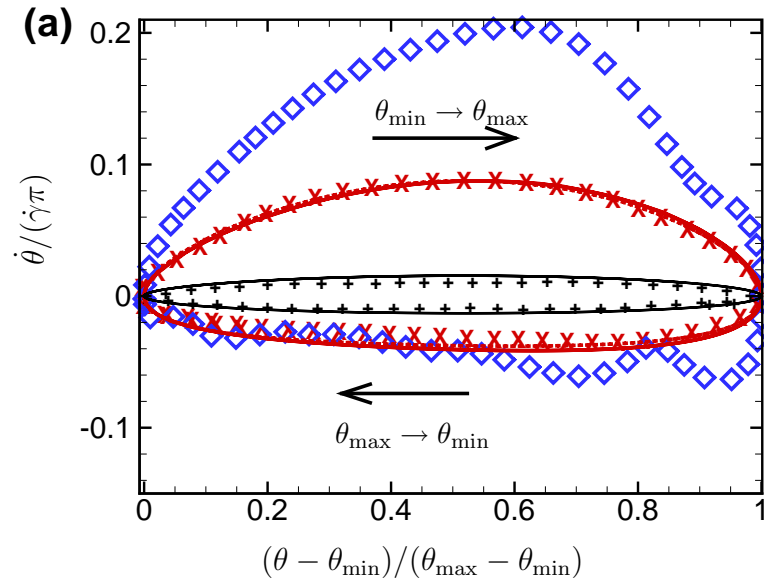


Figure 3.12: (Color online). Angular velocity $\dot{\theta}$. Results for OS cases: right and left arrows imply θ going from θ_{\min} to θ_{\max} , and θ_{\max} to θ_{\min} , for which $\dot{\theta}$ is positive and negative, respectively. Symbols are numerical results for $\alpha = 0.7$ for $\text{Ca} = 0.05, \lambda = 3$ (red X), $\text{Ca} = 0.05, \lambda = 5$ (blue \diamond), $\text{Ca} = 0.2, \lambda = 3$ (black +). Lines are the SS theory for $1/U_e = 2, \lambda = 3$ (solid red line), $1/U_e = 2, \lambda = 5$ (dash red line), $1/U_e = 8, \lambda = 3$ (solid black line). First two SS cases (solid red line and dash red line) nearly overlap in the figure.

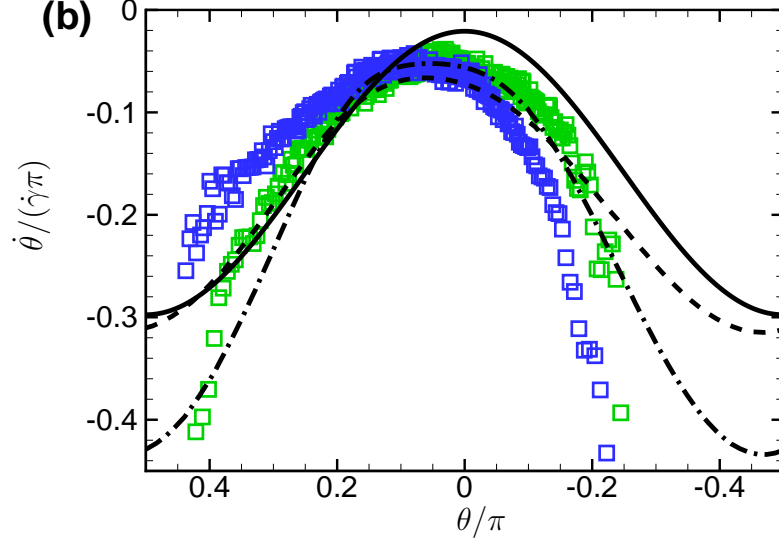


Figure 3.13: (Color online). Angular velocity $\dot{\theta}$. Results for TU cases: Symbols are numerical results for $\alpha = 0.7$ for $\text{Ca} = 0.05$, $\lambda = 10$ (green squares), and $\text{Ca} = 0.02$, $\lambda = 5$ (blue squares). Solid black line is the KS theory for $\alpha = 0.7$, $\lambda = 10$. Dash and dash-dot black lines are the SS theory for $\alpha = 0.7$ for $1/U_e = 1$, $\lambda = 10$, and $1/U_e = 1.43$, $\lambda = 5$, respectively.

lower when the capsule swings clockwise in the direction of rotation of the flow (i.e, when θ goes from θ_{\max} to θ_{\min}) than that when it goes the other way. This asymmetry is the result of the shape deformation in which elongation occurs faster and over a smaller extent of $\theta(t)$ as discussed before. The magnitude of $\dot{\theta}_{\text{num}}$ in the counter-clockwise swing increases rapidly with increasing λ , while that in the clockwise swing increases at a slower rate. The asymmetry also increases with decreasing Ca .

The numerical results can be matched with the SS theory by choosing an appropriate value of $1/U_e$. We also noted that the effect of changing Ca can also be matched when we proportionately change U_e , as shown in the figure. However,

the effect of changing λ is not predicted correctly by the SS theory which shows that $\dot{\theta}_{\text{SS}}$ is nearly insensitive to changing λ .

Figure 3.13 shows $\dot{\theta}$ for the TU cases, and compares the numerical results with the KS and SS theory. Unlike the KS theory for which $\dot{\theta}_{\text{KS}}$ is symmetric about $\theta = 0$, the numerical results show a significant asymmetry. Further, $|\dot{\theta}_{\text{num}}| > |\dot{\theta}_{\text{KS}}|$ for $\theta < 0$, but $|\dot{\theta}_{\text{num}}| < |\dot{\theta}_{\text{KS}}|$ for $\theta > 0$. Hence the numerical tumbling velocity is lower than that predicted by the KS theory when the capsule is in the extensional quadrant of the shear flow. This is because the capsule spends more time in the extensional quadrant as shown earlier ($\tau_2/\tau_1 > 1$). When the capsule is in the compressional quadrant, the numerical tumbling velocity is higher than that predicted by the KS theory because the capsule spends less time here. When we compare the numerical results with the SS theory, we see that the SS theory can capture the asymmetrical nature of $\dot{\theta}_{\text{num}}$ to some extent, but it still differs from the numerical results.

3.3 Capsule Dynamics at High Shear

We now consider the capsule dynamics at ‘high shear’ ($\text{Ca} \geq 0.2$, typically) as shown in Fig. 3.14. Here we show time dependent inclination angle $\theta(t)$, deformation parameter $D(t)$, and the length of the semi-major and minor axes, $L(t)$ and $B(t)$. These simulations are performed for longer times ($t^* > 50$). Very interestingly, we see that the same capsule transits from one mode to other over time. For example, in Fig. 3.14(a) which is for $\text{Ca} = 0.2$ and $\lambda = 13$, we see

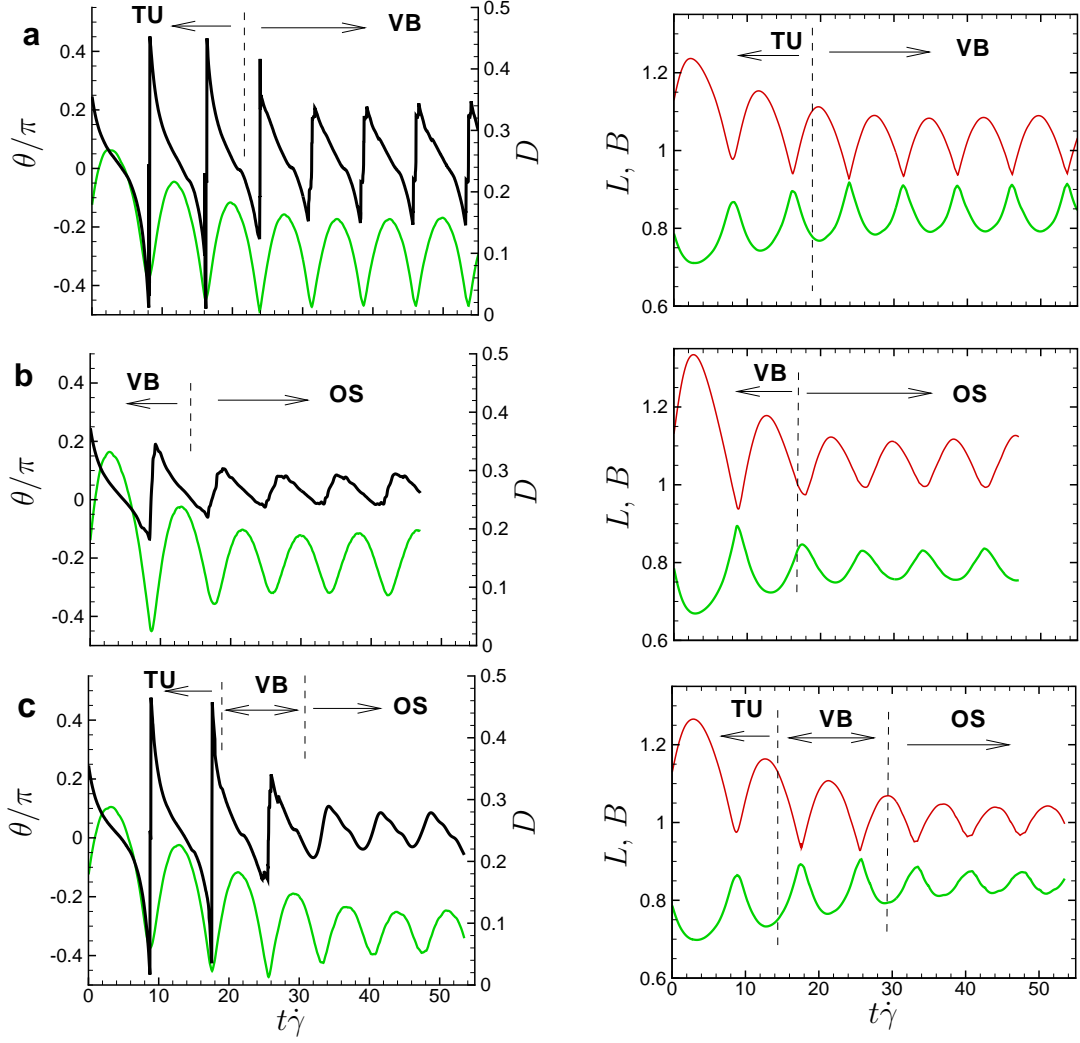


Figure 3.14: (Color online). Capsule dynamics at ‘high shear’ for $\alpha = 0.7$. (a) $Ca = 0.2, \lambda = 13$; (b) $Ca = 0.4, \lambda = 9$; (c) $Ca = 0.4, \lambda = 13$. Left panel shows the inclination angle $\theta(t)$ (black line), and deformation parameter D (green line). Right panel shows semi-major and minor axes lengths, L (red line) and B (green line).

that the capsule switches from TU to VB mode at around $t^* \approx 25$, after making one full tumbling motion. In Fig. 3.14(b) which is for $\text{Ca} = 0.4$ and $\lambda = 9$, the capsule switches from VB to OS mode at around $t^* \approx 15$. In Fig. 3.14(c) which is for $\text{Ca} = 0.4$ and $\lambda = 13$, we see that two transitions occur: from TU to VB at $t^* \approx 20$, and VB to OS at $t^* \approx 30$. We conducted a large number of simulations going up to $\lambda = 25$. Based on all simulations, we observe three types of transient states which occur with increasing viscosity contrast as $\text{VB} \rightarrow \text{OS}$, $\text{TU} \rightarrow \text{VB} \rightarrow \text{OS}$, and $\text{TU} \rightarrow \text{VB}$. The transition is always one-way; a transition in the reverse direction is not observed.

In agreement with the results in [19], therefore, we do not observe any intermittent dynamics as theoretically predicted by the SS model [12].

Based on our simulation results, we present phase diagrams on λ — Ca plane identifying different dynamical regimes in Fig. 3.15. At a low Ca , three regimes are observed, namely OS, VB, and TU, with increasing λ . The VB mode occurs in the neighborhood of $\lambda = \lambda_c$ immediately before transition from the OS to TU modes. Our results show that the VB mode exists over a large range of the viscosity contrast. The critical viscosity contrasts at which $\text{OS} \rightarrow \text{VB}$ and $\text{VB} \rightarrow \text{TU}$ transitions occur increase with increasing Ca and α . The phase diagrams show that the transitions can be triggered below λ_c by decreasing Ca . This behavior is in qualitative agreement with the SS theory, and the experiments of Abkarian *et al.* [5] using erythrocytes in shear flow. At higher Ca , the three transient regimes, $\text{VB} \rightarrow \text{OS}$, $\text{TU} \rightarrow \text{VB} \rightarrow \text{OS}$, and $\text{TU} \rightarrow \text{VB}$, exist

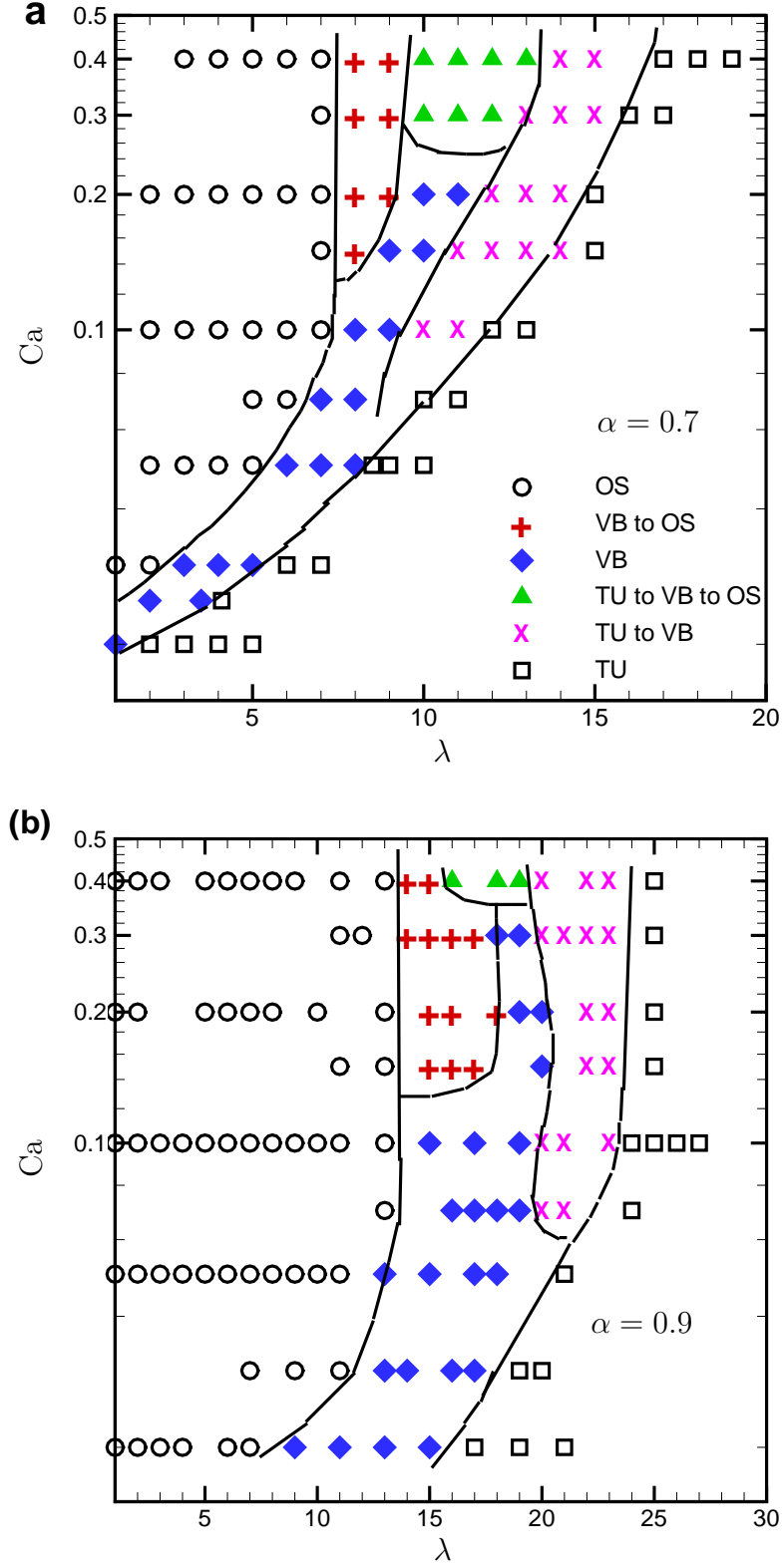


Figure 3.15: (Color online). Phase diagrams showing different regimes of capsule dynamics for (a) $\alpha = 0.7$, and (b) 0.9.

in the region between the OS and TU modes. The range of λ over which these transient modes occur increases with increasing Ca. Hence, these transient modes would be important for capsule dynamics at high shear.

Chapter 4

Rheology of a Dilute Suspension of Liquid-filled Elastic Capsules

4.1 Introduction

Understanding rheology of blood is a fundamental problem of immense biological importance, and has been a subject of *in vivo* and *in vitro* studies over nearly a century. These studies have addressed blood rheology on a macroscale, and demonstrated several non-Newtonian behaviors, such as, the shear-thinning viscosity and the Fahraeus-Lindqvist effect. In contrast, there has been relatively fewer studies which seek to connect the macroscopic rheology with the microhydrodynamics of individual erythrocytes.

Following Batchelor's theory of suspension [43], Barthes-Biesel & Chhim [44] derived expressions of shear viscosity and normal stress differences of a dilute suspension of spherical capsules undergoing small deformation. The salient features of their result are: (i) the suspension exhibits shear-thinning behavior with shear viscosity $\mu_s \propto \lambda \dot{\gamma}$, where $\dot{\gamma}$ is the shear rate; (ii) normal stress differences, to the leading order, depend linearly on $\dot{\gamma}$ but independent of λ . Using boundary integral simulations, Pozrikidis [45] and Ramanujan & Pozrikidis [16] computed

dilute suspension rheology for spherical capsules undergoing large deformation. Pozrikidis [46] also briefly addressed time-dependent rheology of a dilute suspension of biconcave capsules.

For a dilute suspension of vesicles, a remarkable result is recently discovered by Misbah and co-workers [14, 47, 48]. In the limit of small vesicle excess area, they theoretically predict that the shear viscosity of the vesicle suspension first decreases reaching a minimum, and then increases with increasing λ . Thus the shear viscosity is higher when the vesicle is either in a pure tank-treading motion, or in a pure tumbling motion. The pronounced minimum of the shear viscosity occurs in the vicinity of the critical viscosity contrast λ_c , and, hence, it is associated with the onset of the vacillating-breathing motion as the vesicle makes transition between the tank-treading and tumbling motions. Their theoretical result is later supported by viscometric experiments using erythrocyte and vesicle suspensions [49].

In this chapter, we address the rheology of a dilute suspension of capsules. We focus exclusively on initially *spherical* capsules for which only a steady tank-treading motion is observed. Using three-dimensional numerical simulations of capsules in large deformation, we present a very comprehensive analysis of the suspension rheology over a broad range of viscosity contrast and shear rate for both strain-hardening and strain-softening membrane. We also investigate (i) whether the shear viscosity anomaly (i.e. shear viscosity minimum at moderate values of viscosity ratio, and at high shear rates) exists for capsule suspensions,

similar to that found for a vesicle suspension [14, 47–49].

(ii) whether the anomaly is a result of the onset of the vacillating-breathing mode, or it can occur even when the capsule is undergoing a steady tank-treading motion, and,

(iii) how the viscosity difference between the interior and exterior fluids, and the elastic stresses on the capsule membrane individually contribute to the bulk rheology.

We observe that a capsule suspension exhibits a shear viscosity minimum even when the capsule makes a steady tank-treading motion. We then show that the viscosity minimum is a result of non-trivial contributions coming from the capsule membrane stresses and the viscosity difference between the interior and suspending fluids.

4.2 Methodology

Three-dimensional numerical simulations using front-tracking methods are performed to simulate capsule dynamics and rheology. We consider an initially spherical capsule of radius a suspended in a linear shear flow $\mathbf{u}^\infty = \{\dot{\gamma}y, 0, 0\}$. The constitutive law describing the membrane material of the capsule is described in terms of a strain energy function W . We consider both strain-hardening and strain-softening membranes. For the former, we use the strain energy function

developed by Skalak et al [34] (hereafter referred to as SK model):

$$W = \frac{E_s}{8} [(\epsilon_1^2 + \epsilon_2^2 - 2)^2 + 2(\epsilon_1^2 + \epsilon_2^2 - \epsilon_1^2 \epsilon_2^2 - 1)] + \frac{E_a}{8} (\epsilon_1^2 \epsilon_2^2 - 1)^2 \quad (4.1)$$

where ϵ_1 and ϵ_2 are the principal stretch ratios, and E_s and E_a are the moduli of shear elasticity, and area dilatation, respectively. For a strain-softening membrane, we use the neo-Hookean law (hereafter referred to as NH model):

$$W = \frac{E_s}{6} (\epsilon_1^2 + \epsilon_2^2 + \epsilon_1^{-2} \epsilon_2^{-2} - 3) \quad (4.2)$$

We scale all lengths by a , and time by $1/\dot{\gamma}$. The three major dimensionless parameters are capillary number $\text{Ca} = \mu_o a \dot{\gamma} / E_s$, the viscosity ratio λ , and the ratio of area-dilatation to shear deformation moduli $C = E_a / E_s$.

Following Batchelor, the bulk stress of a dilute suspension can be written as

$$\Sigma^{\text{bulk}} = \Sigma^\infty + \Sigma \quad (4.3)$$

where $\Sigma^\infty = 2\mu_o \mathbf{E}$ is the contribution due to the imposed linear flow \mathbf{u}^∞ , \mathbf{E} is the strain-rate tensor, and Σ is the particle stress tensor that accounts for the contribution from the capsules [43]. For M number of identical capsules in a volume of V , the particle stress tensor is given by

$$\Sigma_{ij} = \frac{1}{V} \sum_M \int_A [\sigma_{ik} n_k x'_j - \mu_o (u_i n_j + u_j n_i)] dA \quad (4.4)$$

where σ is the stress in the suspending fluid at the capsule membrane, \mathbf{n} is the unit vector normal to the capsule surface and directing outward, \mathbf{x}' and \mathbf{u} are the position and velocity on a capsule surface, and the integral is taken over the surface A . In the front-tracking method, we find it convenient to use an alternative expression

$$\Sigma_{ij} = \frac{1}{V} \sum_M \int_A [f_i x'_j + \mu_o (\lambda - 1) (u_i n_j + u_j n_i)] dA \quad (4.5)$$

where \mathbf{f} is the elastic force in the membrane [16, 45].

It is of interest to study the individual contributions of the membrane stress and viscosity difference to the particle stress. Hence we introduce the *elastic* and *viscous* contributions as

$$\Sigma_{ij}^{\text{el}} = \frac{1}{V} \sum_M \int_A f_i x'_j dA, \quad (4.6)$$

and

$$\Sigma_{ij}^{\text{vis}} = \frac{\mu_o (\lambda - 1)}{V} \sum_M \int_A (u_i n_j + u_j n_i) dA, \quad (4.7)$$

respectively, so that,

$$\Sigma_{ij} = \Sigma_{ij}^{\text{el}} + \Sigma_{ij}^{\text{vis}}. \quad (4.8)$$

The elastic contribution Σ^{el} arises due to the stresses developed in the capsule

membrane, while the viscous contribution Σ^{vis} arises due to the viscosity difference between the internal and suspending fluids.

Quantities of interest are the particle shear stress Σ_{xy} , the first normal stress difference $N_1 = \Sigma_{xx} - \Sigma_{yy}$, and the second normal stress difference $N_2 = \Sigma_{yy} - \Sigma_{zz}$.

The shear viscosity is given by

$$\mu_{\text{eff}} = \mu_o \left(1 + \frac{\Sigma_{xy}}{\mu_o \dot{\gamma}} \right) \quad (4.9)$$

In the following sections, the particle stresses are presented by scaling them by $\mu_o \dot{\gamma} \phi$ where ϕ is the capsule volume fraction. For the present simulations, $\phi = 0.017$.

4.3 Results

4.3.1 Capsule shape and orientation

We consider capsules of spherical resting shape for which only the *steady tank-treading* motion is observed. When placed in a shear flow, the capsule deforms and eventually attains a steady oblate shape, and aligns at a steady inclination angle with the flow direction. Figs. 4.1a and 4.1b show the final capsule shape for $\lambda = 1$ and 13, both at $\text{Ca} = 0.6$, for capsules with SK model ($C = 1$). Large deformation resulting to an elongated shape is observed at $\lambda = 1$, whereas less deformed shape is observed at $\lambda = 13$. Fig. 4.1c shows the evolution of the Taylor

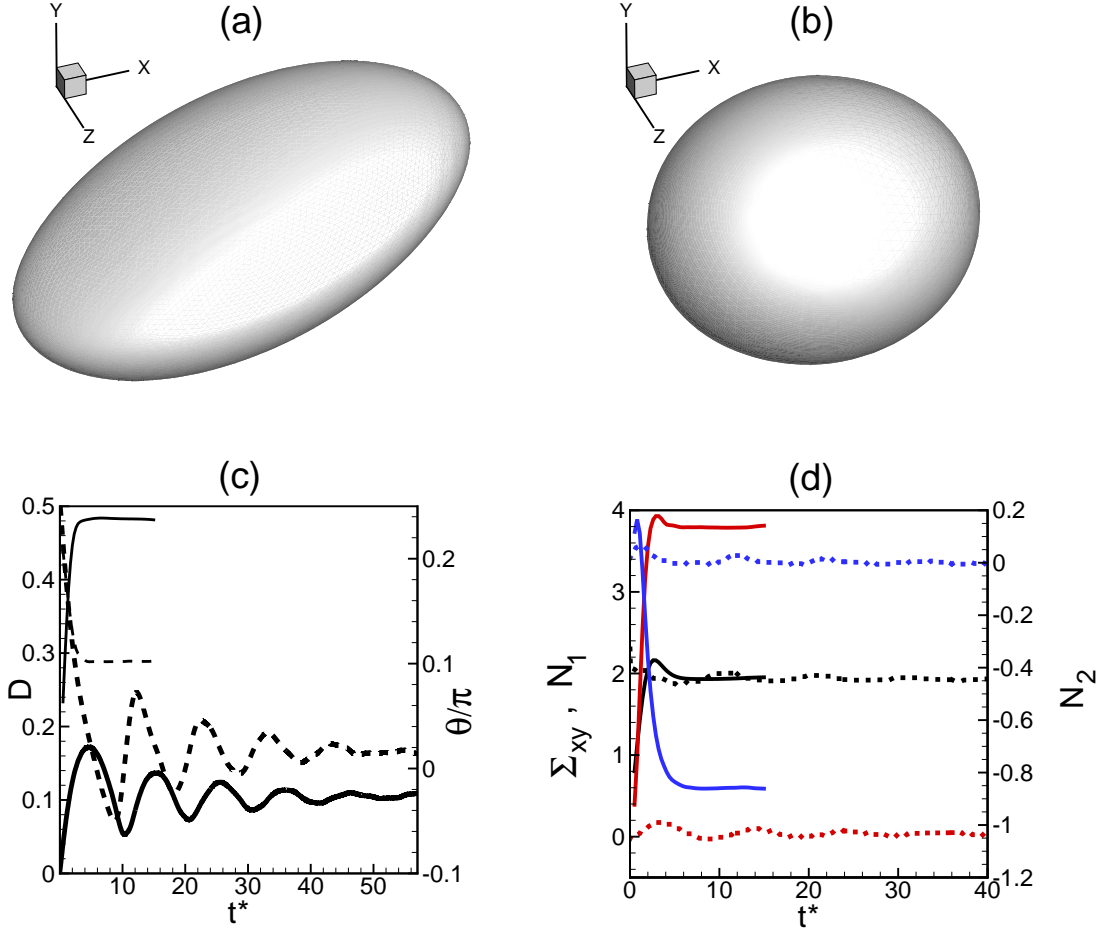


Figure 4.1: (Color online) Sample results for spherical capsules with SK model ($C = 1$). (a) and (b) show the final shapes for $\text{Ca} = 0.6$, $\lambda = 1$ and $\text{Ca} = 0.6$, $\lambda = 13$, respectively. (c) Time-dependent Taylor deformation parameter D (left axis, and continuous lines) and inclination angle θ (right axis, and dash lines) for two cases: $\text{Ca} = 0.6$, $\lambda = 1$ (thin lines), and $\text{Ca} = 0.6$, $\lambda = 13$ (thick lines). (d) Time-dependent particle stress components Σ_{xy} (black lines, left axis), N_1 (red lines, left axis), and N_2 (blue lines, right axis) for two cases: $\text{Ca} = 0.6$, $\lambda = 1$ (continuous lines), and $\text{Ca} = 0.6$, $\lambda = 13$ (dotted lines).

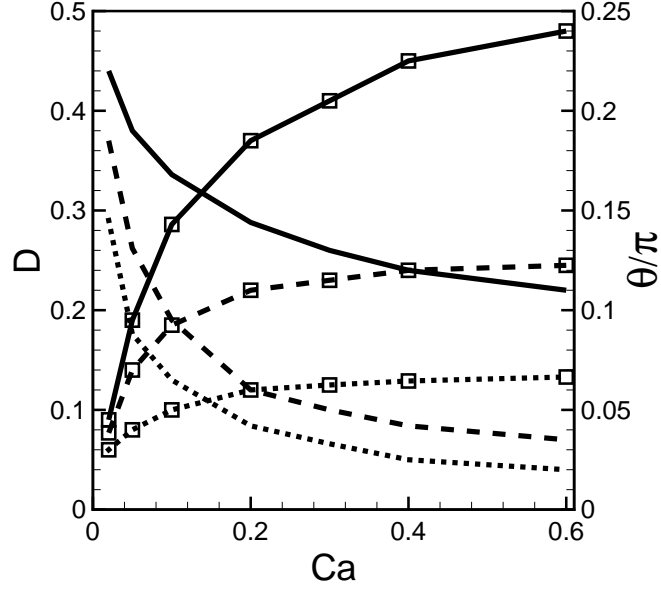


Figure 4.2: Steady-state values of the Taylor deformation parameter D (left axis, and lines with symbols) and the inclination angle θ (right axis, and lines without symbols) for capsules with SK model ($C = 1$). $\lambda = 1$ (continuous lines), 5 (dash lines), and 10 (dotted lines).

deformation parameter $D = (L - B)/(L + B)$ where L and B are the semi-major and minor axes of the deformed capsule in the shear plane. Also shown is the inclination angle θ that the major axis makes with the flow direction (x -axis). The $\lambda = 1$ case quickly reaches the steady state, whereas the $\lambda = 13$ case exhibits damped oscillations before reaching a steady state. Damped oscillations are typically observed for higher values of Ca and λ . Simulations are run for longer times (as shown in Fig. 4.1c) to ensure that such oscillations become negligible. Time evolution of Σ_{xy} , N_1 and N_2 are presented in Fig. 4.1d showing that they also reach steady values.

Steady-state values of D and θ as functions of Ca for various λ are shown

in Fig. 4.2 for SK model ($C = 1$). Deformation increases and θ decreases with increasing Ca and decreasing λ . These results agree well with previously published data [17, 50, 51].

4.3.2 Shear stress

We now come to the main focus of this article, which is the particle shear stress Σ_{xy} . The SK model with $C = 1$ is considered in Fig. 4.3. The variation of Σ_{xy} with Ca presented in Fig. 4.3a shows that Σ_{xy} decreases with increasing Ca for all values of λ . Hence, the capsule suspension exhibits a shear-thinning behavior.

The effect of the viscosity ratio λ is shown in Fig. 4.3b by keeping the capillary number fixed. Two different trends are observed at low and high values of Ca. Consider first the low values of Ca in the range $\text{Ca} \leq 0.1$. In this range Σ_{xy} decreases uniformly with increasing λ . This result is counter-intuitive as capsule deformation decreases with increasing λ (Fig. 4.2), and a reduced deformation should result an increase in Σ_{xy} . This result suggests that the trend of Σ_{xy} cannot be explained by capsule geometry alone.

The above result of decreasing Σ_{xy} with increasing λ is also in contradiction to that of a dilute emulsion of liquid drops with constant interfacial tension [52]. For a liquid drop emulsion, in the limit of small deformation, we have

$$\Sigma_{xy} = \frac{1 + 5\lambda/2}{1 + \lambda} \mu_o \dot{\gamma} \phi, \quad (4.10)$$

which gives an increasing Σ_{xy} with increasing λ , unlike the computed results for

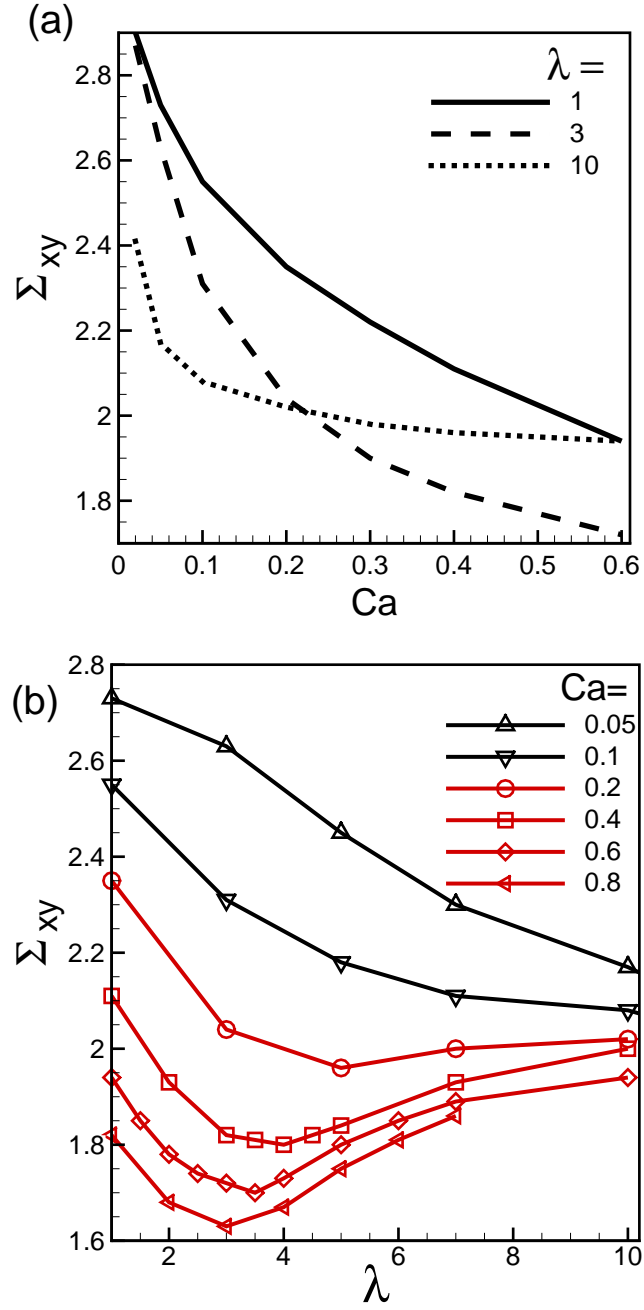


Figure 4.3: Particle shear stress Σ_{xy} for capsules with SK model ($C = 1$). (a) Effect of Ca at constant λ , and (b) effect of λ at constant Ca .

capsules. We however note that the small deformation theory of capsule suspension does predict a (linear) decrease of Σ_{xy} with increasing λ [44]. Furthermore, a similar trend is also predicted for emulsions of surfactant-covered liquid drops [53].

Consider now the trends of Σ_{xy} versus λ at higher shear rates ($\text{Ca} > 0.1$, Fig. 4.3b). We see a remarkably non-intuitive result: Σ_{xy} first decreases reaching a minimum, and then increases with increasing λ .

Hence, the capsule suspension exhibits a shear viscosity minimum at moderate values of viscosity ratio, and at high shear rates. In this respect, there is some qualitative similarity between the present results and those for vesicle suspension as predicted and observed by Misbah and co-workers [14, 47–49]. However, since the capsules in our simulations are in steady tank-treading motion, the physical mechanisms underlying the shear viscosity anomaly are completely different in capsule and vesicle suspensions, as will be shown later.

We note again that the shear viscosity minimum cannot be explained based on the capsule shape alone, as D and θ both decrease continually with increasing λ (Fig. 4.2). This anomalous behavior was not predicted by the small deformation theory of suspension of capsule or surfactant-covered drops [44, 53].

We now show that the shear viscosity minimum exists for strain-softening membranes as well. For this we present simulation results for capsules with NH model in Fig. 4.4. As before, the salient features of Fig. 4.4 are: (i) a shear-thinning behavior with respect to Ca , (ii) a uniform decrease of Σ_{xy} with increasing λ at low shear rates ($\text{Ca} \leq 0.05$), and (iii) an initial decrease of Σ_{xy} reaching

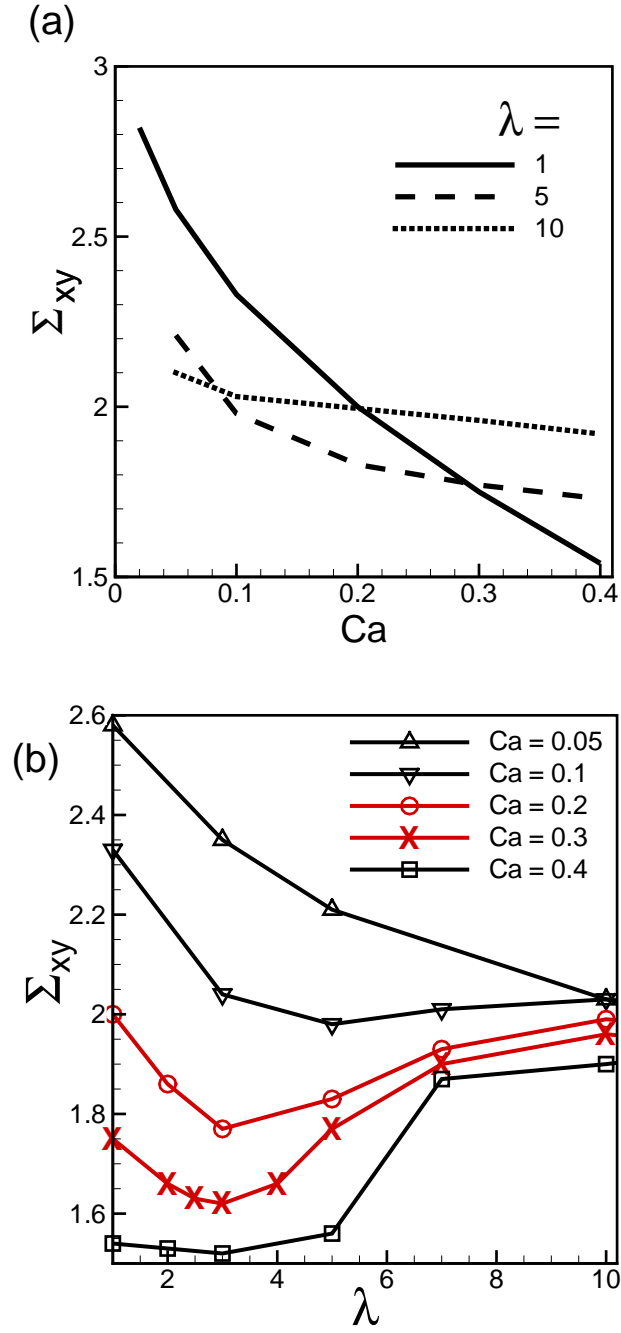


Figure 4.4: Particle shear stress Σ_{xy} for capsules with NH model. (a) Effect of Ca at constant λ , and (b) effect of λ at Ca .

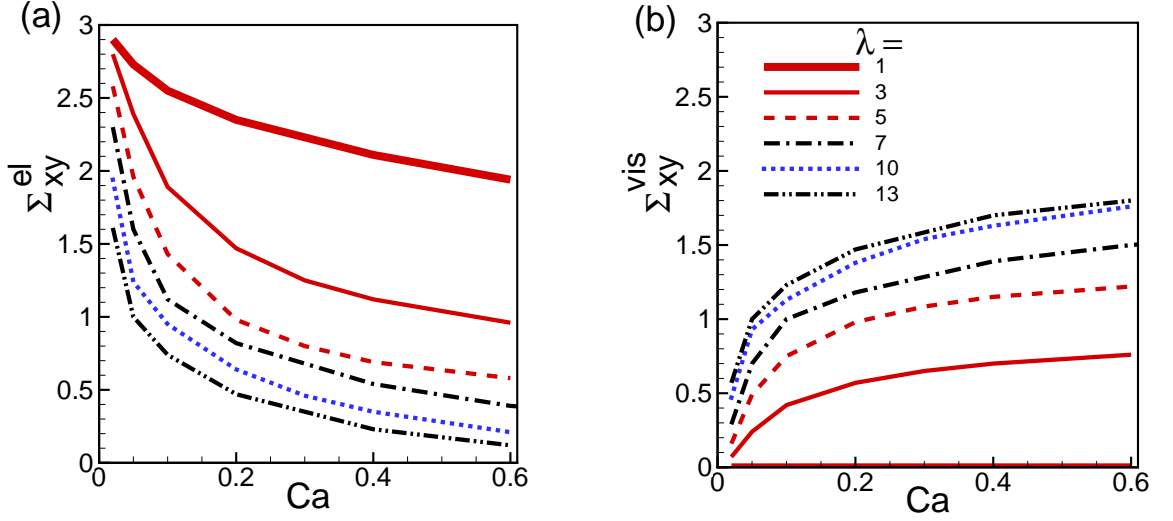


Figure 4.5: (Color online) Elastic (Σ_{xy}^{el}) and viscous (Σ_{xy}^{vis}) components with varying Ca for different values of λ for SK model with $C = 1$. Symbols have same meanings in (a) and (b).

a minimum, followed by an increase with λ at high shear rates ($Ca > 0.1$).

The non-trivial behavior of the shear stress observed in Figs. 4.3 and 4.4, and its differences with the results predicted by the small deformation theory for capsules, and vesicles, suggest that the bulk rheology is dictated not only by the capsule geometry (deformation and inclination), but also by the contributions coming from the membrane stress and viscosity contrast. Hence, we look at the elastic component Σ_{xy}^{el} and the viscous component Σ_{xy}^{vis} .

Fig. 4.5 shows Σ_{xy}^{el} and Σ_{xy}^{vis} as functions of Ca for various λ values. We see that the elastic contribution Σ_{xy}^{el} decreases with increasing Ca for all λ . More interestingly, however, we see that the viscous contribution Σ_{xy}^{vis} increases with increasing Ca . Thus the elastic contribution is shear-thinning in nature, but the viscous contribution is shear-thickening. At a fixed Ca , the elastic contribution

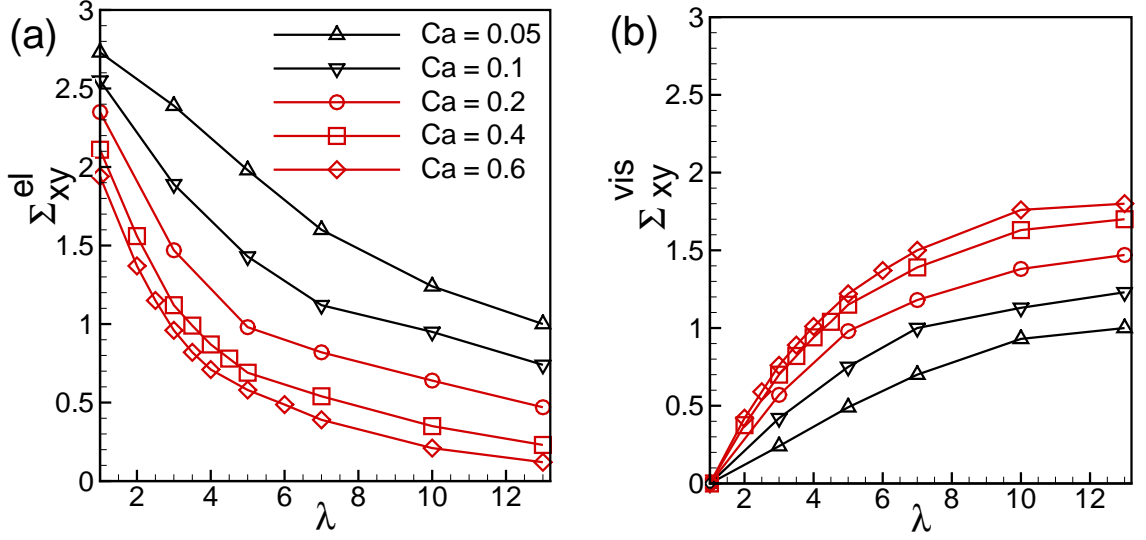


Figure 4.6: Elastic (Σ_{xy}^{el}) and viscous (Σ_{xy}^{vis}) components with varying λ for different Ca for SK model with $C = 1$. Symbols have same meanings in (a) and (b).

decreases, but the viscous contribution increases, with increasing λ . At low values of Ca and λ , the viscous contribution is smaller than the elastic contribution resulting a decreasing trend of Σ_{xy} with increasing Ca as observed in Figs. 4.3a and 4.4a. This trend is completely reversed at high values of Ca and λ , leading to a reduced shear-thinning behavior of the bulk suspension.

Next we explore the origin of shear viscosity minimum as observed in Fig. 4.3b. For this, we plot the variation of Σ_{xy}^{el} and Σ_{xy}^{vis} as a function of λ for different values of Ca in Fig. 4.6. The elastic contribution decreases, but the viscous contribution increases, with increasing λ . At low Ca , Σ_{xy}^{el} is mostly higher than Σ_{xy}^{vis} , and thus the total shear stress Σ_{xy} decreases with increasing λ as observed in Figs. 4.3b and 4.4b. At higher Ca , $\Sigma_{xy}^{el} > \Sigma_{xy}^{vis}$ for smaller values of λ , but $\Sigma_{xy}^{el} < \Sigma_{xy}^{vis}$ for larger

values of λ . Thus a minimum of Σ_{xy} occurs at intermediate values of λ , as observed in Figs. 4.3b and 4.4b. This analysis clearly shows that the opposite trends in Σ_{xy}^{el} and Σ_{xy}^{vis} with respect to λ are responsible for shear viscosity minimum in capsule suspension.

We now seek to explain the trends of the elastic and viscous components. The elastic component Σ_{xy}^{el} can be further decomposed into two contributions. The first one depends on capsule shape and alignment alone and can be written as

$$\Sigma^{\text{el,iso}} = -\Gamma \int_A \left(\mathbf{nn} - \frac{\mathbf{I}}{3} \right) dA \quad (4.11)$$

where the constant Γ represents an isotropic membrane tension. The second contribution arises from the anisotropic distribution of the membrane tension. For a liquid drop with a constant surface tension, Γ becomes the surface tension, and the anisotropic part vanishes. Then, $\Sigma^{\text{el}} = \Sigma^{\text{el,iso}}$ which depends only on the drop shape and alignment. For a capsule, the anisotropic contribution is non-zero. We seek to address if the above isotropic model can qualitatively explain the trends of Σ_{xy}^{el} as observed in Figs. 4.5 and 4.6.

Fig. 4.7 shows $\Sigma^{\text{el,iso}}$ evaluated using Eq. 4.11 for oblate spheroids of aspect ratio (semi-major to minor axes) $\alpha = 1, 1.25$, and 1.67 , as a function of the inclination angle θ . The results are shown in arbitrary units, and taking $\Gamma = 1$. For the stationary capsule dynamics, only the results between $\theta = \pi/4$ and 0 are of interest. We see that $\Sigma^{\text{el,iso}} = 0$ for $\alpha = 1$ at any inclination angle, as expected. For $\alpha \neq 1$, $\Sigma_{xy}^{\text{el,iso}}$ is maximum at $\theta = \pi/4$, and it decreases with

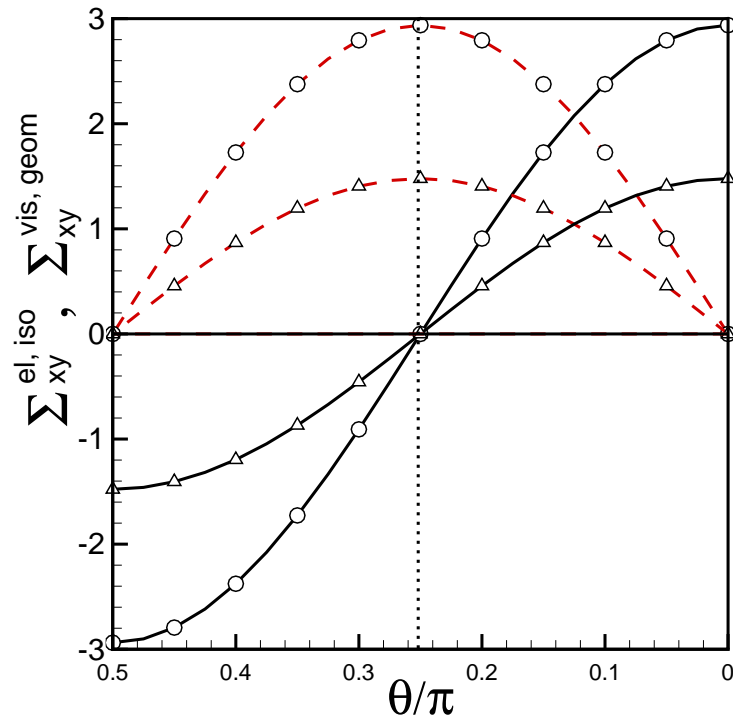


Figure 4.7: (Color online) Variation of $\Sigma_{xy}^{\text{el, iso}}$ (solid, black lines), and $\Sigma_{xy}^{\text{vis, geom}}$ (dash red lines) as functions of inclination angle θ for shape-preserving oblate spheroids for aspect ratios 1 (no symbol), 1.25 (triangles), and 1.67 (circles).

decreasing θ and increasing α . This result can completely explain the qualitative trends of numerically obtained Σ_{xy}^{el} seen in Figs. 4.5 and 4.6. Increasing the capillary number results increasing deformation (i.e. increasing α , in this model), and decreasing θ . Increasing the viscosity contrast causes decreasing deformation (i.e., decreasing α) and decreasing θ . Thus, the qualitative trend of Σ_{xy}^{el} follows that of $\Sigma_{xy}^{\text{el,iso}}$.

Now we analyze the qualitative trends of the viscous contributions Σ_{xy}^{vis} . At steady-state, the shape of the capsule and its alignment with the flow direction are fixed (for the unstressed spherical shape considered here) while the capsule membrane undergoes the tank-treading motion. Then the membrane velocity can be expressed as $\mathbf{u}(\mathbf{x}', t) = |\mathbf{u}(\mathbf{x}', t)|\mathbf{t}$ where \mathbf{t} is tangent to the capsule surface in shear plane. Approximating the membrane velocity \mathbf{u} by a/T where T is the tank-treading period, we write

$$\Sigma^{\text{vis}} \approx \frac{a\mu_o(\lambda - 1)}{TV} \int_A (\mathbf{t}\mathbf{n} + \mathbf{n}\mathbf{t}) \, dA \quad (4.12)$$

Then, we introduce $\Sigma^{\text{vis,geom}}$ as

$$\Sigma^{\text{vis,geom}} = \int_A (\mathbf{t}\mathbf{n} + \mathbf{n}\mathbf{t}) \, dA \quad (4.13)$$

which depends only on the geometry. Neglecting the effect of T , the integral in Eq. 4.13 is used to illustrate the trends of Σ_{xy}^{vis} . For this purpose, $\Sigma_{xy}^{\text{vis,geom}}$ is evaluated using Eq. 4.13 for oblate spheroids for aspect ratios $\alpha = 1, 1.25$, and

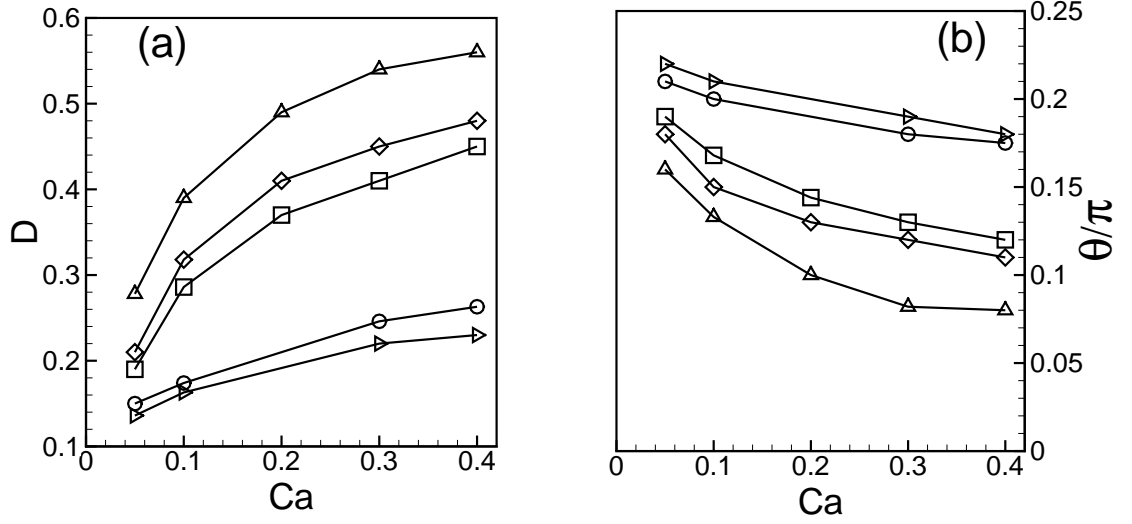


Figure 4.8: Effect of area dilatation on (a) capsule deformation and (b) inclination angle. Symbols represent NH model (Δ), and SK models with $C = 0.1$ (\diamond), 1 (\square), 50 (\circ), and 100 (\triangleright).

1.67, and plotted in Fig. 4.7 as a function of θ . We see that $\Sigma_{xy}^{\text{vis,geom}} = 0$ for $\alpha = 1$, as expected. For $\alpha > 1$, $\Sigma_{xy}^{\text{vis,geom}}$ is minimum at $\theta = \pi/4$, and it increases with decreasing θ and increasing α . Recalling that deformation increases and θ decreases with increasing Ca , we see that the trend of $\Sigma_{xy}^{\text{vis,geom}}$ can explain the trends of Σ_{xy}^{vis} with Ca . Recalling further that both deformation D and inclination θ decrease with increasing λ , we see again that Σ_{xy}^{vis} follows the same trend as $\Sigma_{xy}^{\text{vis,geom}}$ with varying λ .

4.3.3 Effect of area dilatation

Next we consider the effect of capsule surface area dilatation. Fig. 4.8 shows the steady-state deformation parameter D and inclination angle θ as functions of Ca for five cases: the NH model, and the SK model with $C = 0.1, 1, 50$, and

100. The viscosity contrast is fixed at $\lambda = 1$. For all cases, D increases and θ decreases with increasing Ca . In contrast, increasing the values of C results in reduced deformation and higher inclination angle. Reduced deformation at higher values of C is achieved via reduced surface area dilatation. The area dilatation is maximum for the neo-Hookean membrane for which the area increases by 4.5% and 29% of the initial area for $\text{Ca} = 0.05$ and 0.4, respectively. For the SK model at $C = 1$, the area increases by 1.5% and 14.1% for $\text{Ca} = 0.05$ and 0.4, respectively. At $C = 100$, the respective area increases are only 0.16% and 1.8%.

The effect of area-dilatation on Σ_{xy} is shown in Fig. 4.9 by considering four cases: the NH model, and the SK model with $C = 0.1, 1$, and 50. Fig. 4.9a shows Σ_{xy} as a function of Ca at a constant viscosity contrast $\lambda = 1$. The shear-thinning behavior is prominent for the NH model, and for SK model at high area dilatation (i.e., low to moderate values of C). At $C \geq 50$, the shear-thinning behavior is nearly absent due to a reduced capsule deformation.

Increasing the values of C also results in increasing values of Σ_{xy} . This can be understood based on the reduction of capsule deformation with increasing C as observed in Fig. 4.8.

Fig. 4.9b shows the variation of Σ_{xy} with respect to λ by keeping the capillary number fixed at 0.4. For the SK model with $C = 0.1$ and 1, Σ_{xy} first reaches a minimum, and then increases with increasing λ . For $C \geq 50$, Σ_{xy} is observed to decrease continually with increasing λ . Thus, for a capsule suspension, the shear

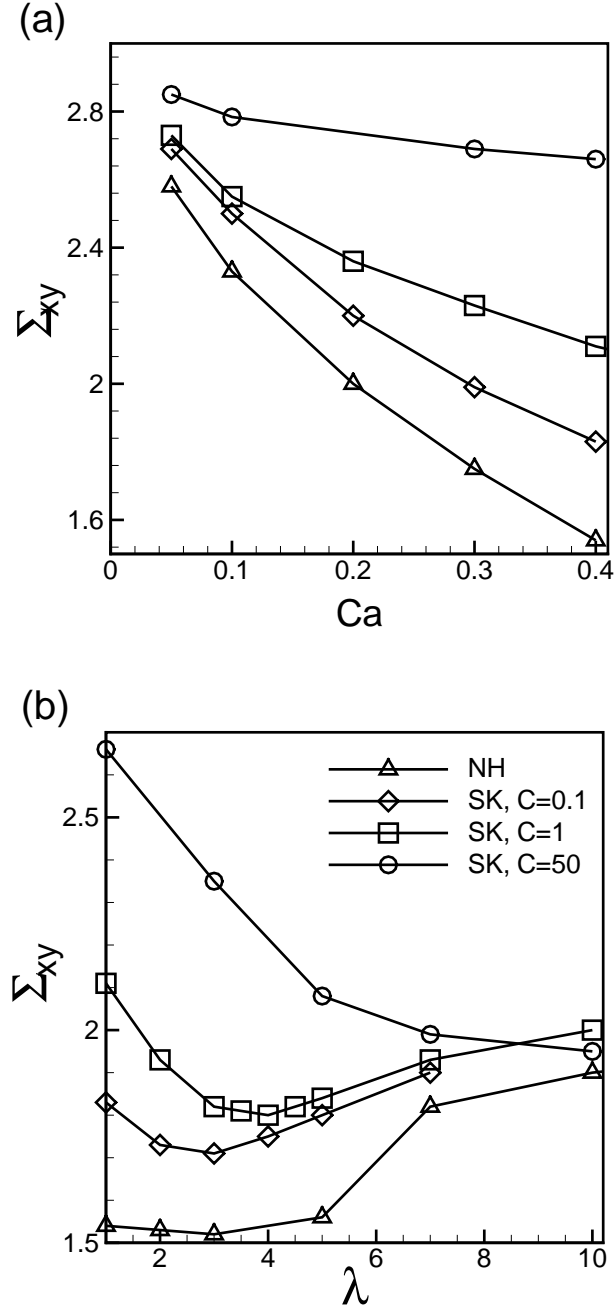


Figure 4.9: Effect of area dilatation on Σ_{xy} . (a) variation with respect to Ca at $\lambda = 1$; and (b) variation with respect to λ at $Ca = 0.4$. Symbols represent NH model (Δ), and SK models with $C = 0.1$ (\diamond), 1 (\square), and 50 (\circ).

viscosity minimum is observed for area-dilating membranes but not for nearly-incompressible membranes.

The absence of shear viscosity minimum for nearly-incompressible membranes can be understood again by decomposing the shear stress Σ_{xy} in to its elastic and viscous components. Fig. 4.10a shows Σ_{xy}^{el} and Σ_{xy}^{vis} with increasing λ . We see that with increasing λ , the elastic contribution Σ_{xy}^{el} decreases, but the viscous contribution Σ_{xy}^{vis} increases. At a fixed value of λ , the elastic contribution is the lowest for the NH model, and it increases with increasing values of C for the SK model. In contrast, the viscous contribution is the maximum for the NH model, and it decreases with increasing values of C for the SK model. For the SK model with $C = 50$, Σ_{xy}^{el} is significantly higher than Σ_{xy}^{vis} for lower values of λ . At higher λ values, Σ_{xy}^{el} continues to drop at a faster rate. This explains the monotonically declining trend of Σ_{xy} with λ for the $C = 50$ case, and hence, for nearly-incompressible membranes.

Some interesting results for the SK model can be deduced by further decomposing the elastic component as

$$\Sigma^{\text{el}} = \Sigma^{\text{sh}} + \Sigma^{\text{di}} \quad (4.14)$$

where Σ^{sh} represents the contribution from the shear elasticity E_s , and Σ^{di} represents the contribution from the area-dilatation modulus E_a . Fig. 4.10b shows Σ_{xy}^{sh} and Σ_{xy}^{di} as functions of λ for various values of C . Both Σ_{xy}^{sh} and Σ_{xy}^{di} decline with

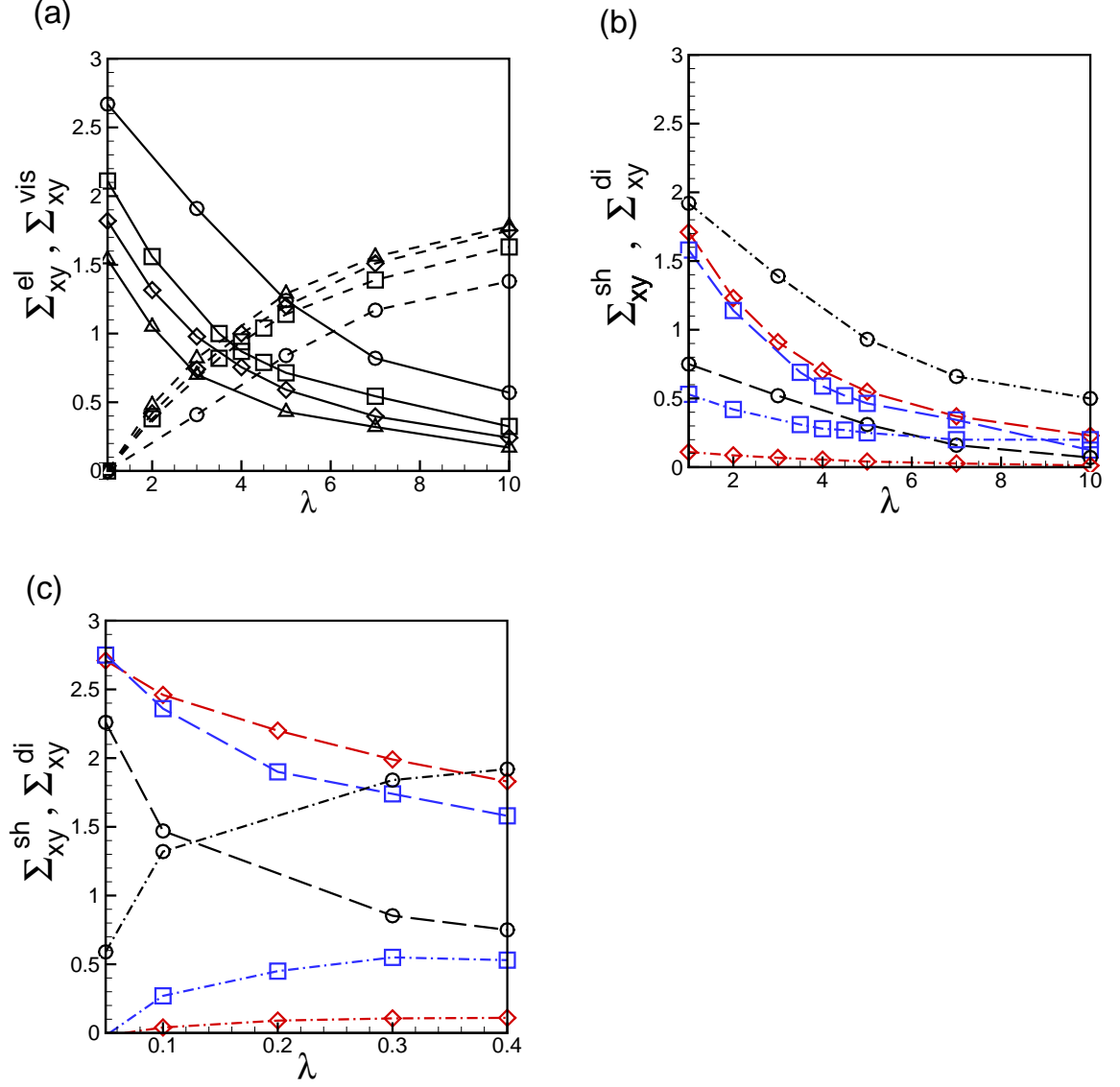


Figure 4.10: (Color online) Effect of area dilatation on Σ_{xy}^{el} and Σ_{xy}^{vis} . Symbols represent NH model (Δ), and SK models with $C = 0.1$ (\diamond), 1 (\square), and 50 (\circ). (a) Variation of Σ_{xy}^{el} (continuous lines) and Σ_{xy}^{vis} (dash lines) with λ at $Ca = 0.4$. (b) Variation of Σ_{xy}^{sh} (long dash lines) and Σ_{xy}^{di} (dash-dot lines) with λ at $Ca = 0.4$. (c) Variation of Σ_{xy}^{sh} (long dash lines) and Σ_{xy}^{di} (dash-dot lines) with Ca at $\lambda = 1$.

increasing λ . At a fixed value of λ , Σ_{xy}^{sh} decreases, but Σ_{xy}^{di} increases, with increasing C . At large values of λ and C , Σ_{xy}^{di} exceeds Σ_{xy}^{sh} by several factors implying that the area-dilatation characteristics strongly affects the bulk rheology.

Ca-dependence of Σ_{xy}^{sh} and Σ_{xy}^{di} is shown in Fig. 4.10c. Opposite trends for Σ_{xy}^{sh} and Σ_{xy}^{di} are observed. Σ_{xy}^{sh} decreases but Σ_{xy}^{di} increases with increasing Ca. For nearly incompressible membranes ($C = 50$) at high capillary numbers, Σ_{xy}^{di} exceeds Σ_{xy}^{sh} by several factors. Hence, as noted above, the membrane area-dilatation significantly affects the bulk shear stress.

4.3.4 Normal stress differences

The normal stress differences N_1 and N_2 for capsules with the SK model are shown in Fig. 4.11. Positive values of N_1 and negative values of N_2 , with $|N_2| < N_1$, are observed for all cases, as typical of emulsions. The dependence of the normal stress differences on Ca and λ is counterintuitive. At $\lambda = 1$, both N_1 and $|N_2|$ increase with increasing Ca indicating an increasing elastic nature of the emulsion. At $\lambda = 3$, N_1 and $|N_2|$ first increase with increasing Ca, but attain constant values at higher shear rates. For $\lambda = 5$ and 7, N_1 and $|N_2|$ first increase to maximum values, but then decrease with increasing Ca. For $\lambda = 10$, and 13, N_1 and $|N_2|$ monotonically decreases with increasing Ca, thus completely reversing the trend seen at $\lambda = 1$.

It is worth mentioning that the trends of computed N_1 and N_2 as observed in Fig. 4.11 are completely different from those predicted by the small deformation

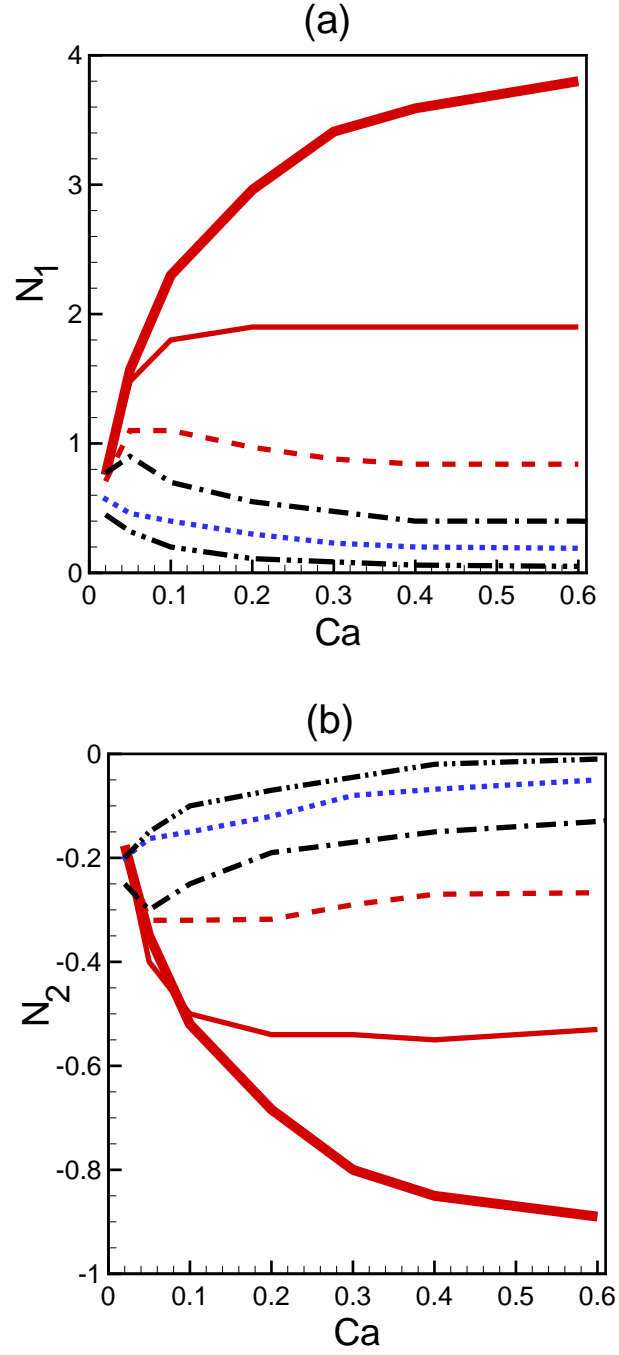


Figure 4.11: (Color online) N_1 and N_2 for capsules with SK model ($C = 1$). $\lambda = 1$ (thick red lines), 3 (thin red lines), 5 (dash red lines), 7 (black dash-dot lines), 10 (blue dotted lines), and 13 (black dash-dot-dot lines).

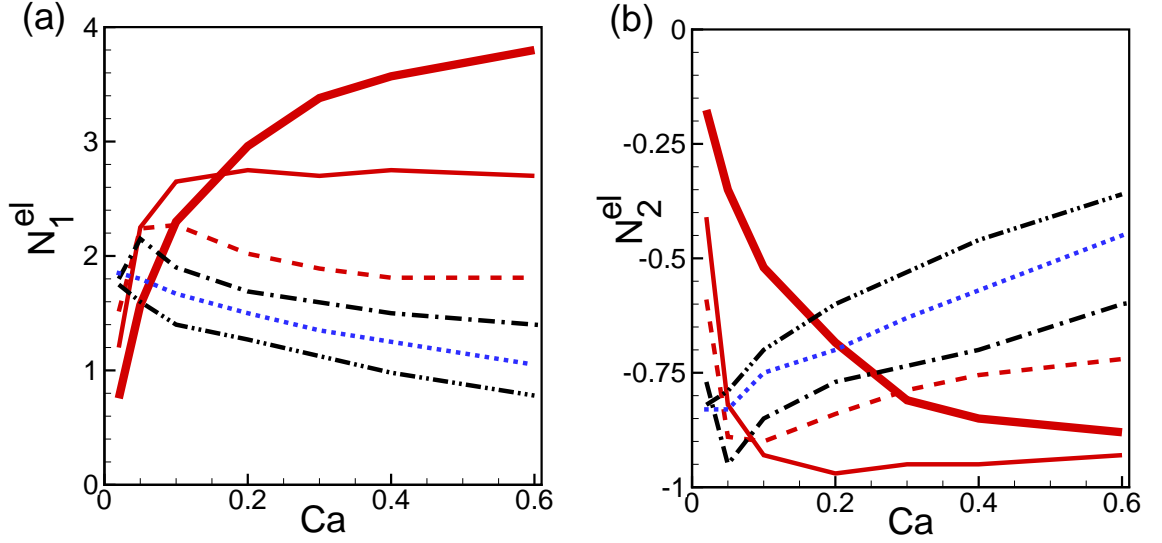


Figure 4.12: (Color online) Effect of Ca on the elastic contributions (a) N_1^{el} , and (b) N_2^{el} for SK model with $C = 1$. Line patterns represent different values of λ as in Fig. 4.11. $\lambda = 1$ (thick red lines), 3 (thin red lines), 5 (dash red lines), 7 (black dash-dot lines), 10 (blue dotted lines), and 13 (black dash-dot-dot lines).

theories. As mentioned before, the second-order theory of capsule deformation, and the third-order theory for surfactant-covered liquid drops predict that N_1 and $|N_2|$ depend linearly on Ca but independent of λ [44, 53]. In contrast, the computed values show a non-linear dependence on Ca and λ .

It is also worth noting the differences with the theoretical results for vesicle suspension. Similar to Σ_{xy} , the theoretical analysis for vesicle suspension predicts that N_1 first reaches a minimum and then increases with increasing values of λ [48]. In contrast, our computations suggest that N_1 and $|N_2|$ decrease uniformly with increasing λ .

We now explain the trends of N_1 and N_2 by looking at the viscous and elastic

components. We recall from Eq. 4.8 that

$$N_1 = N_1^{\text{el}} + N_1^{\text{vis}}, \quad (4.15)$$

and

$$N_2 = N_2^{\text{el}} + N_2^{\text{vis}}. \quad (4.16)$$

The elastic components N_1^{el} and N_2^{el} with Ca are shown in Fig. 4.12. We see that N_1^{el} is positive, and larger than N_1 , whereas N_2^{el} is negative, and its magnitude is larger than $|N_2|$. This is because, as will be seen later, the viscous component N_1^{vis} is negative, and N_2^{vis} is positive. We also note that for $\lambda = 1$, $N_1^{\text{el}} = N_1$ and $N_2^{\text{el}} = N_2$ since the viscous component is absent, and that N_1^{el} and $|N_2^{\text{el}}|$ increase with increasing Ca following the trends of N_1 and $|N_2|$. For $\lambda > 1$, however, a remarkably different behaviour is observed. For $\lambda = 3$, N_1^{el} and $|N_2^{\text{el}}|$ rapidly increase but then become independent of Ca. For $\lambda \geq 5$, N_1^{el} and $|N_2^{\text{el}}|$ first increase to a maximum, but then decrease with increasing Ca. This trend is completely different from that observed at $\lambda = 1$. This behavior implies that at high viscosity contrast, the elastic nature of the suspension diminishes with increasing shear rates. Thus, the capsule suspension exhibits elastic normal stress maximums at moderate viscosity differences and shear rates.

The anomalous trends of N_1^{el} and N_2^{el} at high viscosity contrast are further explored in Fig. 4.13 where the variations with respect to λ at fixed values of

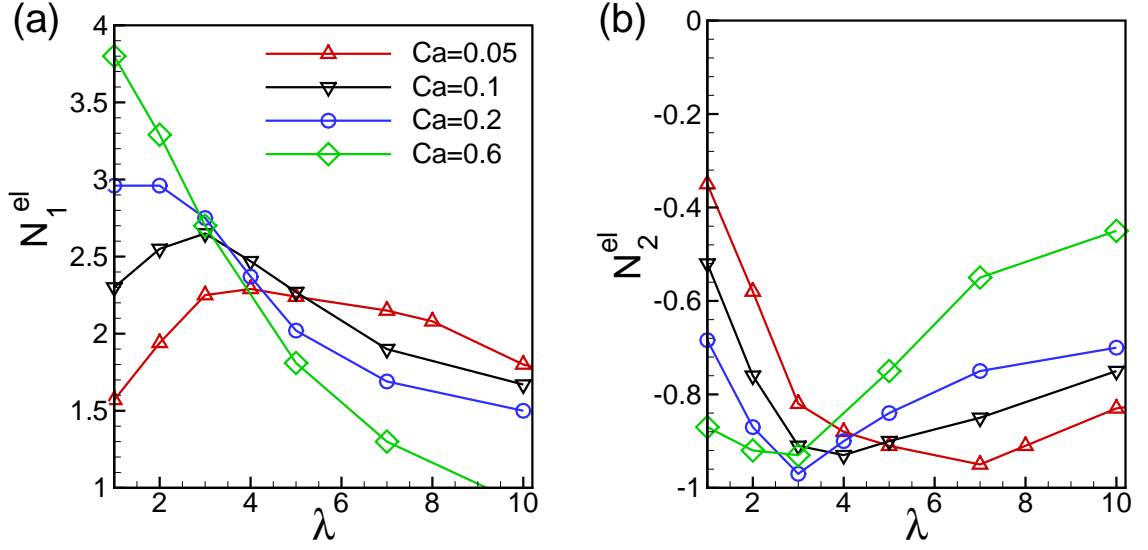


Figure 4.13: (Color online) Effect of λ on the elastic contributions (a) N_1^{el} , and (b) N_2^{el} for SK model with $C = 1$. Line patterns represent different values of Ca as indicated.

Ca are considered. The figure clearly shows that at smaller values of λ , the magnitudes of the elastic components increase with increasing Ca , while the trend is reversed at larger values. For $\text{Ca} = 0.05$ and 0.1 , N_1^{el} and $|N_2^{\text{el}}|$ first increase, and then decrease with increasing λ . For $\text{Ca} \geq 0.6$, N_1^{el} and $|N_2^{\text{el}}|$ continually decrease with increasing λ .

We now investigate if the complex trends of N_1^{el} and N_2^{el} can be predicted by the isotropic model given by Eq. 4.11, which accounts for capsule geometry only. Fig. 4.14 shows $N_1^{\text{el,iso}}$ and $N_2^{\text{el,iso}}$ computed using Eq. 4.11 for oblate spheroids of aspect ratio $\alpha = 1, 1.25$, and 1.67 , with varying θ . The results are shown in arbitrary units taking $\Gamma = 1$. For $\alpha = 1$, we see that $N_1^{\text{el,iso}} = N_2^{\text{el,iso}} = 0$ at any θ , as expected. For $\alpha > 1$, $N_1^{\text{el,iso}}$ and $|N_2^{\text{el,iso}}|$ increase with increasing α and decreasing θ . This trend is the same that was observed for N_1^{el} and N_2^{el} for $\lambda = 1$,

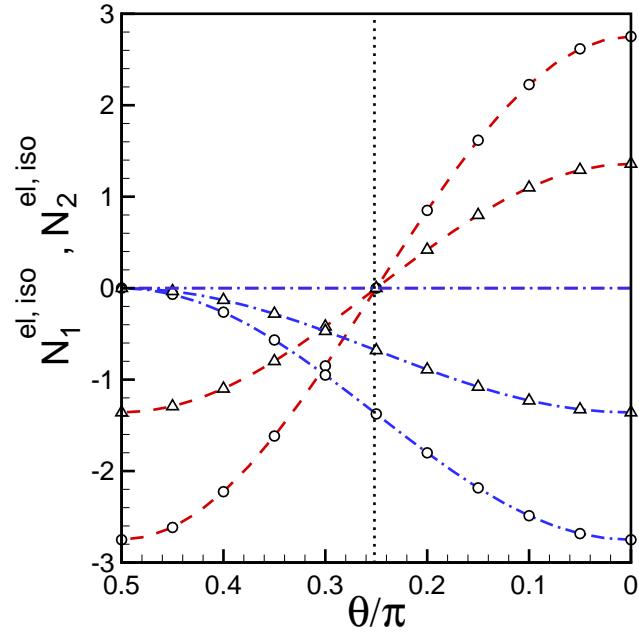


Figure 4.14: Variation of $N_1^{\text{el, iso}}$ (red dash lines) and $N_2^{\text{el, iso}}$ (blue dash-dot lines) as functions of inclination angle θ for shape-preserving oblate spheroids for aspect ratios 1 (no symbol), 1.25 (triangles), and 1.67 (circles).

but not for $\lambda > 1$ (Figs. 4.12 and 4.13). Thus, the isotropic model fails to explain the trends of N_1^{el} N_2^{el} for $\lambda > 1$.

For $\lambda > 1$, it appears that the anisotropy of the membrane tension contributes significantly to the elastic components. This can be illustrated by looking at the distribution of the membrane principal tensions

$$\tau_1 = \frac{1}{\epsilon_2} \frac{\partial W}{\partial \epsilon_1}, \quad \tau_2 = \frac{1}{\epsilon_1} \frac{\partial W}{\partial \epsilon_2}. \quad (4.17)$$

Figs. 4.15 and 4.16 show the contours of τ_1 and τ_2 for $\lambda = 1$ and 7, respectively, for two capillary numbers, 0.05 and 0.4. Consider first the $\lambda = 1$ case (Fig. 4.15). We see that τ_1 is always positive, but τ_2 can be negative (which is indicative of a compressive stress). The magnitudes of τ_1 and τ_2 contours increase with increasing Ca, and positive values of τ_2 dominate at higher capillary numbers. Thus, the integrated effect of the membrane tensions is to increase the magnitudes of N_1^{el} and N_2^{el} with increasing Ca as observed in Fig. 4.12 for $\lambda = 1$. Consider now the $\lambda = 7$ case (Fig. 4.16). At Ca = 0.05, the contours of τ_1 and τ_2 are similar to those obtained at $\lambda = 1$. But at Ca = 0.4, we see that τ_1 has become negative, and τ_2 is dominantly negative. The integrated effect of such negative membrane tensions is to reduce the values of N_1^{el} and $|N_2^{\text{el}}|$. Hence, N_1^{el} and N_2^{el} , unlike $N_1^{\text{el,iso}}$ and $N_2^{\text{el,iso}}$, exhibit non-monotonic trends with respect to Ca and λ due to the non-monotonic trends of the membrane tensions.

The viscous components of the normal stress differences, N_1^{vis} and N_2^{vis} , are shown in Fig. 4.17. The viscous components have opposite signs when compared

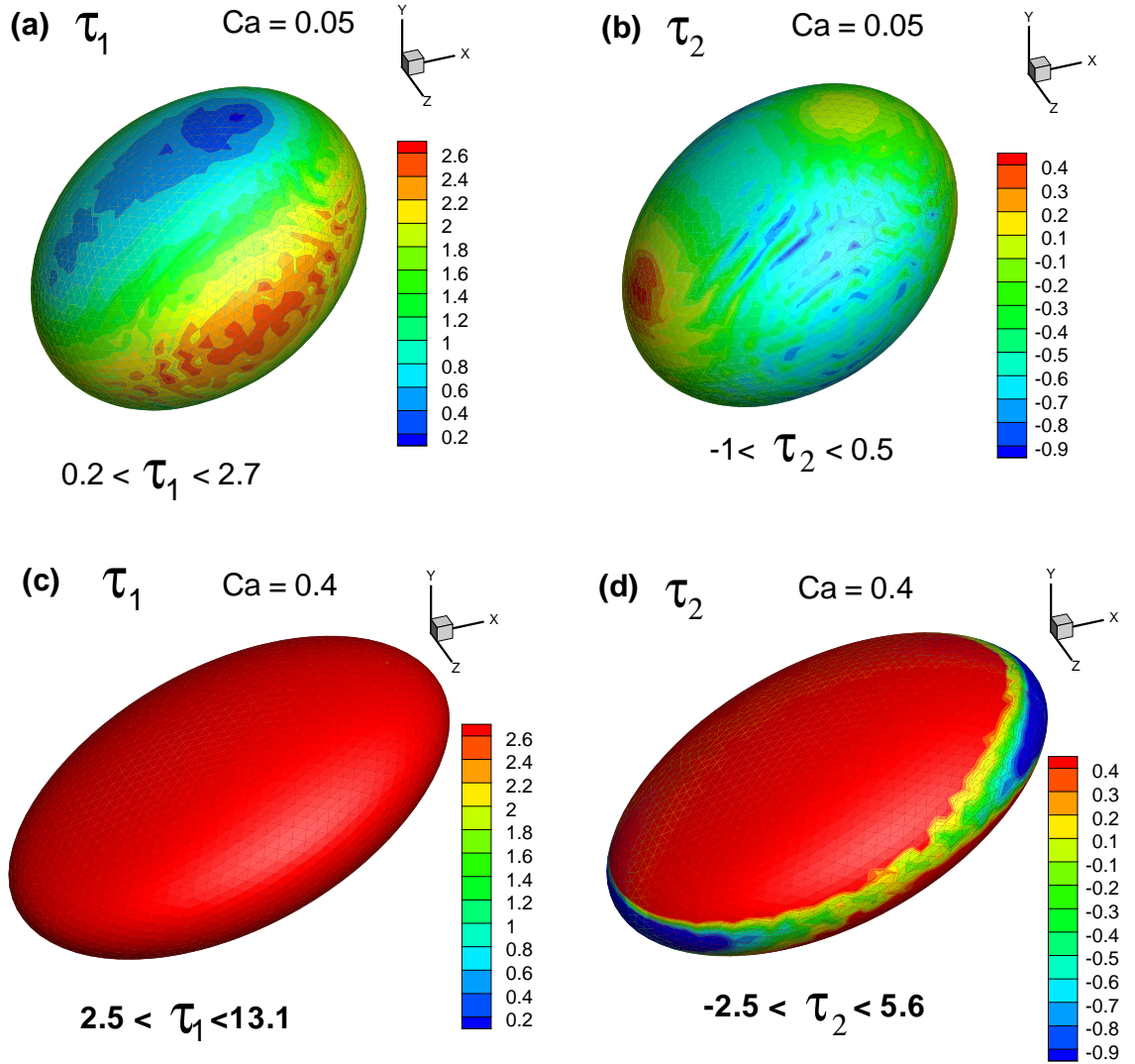


Figure 4.15: (Color online) Distribution of the principal membrane tensions τ_1 and τ_2 for $\lambda = 1$ for two capillary numbers 0.05 (a,b) and 0.4 (c,d). The color changes from red to blue as the values change from positive to negative, respectively. The contour ranges are indicated for each case.

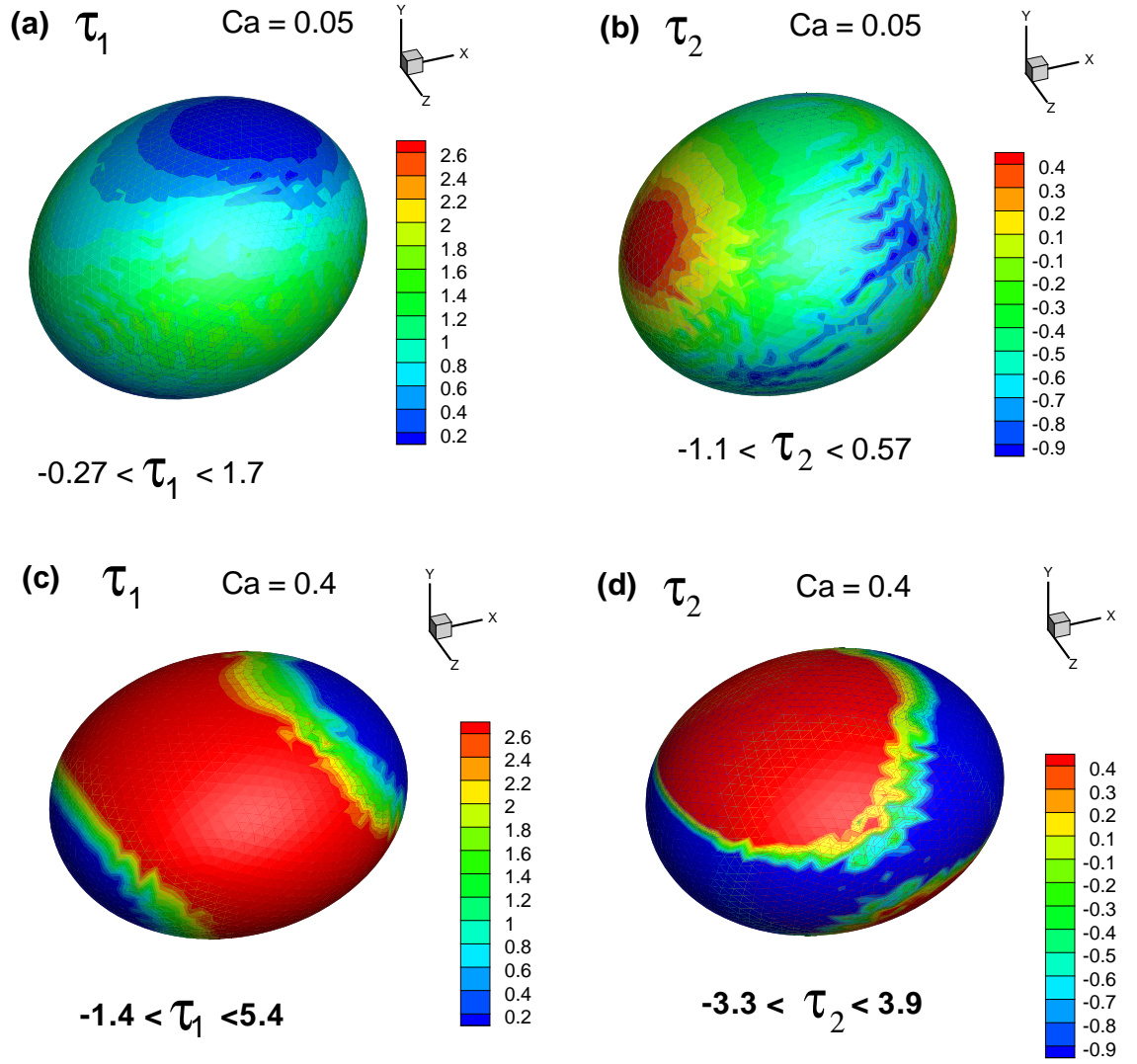


Figure 4.16: (Color online) Same as in Fig. 4.15 but for $\lambda = 7$, and $Ca = 0.05$ (a,b) and 0.4 (c,d).

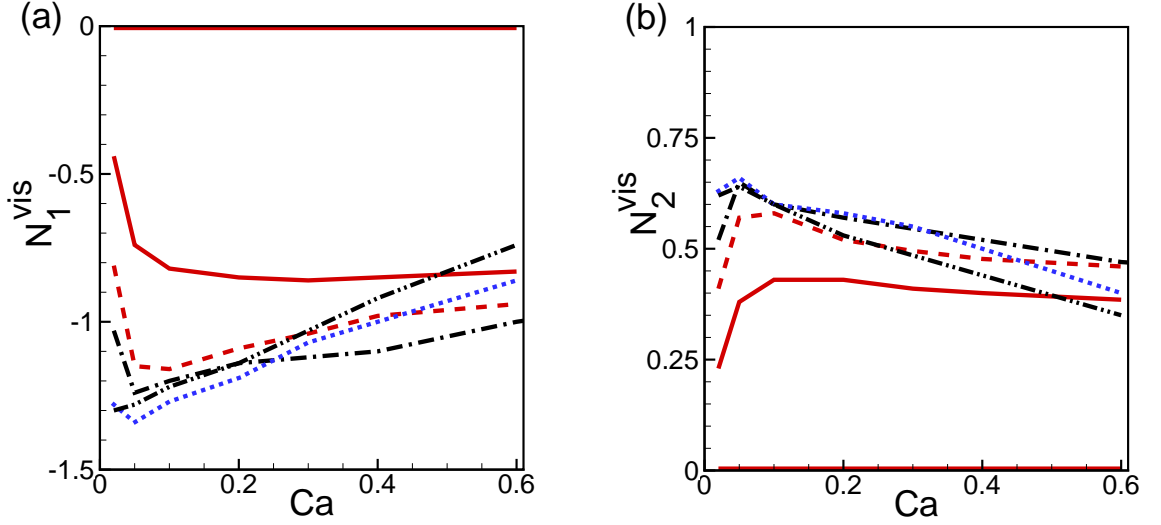


Figure 4.17: (Color online) Effect of Ca on the viscous contributions (a) N_1^{vis} , and (b) N_2^{vis} for SK model with $C = 1$. Line patterns represent different values of λ as in Fig. 4.11. $\lambda = 1$ (thick red lines), 3 (thin red lines), 5 (dash red lines), 7 (black dash-dot lines), 10 (blue dotted lines), and 13 (black dash-dot-dot lines).

with their elastic counterparts; N_1^{vis} is negative, and N_2^{vis} is positive. Figs. 4.17a and 4.17b illustrate the Ca -dependence of N_1^{vis} and N_2^{vis} . Interesting behavior is noted when variations with respect to Ca at $\lambda \geq 5$ are considered. In this range, $|N_1^{\text{vis}}|$ and N_2^{vis} first increase reaching maximum values, and then decrease with increasing Ca . This non-monotonic trend is quite different from that observed for Σ_{xy}^{vis} which monotonically increases with increasing Ca .

The trends of $|N_1^{\text{vis}}|$ and N_2^{vis} versus Ca can be partly explained based on the isotropic model. Using Eq. 4.13 we can evaluate $N_1^{\text{vis,geom}}$ and $N_2^{\text{vis,geom}}$ for oblate spheroids for different values of aspect ratio α and inclination angle θ . It appears that $|N_1^{\text{vis,geom}}|$ and $N_2^{\text{vis,geom}}$ are maximum at $\theta = \pi/4$, and they decrease with decreasing θ and increasing α . In the limits that $\alpha \rightarrow 1$ (i.e., Ca

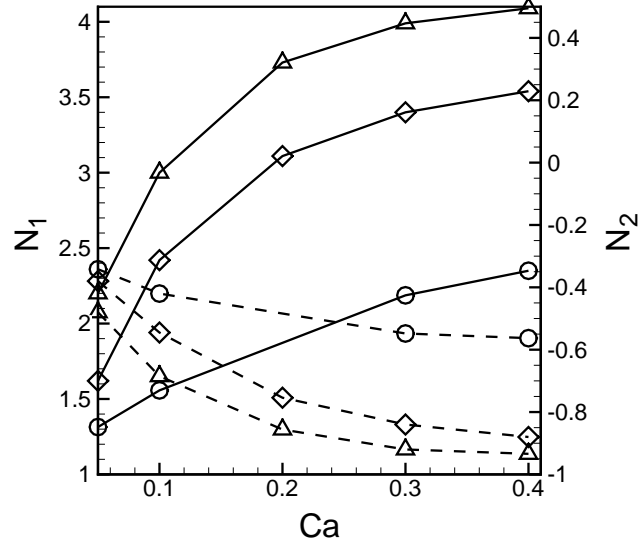


Figure 4.18: Effect of area dilatation on N_1 (continuous line, left axis) and N_2 (dash lines, right axis). Variation with respect to Ca is shown at $\lambda = 1$. Symbols represent NH model (Δ), and SK models with $C = 0.1$ (\diamond), and 50 (\circ).

$\rightarrow 0$), and $\theta \rightarrow 0$ ($Ca \rightarrow \infty$), both $N_1^{\text{vis,geom}}$ and $N_2^{\text{vis,geom}}$ vanish. Then, the maximum values of $|N_1^{\text{vis,geom}}|$ and $N_2^{\text{vis,geom}}$ (and, hence, $|N_1^{\text{vis}}|$ and N_2^{vis}) occur at intermediate values of Ca . As a result, N_1^{vis} and N_2^{vis} exhibit non-monotonic trends with increasing Ca .

Based on the above results on elastic and viscous components, we can now explain the trends of N_1 and N_2 as seen earlier in Fig. 4.11. The above observation suggests that the magnitudes of elastic and viscous components first rapidly increase, and then decrease with increasing Ca for moderate to large values of λ ; the larger the value of λ , the faster the decrease. This explains why N_1 and N_2 approach to zero with increasing Ca and at a faster rate with increasing λ .

Effect of area dilatation on normal stress differences is shown in Fig. 4.18

by considering three cases: the NH model, and the SK model with $C = 0.1$, and 50. For all cases, N_1 and $|N_2|$ increase non-linearly, and eventually tend to saturate with increasing Ca . As expected, $N_1 > 0$, $N_2 < 0$, and $N_1 > |N_2|$, for all cases. However, N_1 and $|N_2|$ decrease with increasing C due to reduced capsule deformation. Thus the elastic nature of the bulk suspension is reduced with decreasing area-dilatation of the membrane.

Chapter 5

Conclusion

5.1 Dynamics of Ellipsoidal Capsules

In Chapter 3, we presented numerical results on the dynamics of oblate shape capsules in shear flow by considering a broad range of viscosity contrast, capillary number, and aspect ratio. The focus is on the coupling between the shape deformation and orientation dynamics, and how this coupling affects the transition dynamics as a function of the viscosity contrast. At low values of Ca , three distinct modes of capsule dynamics are identified: (i) At a low value of λ , a swinging or oscillatory (OS) mode occurs during which the capsule oscillates about a mean inclination angle, but the major axis always lies in the extensional quadrant of the shear flow, so that $0 < \theta(t) < \pi/4$; the oscillatory motion co-exists with the tank-treading of the membrane. (ii) At a moderate value of λ , a vacillating-breathing (VB) mode occurs during which the capsule swings vigorously about the mean inclination angle which is close to zero, and $\theta(t)$ periodically becomes positive and negative, but a full tumbling does not occur; a significant compression occurs in this mode leading to the maximum shape deformation. (iii) At even higher values of λ , a pure tumbling mode (TU) occurs; even in this mode, significant

shape deformation is observed.

The VB mode of capsules as shown in this chapter is qualitatively similar to that for vesicles described in earlier works, e.g, [9,10,14,26–28]. These modes occur because, at the intermediate values of λ , the capsule undergoes a significant compression when $\theta(t)$ becomes negative, leading to the near-circular shape, and a reduced hydrodynamic torque. The capsule, as a result, is unable to make a full tumbling motion. Due to the significant compression, the capsule shapes in the extensional and compressional quadrants of the flow are not mirror images about the mean inclination angle. Furthermore, the compression of the capsule occurs at a slower time scale, while the elongation occurs much faster. Thus, in the VB mode, the clockwise swing occurs slower than the counter-clockwise swing.

At higher capillary numbers, three types of transient motions occur, in addition to the OS and TU modes, during which the capsule switches from one mode to the other. With increasing λ , these modes appear as (i) VB \rightarrow OS, (ii) TU \rightarrow VB \rightarrow OS, and (iii) TU \rightarrow VB.

We analyze the coupling between the shape deformation and orientation dynamics, and show how this coupling influences the transition from tank-treading to tumbling motion as the viscosity contrast is increased. For all modes of motion (OS, VB, TU), a large amplitude oscillation in capsule shape is observed. The coupling between the shape deformation and orientation is the strongest in the VB mode during which the amplitude of shape deformation ΔD reaches its maximum, and the capsule shape shows the maximum compression. Hence the

shape deformation is most important at an intermediate viscosity contrast around $\lambda = \lambda_c$.

The coupling between the orientation dynamics and the shape deformation leads to a number of significant departures from the KS theory. (i) According to the KS model, a steady inclination angle exists for $\lambda < \lambda_c$, whereas the numerical results show that a steady inclination angle does not exist at a low value of λ . (ii) In the KS model, tumbling starts as soon as $\theta(t)$ becomes negative which happens at $\lambda = \lambda_c$. The numerical results show that as λ approaches λ_c , the inclination angle $\theta(t)$ can become negative without a full tumbling of the capsule. This results in the occurrence of the VB mode. (iii) In the KS model, the inclination angle is independent of the shear rate. In the numerical results, the mean inclination angle θ_o decreases with increasing Ca and, hence, shear rate. (iv) In the KS model, the inclination angle goes to zero at a faster rate as λ approaches λ_c . In the simulations, θ_o is found to decrease at a much slower rate near the transition. As a result, tumbling occurs in the simulations even when $\theta_o > 0$. (v) The KS theory predicts that the ellipsoid spends equal amount of time in the extensional and compressional quadrants of the shear flow during the tumbling motion. In the simulations, we find that the capsule spends more time in the extensional quadrant of the flow than in the compressional quadrant.

The major departures from the SS theory are (i) the existence of the VB mode at a low Ca for which the shape deformation is the maximum, (ii) the emergence of the transient modes $\text{VB} \rightarrow \text{OS}$, $\text{TU} \rightarrow \text{VB} \rightarrow \text{OS}$, and $\text{TU} \rightarrow \text{VB}$, at

higher Ca , and (iii) absence of any intermittent dynamics. The occurrence of the VB mode cannot be predicted by the SS theory, as this mode corresponds to the maximum shape deformation. Further discrepancies between the SS theory and the numerical results are as follows: (iv) the SS theory predicts that the mean inclination angle θ_o is independent of $\dot{\gamma}$ in the OS regime, but the numerical results show that θ_o decreases with increasing Ca . (v) The large amplitude oscillation of the inclination angle at the intermediate λ is also not predicted by the SS theory. Unlike in the SS theory, here the shape deformation drives the orientation dynamics at the intermediate viscosity contrasts.

Several other interesting results are presented. The amplitude of shape deformation ΔD first increases reaching its maximum, but then decreases, with increasing λ . The major axis shows a greater variation in length over time than the minor axis. Compression of the capsule occurs at a slower rate than its elongation. Compression starts even when the major axis lies in the extensional quadrant of the flow. Elongation continues for $\theta < \pi/4$; the maximum elongation occurs progressively at an angle lower than $\pi/4$ with increasing λ and Ca . Further, though the capsule spends more time aligned with the extensional direction of the flow, it is actually subjected to a high compressive stress. These results could help in developing a phenomenological model of nonspherical capsule dynamics that can further improve the SS model.

5.2 Rheology of Dilute suspension of Capsules

In Chapter 4, we presented numerical results on the rheology of a dilute suspension of elastic capsules in linear shear flow. This study is partly motivated by the recent discovery that a dilute suspension of vesicles exhibits a shear viscosity minimum during the transition between the tank-treading and tumbling modes [14, 47–49], keeping in mind that fundamental differences exist between a vesicle and a capsule. In this chapter, we consider capsules of spherical resting shape for which only a steady tank-treading motion is observed. The important results obtained here are summarised as follows.

The suspension exhibits a shear-thinning behavior that is most prominent at moderate values of viscosity ratio λ . When variation with respect to λ is considered, two non-intuitive results are observed. First, at low capillary numbers, the shear stress decreases with increasing λ . This trend is opposite to that of a liquid drop suspension. Second, at high capillary numbers, the shear stress first decreases reaching a minimum, and then increases with increasing λ . Thus, unlike a vesicle suspension, the capsule suspension exhibits a shear viscosity minimum even in a steady tank-treading motion. Existence of the shear viscosity minimum can neither be explained by capsule shape, nor can be predicted by small deformation theory of capsule suspension.

However, this anomaly can be explained by decomposing the bulk stress into an elastic contribution due to the membrane tension, and a viscous contribution due to the viscosity difference between the interior and suspending fluids. It is

shown that the elastic component is shear-thinning, but the viscous component is shear-thickening. Hence, the opposite trends of the elastic and viscous components are responsible for the occurrence of the shear viscosity minimum in a capsule suspension. It is further shown that the trends of the elastic and viscous components can be qualitatively explained based on an isotropic model taking into consideration capsule shape and inclination.

The normal stress differences N_1 and N_2 show much more complex trends. At low viscosity ratio, their magnitudes increase with increasing Ca , as typical on an emulsion. But this trend is completely reversed at high viscosity ratio. Further, N_1 and $|N_2|$ decrease uniformly with increasing λ , in stark departure from the predictions of small deformation theory.

The elastic and viscous components of N_1 and N_2 are analysed to explain the observed trends. It is shown that the viscous components can be described by the isotropic model, but not the elastic components. However, the elastic components can be explained by considering the distribution of the membrane tension which is indeed anisotropic in nature. It appears that at high capillary number and viscosity ratio, emergence of a compressive membrane stress results in a reduction of the normal stress magnitudes.

The effect of area dilatation is also studied. Shear-thinning behavior gradually diminishes with reduced area dilatation. The shear viscosity minimum is observed for area dilating membranes, but not for nearly-incompressible membranes. This result is in stark contrast to that of the vesicle suspension because

the vesicle surface is incompressible. In closing, we note that no shape change is possible for a volume- and surface-area preserving object with a spherical initial shape. Thus, a vesicle has an excess area to start with. In contrast, the area of an initially spherical capsule is allowed to dilate in order for it to deform. However, a nonspherical capsule (e.g., a biconcave shape) can change its shape without area dilatation. Thus, it would be of interest to extend our simulations to suspension of nonspherical capsules with nearly-incompressible membranes to see if the shear viscosity minimum exists for such cases. Further, the nonspherical capsules exhibit tank-treading, tumbling and vacillating-breathing motions. It would be of interest to study the effect of such dynamics on the time-dependent and mean rheology of the suspension. Finally, it would be of great scientific value to address these issues for a dense or semi-dense suspension.

References

- [1] R.J. Asaro P. Sche Q. Zhu, C. Vera and L.A. Sung. A hybrid model for erythrocyte membrane: A single unit of protein network coupled with lipid bilayer. *Biophysical J.*, **93**:386, 2007.
- [2] N. Mohandas and E. Evans. Mechanical properties of the red cell membrane in relation to molecular structure and genetic defects. *Annu. Rev. Biophys. Biomolec. Struct.*, **23**:787–818, 1994.
- [3] H. Goldsmith and J. Marlow. Flow behaviour of erythrocytes i. rotation and deformation in dilute suspensions. *Proc. R. Soc. Lond. B.*, **182**:351, 1972.
- [4] M. Stohr-Liesen T.M. Fischer and H. Schmid-Schonbein. The red cell as a fluid droplet: Tank tread-like motion of the human erythrocyte membrane in shear flow. *Science.*, **202**:894, 1978.
- [5] M. Faivre M. Abkarian and A. Viallat. Swinging of red blood cells under shear flow. *Phys. Rev. Lett.*, **98**(188302), 2007.
- [6] M. Husmann H. Rehage and A. Walter. From two-dimensional model networks to microcapsules. *Rheol. Acta*, **41**:292, 2002.
- [7] V. Kantsler and V. Steinberg. Orientation and dynamics of a vesicle in tank-treading motion in shear flow. *Phys. Rev. Lett.*, **95**(258101), 2005.
- [8] V. Kantsler and V. Steinberg. Transition to tumbling and two regimes of tumbling motion of a vesicle in shear flow. *Phys. Rev. Lett.*, **96**(036001), 2006.
- [9] M. Abkarian A. Viallat M.-A. Mader, V. Vitkova and T. Podgorski. Dynamics of viscous vesicles in shear flow. *Eur. Phys. J. E*, **19**:389–397, 2006.
- [10] V. Kantsler J. Deschamps and V. Steinberg. Phase diagram of single vesicle dynamical states in shear flow. *Phys. Rev. Lett.*, **102**(118105), 2009.
- [11] S.R. Keller and R. Skalak. Motion of a tank-treading ellipsoidal particle in a shear flow. *J. Fluid Mech.*, **120**:27, 1982.
- [12] J.M. Skotheim and T.W. Secomb. Red blood cells and other nonspherical capsules in shear flow: Oscillatory dynamics and the tank-treading-to-tumbling transition. *Phys. Rev. Lett.*, **98**(078301), 2007.

- [13] D. Barthes-Biesel and J.M. Rallison. The time-dependent deformation of a capsule freely suspended in a linear shear flow. *J. Fluid Mech.*, **113**:251, 1981.
- [14] T. Podgorski C. Verdier G. Danker, T. Biben and C. Misbah. Dynamics and rheology of a dilute suspension of vesicles: Higher-order theory. *Phys. Rev. E.*, **76**(041905), 2007.
- [15] K.S. Turitsyn V.V. Lebedev and S.S. Vergeles. Nearly spherical vesicles in an external flow. *New J. Phys.*, **10**(043044), 2008.
- [16] S. Ramanujan and C. Pozrikidis. Deformation of liquid capsules enclosed by elastic membranes in simple shear flow: large deformations and the effect of fluid viscosities. *J. Fluid Mech.*, **361**:117–143, 1998.
- [17] A. Morel E. Lac and D. Barthes-Biesel. Hydrodynamic interaction between two identical capsules in simple shear flow. *J. Fluid Mech.*, **573**:149, 2007.
- [18] Y.T. Chew Y. Sui, H.T. Low and P. Roy. Tank-treading, swinging, and tumbling of liquid-filled elastic capsules in shear flow. *Phys. Rev. E*, **77**:016310, 2008.
- [19] R. Finken S. Kessler and U. Seifert. Swinging and tumbling of elastic capsules in shear flow. *J. Fluid Mech.*, **605**:207, 2008.
- [20] T. Biben and C. Misbah. Tumbling of vesicles under shear flow within an advected-field approach. *Phys. Rev. E*, **67**:031908, 2003.
- [21] U. Seifert M. Kraus, W. Wintz and R. Lipowsky. Fluid vesicles in shear flow. *Phys. Rev. Lett.*, **77**(17):3685, 1996.
- [22] T. Seon J. Beaucourt, F. Rioual and C. Misbah. Steady to unsteady dynamics of a vesicle in a flow. *Phys. Rev. E*, **69**:011906, 2004.
- [23] H. Noguchi and G. Gompper. Fluid vesicles with viscous membranes in shear flow. *Phys. Rev. Lett.*, **93**:258102, 2004.
- [24] H. Noguchi and G. Gompper. Dynamics of fluid vesicles in shear flow: Effect of membrane viscosity and thermal fluctuations. *Phys. Rev. E*, **72**:011901, 2005.
- [25] H. Noguchi and G. Gompper. Swinging and tumbling of fluid vesicles in shear flow. *Phys. Rev. Lett.*, **98**:128103, 2007.
- [26] C. Misbah. Vacillating breathing and tumbling of vesicles under shear flow. *Phys. Rev. Lett.*, **96**:028104, 2006.
- [27] P.M. Vlahovska and R.S. Gracia. Dynamics of a viscous vesicle in linear flows. *Phys. Rev. E*, **75**:016313, 2007.

- [28] C. Misbah M.-A. Mader, H. Ez-Zahraouy and T. Podgorski. On coupling between the orientation and the shape of a vesicle under a shear flow. *Eur. Phys. J. E*, **22**:275–280, 2007.
- [29] K. Kassner T. Biben and C. Misbah. Phase-field approach to three-dimensional vesicle dynamics. *Phys. Rev. E*, **72**:041921, 2005.
- [30] T. Biben F. Rioual and C. Misbah. Analytical analysis of a vesicle tumbling under a shear flow. *Phys. Rev. E*, **69**:061914, 2004.
- [31] C.S. Peskin. Numerical analysis of blood flow in the heart. *J. Comput. Phys.*, **25**:220–233, 1977.
- [32] S.O. Unverdi and G. Tryggvason. A front-tracking method for viscous, incompressible, multi-fluid flows. *Journal of Computational Physics*, **100**:25–37, 1992.
- [33] A. Esmaeeli N. Al-Rawahi W. Tauber J. Han S. Nas G. Tryggvason, B. Bunner and Y. Jan. A front-tracking method for the computations of multiphase flow. *J. Comp. Phys.*, **169**:708–759, 2001.
- [34] P.R. Zarda R. Skalak, A. Tozeren and S. Chien. Strain energy function of red blood cell membranes. *Biophys. J.*, **13**:245, 1973.
- [35] S. Shrivastava J.M. Charrier and R. Wu. Free and constrained inflation of elastic membranes in relation to thermoforming-non-axisymmetric problems. *J. Strain Anal.*, **24** (2):55–74, 1989.
- [36] S. Shrivastava and J. Tang. Large deformation finite element analysis of nonlinear viscoelastic membranes with reference to thermoforming. *J. Strain Anal.*, **28**:31–51, 1993.
- [37] C. D. Eggleton and A. S. Popel. Large deformation of red blood cell ghosts in a simple shear flow. *Physics of Fluids*, **10**(8):1834–1845, 1998.
- [38] S. K. Doddi. Three-dimensional computational modeling and simulation of biological cells and capsules. *PhD thesis*, 2008. Rutgers University.
- [39] S.K. Doddi and P. Bagchi. Lateral migration of a capsule in a plane poiseuille flow in a channel. *Intl. J. Multiphase Flow*, **34**:966–986, 2008.
- [40] S.K. Doddi and P. Bagchi. Three-dimensional computational modeling of multiple deformable cells flowing in microvessels. *Phy. Rev. E*, **79**:046318, 2009.
- [41] Prosenjit Bagchi and R. Murthy Kalluri. Dynamics of nonspherical capsules in shear flow. *Physical Review E*, **80**:016307, 2009.
- [42] Prosenjit Bagchi and R. Murthy Kalluri. Rheology of a dilute suspension of liquid-filled elastic capsules. *Physical Review E*. Submitted March 2010.

- [43] G. K. Batchelor. The stress system in a suspension of force-free particles. *Journal of Fluid Mechanics*, **41**(03):545–570, April 1970.
- [44] V. Chhim D. Barthes-Biesel. The constitutive equation of a dilute suspension of spherical microcapsules. *International Journal of Multiphase Flow*, **7**(5):493–505, Oct. 1981.
- [45] C. Pozrikidis. Finite deformation of liquid capsules enclosed by elastic membranes in simple shear flow. *Journal of Fluid Mechanics*, **297**:123–152, 1995.
- [46] C. Pozrikidis. Numerical simulation of the flow-induced deformation of red blood cells. *Ann. Biomed. Eng.*, **31**:1194–1205, 2003.
- [47] Gerrit Danker and Chaouqi Misbah. Rheology of a dilute suspension of vesicles. *Phys. Rev. Lett.*, **98**(8):088104, 2007.
- [48] C. Misbah G. Danker, C. Verdier. Rheology and dynamics of vesicle suspension in comparison with droplet emulsion. *J. Non Newtonian Fluid Mech.*, **152**:156–167, 2008.
- [49] B. Polack C. Misbah V. Vitkova, M.-A. Mader and T. Podgorski. Micro-macro link in rheology of erythrocyte and vesicle suspensions. *Biophys. J.*, **95**(7):L33–L35, 2008.
- [50] P. Roy Y. P. Cheng Y. Sui, Y. T. Chew and H. T. Low. Dynamic motion of red blood cells in simple shear flow. *Phys. Fluids*, **20**:112106, 2008.
- [51] X. Y. Li and K. Sarkar. Front tracking simulation of deformation and buckling instability of a liquid capsule enclosed by an elastic membrane. *J. Comput. Phys.*, **227**:4998, 2008.
- [52] G. I. Taylor. The viscosity of a fluid containing small drops of another fluid. *Proc. R. Soc. Lond. A*, **138**:41–48, Oct. 1932.
- [53] J. Blawdziewicz P. Vlahovska and M. Loewenberg. Nonlinear rheology of a dilute emulsion of surfactant-covered spherical drops in time-dependent flows. *J. Fluid Mech.*, **463**:1–24, 2002.